The Astronomy and Astrophysics Review manuscript No.
(will be inserted by the editor)

Precise radio astrometry and new developments for the next generation of instruments

María J. Rioja · Richard Dodson

Received: date / Accepted: date

Abstract We present a technique-led review of the progression of precise radio astrometry, from the first demonstrations, half a century ago, until to date and into the future. We cover the developments that have been fundamental to allow high accuracy and precision astrometry to be regularly achieved. We review the opportunities provided by the next-generation of instruments coming online, which are primarily: SKA, ngVLA and pathfinders, along with EHT and other (sub)mm-wavelength arrays, Space-VLBI, Geodetic arrays and optical astrometry from GAIA.

From the historical development we predict the future potential astrometric performance, and therefore the instrumental requirements that must be provided to deliver these. The next-generation of methods will allow ultra-precise astrometry to be performed at a much wider range of frequencies (hundreds of MHz to hundreds of GHz). One of the key potentials is that astrometry will become generally applicable, and therefore unbiased large surveys can be performed. The next-generation methods are fundamental in allowing this. We review the small but growing number of major astrometric surveys in the radio, to highlight the scientific impact that such projects can provide.

Based on these perspectives, the future of radio astrometry is bright. We foresee a revolution coming from: ultra-high precision radio astrometry, large surveys of many objects, improved sky coverage and at new frequency bands

M. J. Rioja
CSIRO Astronomy and Space Science, 26 Dick Perry Avenue, Kensington WA 6151, Australia and
International Centre for Radio Astronomy Research, The University of Western Australia, 35 Stirling Hwy, Western Australia and
Observatorio Astronómico Nacional (IGN), Alfonso XII, 3 y 5, 28014 Madrid, Spain
E-mail: maria.rioja@uwa.edu.au

R. Dodson
International Centre for Radio Astronomy Research, The University of Western Australia, 35 Stirling Hwy, Western Australia

other than those available today. These will enable the addressing of a host of innovative open scientific questions in astrophysics.

Keywords Astronomical instrumentation, methods and techniques · Instrumentation: interferometers · Methods: observational Radio astronomy

Contents

1 Introduction

The field of astrometry, through the measurement of the precise positions, distances and motions of astronomical objects, is a fundamental tool for astrophysics, and has been revolutionised in recent years. The level of accuracy and precision achieved, along with its applicability, determines its potential. Currently radio astrometry with Very Long Baseline Interferometry (VLBI) provides the highest accuracy and precision in astronomy. The relentless increase of the precision in these measurements over time has extended the application into many new areas of fundamental astronomy, astrophysics and cosmology. As a result astrometry is assisting in the revision of our knowledge of the physical parameters of individual sources, such as size, luminosity, mass and age, and the understanding of stellar birth and stellar evolution, using direct measurements of the trigonometric parallax distances to objects across the Galaxy, with unprecedented $\pm 10\%$ accuracy. Furthermore, combining with the proper motion measurements these reveal the 3-D spiral structure and the values of the fundamental dynamical parameters of our Galaxy, using the six-dimensional phase-space distributions of Galactic sources. In many cases the "gold standard" VLBI distances measured by trigonometric parallax is significantly different from the kinematic distances and also occasionally to Hipparcos measurements, hence the fundamental role of VLBI to serve as a cross-check for its successor, GAIA. For a recent review of the astrophysical applications of these measurements in radio astrometry see Reid and Honma (2014), and for optical astrometry see Vallenari (2018).

1.1 VLBI astrometry

Very Long Baseline Interferometry is a geometric technique that provides the highest angular resolutions in astronomy, as sketched in Fig. 1. Interferometry consists of the measurements of the coherence function, at a spatial separation. In astronomy these correspond to the correlation of two signals, taken

by observatories separated by a 'baseline' vector and, as the signal is travelling from astronomical distances, represents the Fourier term of the transform of the brightness distribution of the observable sky, at the spatial frequency given by the baseline (e.g., Van Citter 1934, discussed in Born and Wolf 1999). Larger separations (i.e. longer baselines) represent higher 'spatial frequencies' and provide higher image angular resolutions. The more complete the sampling the more reliable will be the reconstruction of the sky brightness distribution. Radio interferometry is blessed in that the phase of the correlated signal can be measured, so the coherence function can be recovered. This complex quantity is called the 'visibility function' and depends only on the antenna pair separation (the baseline), measured in uv-space: (u, v, w), and the brightness distribution. Thus the reconstruction of the observed sky can be performed with a simple Fourier transform of these complex quantities, sampled at the uv-points. In comparison, for optical interferometry or X-ray crystallography the phase terms are lost, introducing significant complexities in the reconstruction (e.g., Perutz 1962). The phase of a complex number has the greatest impact on image reconstruction, thus in radio the prime observable quantity is considered to be the phase and its derivatives in frequency (delay) and time (rate), particularly in astrometry where peak position is more important than image fidelity. VLBI uses simultaneous observations between an array of widely separated telescopes, each equipped with an extremely precise atomic clock, to measure the delay or difference in the arrival time of a radio wavefront at pairs of antennae when combined at the time of the correlation; the output of the correlator becomes what we call the VLBI observables. In the ideal case without errors, as shown Fig. 1, this measures the geometric delay $\tau_{\rm geo}$. That is $\tau_{\rm geo} = \overrightarrow{b}.\hat{s}/c$, where $\hat{s}$ is the unit vector in the direction of the source, $\overrightarrow{b}$ is the baseline vector and c is the speed of light. Astrometry is concerned with the accurate measurement of this term, but in reality the direct measurement is contaminated with delay contributions arising from instrumental and atmospheric propagation effects. Moreover, the wide separations between the antennas makes the stabilisation of phases difficult because the lines of sight from each antenna pass through totally uncorrelated atmospheres (ionosphere and troposphere). The art of astrometry is the careful identification and correction for these non-astronomical contributions, through special observational and analytical techniques, and by using accurate geometric and atmospheric a-priori models; that is 'calibration'. Because these measurements are precise to a few picoseconds VLBI has the potential to determine the celestial source positions to micro-arcsecond (μas) level when using very long baselines, providing there is sufficient signal-to-noise ratio (SNR). For a full description of the fundamentals of radio interferometry we recommend Thompson et al. (2017). The individual elements of the array can be very different in character, as indicated in Fig. 1. With the new technical capabilties now available the elements can be comprised of: connected-arrays forming multiple tied-array beams, large telescopes with multi-beam feeds and/or smaller telescopes with a single pixel feed. Therefore, despite their difference in character, they can

have a matching, larger, Field of View (FoV) (see the light orange cone, Fig. 1).

The majority of VLBI post-processing analysis uses self-calibration techniques, which are very powerful and widely used to generate the highest spatial resolution images in astronomy. Self-calibration relies on phase-closure constraints to separate the contributions from the (baseline-based) intrinsic source structure from all other (antenna-based) contaminating contributions that are cancelled out in the summation around the three baselines. The latter includes the source position errors, which is therefore lost in the image product. Special post-processing analysis techniques are therefore required to preserve the astrometric information, whilst removing the bulk of errors from the contaminating contributions. The conditions for astrometry with VLBI are more stringent than those for imaging, which results in astrometric surveys being constrained by selection effects and biases, and limited to a restricted region of the spectrum. This paper focuses on the exciting opportunities (and challenges) for ultra-high precision ($\sim\mu$as) radio astrometric surveys with the arrival of the next-generation instruments, planned and under construction, from the combined power of highest sensitivity and long baselines, along with a historic perspective of the evolution of the precision astrometric measurements in the past 50 years.

The key lies both in the ongoing advances in the accuracy and precision of astrometric measurements and its extended applicability to many objects. Nowadays, 10 μas high precision astrometry is achievable, for a limited range of frequencies; this level of accuracy is approaching the potential (i.e., the thermal noise level) of the observations with current instruments. The power and potential of astrometric surveys have been demonstrated, for example with the 3-D Galactic mapping projects carried by BeSSeL (Bar and Spiral Structure Legacy) and VERA (VLBI Exploration of Radio Astrometry). Great benefits will be obtained from comprehensive surveys of high-accuracy radio astrometric measurements, as demonstrated by the optical GAIA astrometry mission. This of course requires that the astrometric methods for radio are robust and widely applicable for more targets and at a wider range of frequencies; that is, that they are not limited to carefully selected cases.

The arrival of the next-generation radio observatories, such as the Square Kilometre Array (SKA; Braun et al. 2015) and the next-generation Very Large Array (ngVLA; Murphy 2018), will provide a huge increase in sensitivity, by up to several orders of magnitude, spanning the whole radio frequency band; these observatories will participate in VLBI observations, as powerful phased-up telescopes, in conjunction with other existing telescopes, resulting in a dramatic increase in the sensitivity of the VLBI array. The combination of enhanced sensitivity and long baselines offers great benefits for astrometry, and will result in a "breakthrough" with respect to what we can achieve today. On one hand we will have the ability to significantly increase the astrometric measurement accuracy, on the other, the capability to study in exquisite detail larger samples through the inclusion of weaker objects. That is, the realistic possibility to carry out large radio μas astrometric surveys of complete sam-

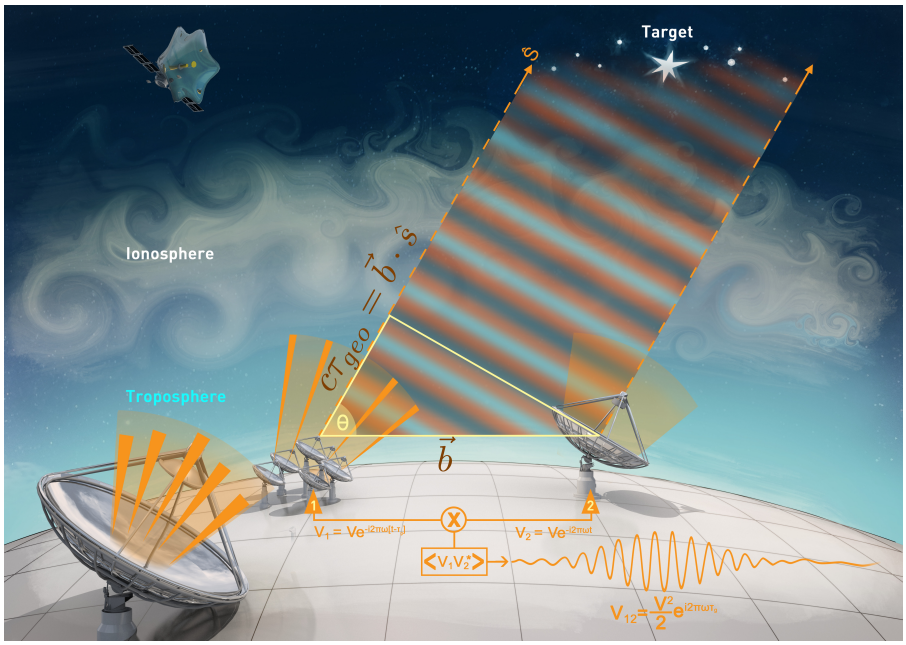

Fig. 1 A schematic of a VLBI interferometric array, comprising diverse elements on the ground and in space. VLBI measures the total delay in the arrival time of the signal from a target source, along the direction $\hat{s}$, to pairs of elements that can be separated by thousands of kilometres and form the baseline $\overrightarrow{b}$. The dot product of the two vectors corresponds to the geometric delay $\tau_{\rm geo}$. The propagation through the turbulent tropospheric and ionospheric components of the atmosphere introduces additional contaminating delays, as does the instrumentation, which need to be removed in the analysis (Sects. 3 and 5). The long baseline allows an extremely accurate determination of $\hat{s}$. Each pair of elements output two voltages, V_1 and V_2, which are multiplied and averaged in the correlator, creating a time-dependent interferometric fringe pattern. The phase and delay from this complex correlated data product are the fundamental VLBI observables in astrometry. The figure shows a variety in the nature and size of the elements in a VLBI-array in the era of the next-generation of instruments (Sect. 4). Alongside the moderate-sized single dish telescope there are the large collecting areas provided by a massive single dish or many smaller dishes from a connected array phased-up, and also the extremely long baselines provided by a radio telescope on a space platform. New technologies can provide matching FoVs (light orange cones) from all of these elements and the capability for multi-frequency observations (Sect. 7). Multiple-pixel capabilities are illustrated by the multiple tied-array beams from the connected array and the multiple beams from a phased array feed on the large telescope, both of which match the wider FoV of the moderate-sized single pixel telescope. The capability for simultaneous multi-frequency observations is indicated by the two-tone incoming wavefront. Image credit: M.J. Rioja and R. Dodson

ples of objects, to advance the understanding of astrophysical phenomena and classes.

The next-generation instruments bring opportunities and challenges for astrometry. Increased sensitivity (alone) does not result in increased astrometric accuracy and precision in the presence of systematic errors, which often set the ultimate limit. In order to realise the full potential from the enhanced sensitiv-

ity with the next-generation instruments, calibration algorithms for systematic errors must achieve the same level of refinement; that is, to mitigate the systematic residual errors to the reduced level of the thermal noise limits of the observations. The on-going development of new calibration methods and new technologies are breaking new ground and providing solutions to overcome the current limitations, in particular the frequency dependent systematic errors arising from the propagation of a wave-front through the Earth's atmosphere, which constitutes the dominant source of astrometric errors that limit the applicability. The distinct nature of these errors across the spectrum requires different calibration strategies depending on the observing frequency, and this drives the layout followed in this review. Additionally, one will have to deal with the new sources of errors that will become significant at these reduced thermal noise levels. The goal is that a combination of all these new developments will lead to the improvement of astrometric performance by an order of magnitude, for a wide range of radio frequencies and for many objects with the prospect to expand its applications into new areas of research.

Contents of this paper: The sections in this paper are organised to provide: a common framework and description for astrometric methods; an overview of the achievements so far, with highlights from surveys with current instruments; and a projection into the future of radio astrometry. The imminent arrival of new instruments and new technological and analytical developments will enable new astrophysical applications, examples of which we describe.

Section 2 is concerned with the fundamental constraints in astrometry and provides the framework for the characterisation and comparison of the methods. Section 3 reviews the past progress in calibration, with established methods. Section 4 is an overview of the next-generation instruments planned or under construction across the radio frequency band, from the perspective of the new astrometric opportunities offered by their extremely high sensitivity and the new science enabled. Section 5 introduces recent innovations in methods, and enabling technologies, of interest for these next-generation instruments. Section 6 looks back at the evolution of the published astrometric results and compares them to the expected systematic errors, to identify the important advances so far. Section 7 describes key technological developments and recent atmospheric propagation studies relevant to the next-generation methods described above, to match the potential of the next-generation instruments. Section 8 is a review of a subset of astrometric surveys with existing instruments, selected to highlight the benefits of high-precision astrometry. They are limited to publications since the review of Reid and Honma (2014). Section 9 explores the future scientific possibilities opened by the new methods and available or planned infrastructure. Section 10 is the summary of the review.

2 Fundamental constraints in astrometry

We aim at reviewing the astrometric constraints, along with a focus on methods and technological developments that have contributed to significant advances in the field, as a launchpad for inferring the direction of new developments into the future. Benefits have come from increasingly stable instruments, receiver and backend developments that resulted in increased sensitivity through low system temperatures, wider bandwidths, frequency agility, improved telescope networks to optimise uv-coverage and higher slew speeds of radio telescopes.

These combined with advances in calibration methods, the increased number and frequency coverage of suitable calibrator sources, improved a-priori knowledge of the contributions to the observables, among others, have paved the way towards the huge expansion of the field of precise astrometry with VLBI.

Next-generation instruments provide unprecedented sensitivity and have the potential for an order of magnitude improvement, delivering μas astrometric surveys, provided the requirements for optimum astrometric calibration methods and usability are not designed out.

2.1 Micro-arcsecond astrometry basics

The primary VLBI observables for high precision astrometry are: the interferometric phase ϕ, the phase difference between the signals received at a pair of antenna, or equivalently the phase delay (the phase in radians divided by the frequency in Hz, in seconds; $\tau_\phi = \frac{1}{2\pi}\frac{\phi}{\nu}$), the frequency derivative or group delay (the rate of change of phase with frequency, in seconds; $\tau_g = \frac{1}{2\pi}\frac{\delta\phi}{\delta\nu}$) and the phase time derivative (usually as delay rate in seconds/second; $\frac{1}{2\pi\nu}\frac{\delta\phi}{\delta t}$). Following the standard nomenclature (e.g., Thompson et al. 2017) the residual phase values or errors, after subtracting the *a-priori* model contributions from the measured values at the time of correlation or post-processing, for observations of the target source (A) for a given baseline as a function of time and frequency, are shown as a sum of contributions:

$$\phi_A(t,\nu) = \phi_{A,\mathrm{pos}}+\phi_{A,\mathrm{str}}+\phi_{A,\mathrm{geo}}+\phi_{A,\mathrm{tro}}+\phi_{A,\mathrm{ion}}+\phi_{A,\mathrm{inst}}+\phi_{A,\mathrm{thermal}}+2\pi n \qquad n \in \text{integer} \tag{1}$$

where the most relevant in astrometry is $\phi_{A,\mathrm{pos}} = 2\pi\,\overrightarrow{b}.(\hat{s}_{\mathrm{true}} - \hat{s}_{\mathrm{model}})\,/\,\lambda$ arises from inadequacies in the a-priori knowledge of the source position, with $\hat{s}_{\mathrm{true}}$ the unit vector in the actual direction of the source and $\hat{s}_{\mathrm{model}}$ is the a-priori position used in the correlation, $\overrightarrow{b}$ is the baseline vector and λ is the wavelength of the observing frequency ν. $\phi_{A,\mathrm{str}}$ stands for the contribution from the structure in extended sources. These terms represent the intrinsic properties of the source of interest to astrometry and are mixed with other extrinsic or contaminating contributions such as: $\phi_{A,\mathrm{geo}}$ arising from

model errors in the geometry of the array including the orientation of the Earth among others, $\phi_{A,\mathrm{tro}}$ and $\phi_{A,\mathrm{ion}}$ arise from mismodelling of propagation medium effects as the cosmic signal transverses the Earth's atmosphere, due to unpredictable refractivity variations in the troposphere and ionosphere along the line of sight, respectively. $\phi_{A,\mathrm{inst}}$ is due to the unaccounted instrumental instabilities. The purpose of astrometric calibration is the identification and elimination of these extrinsic terms. $\phi_{A,\mathrm{thermal}}$ stands for the thermal noise error or measurement error and is related to the sensitivity of the instrument, setting the ultimate potential astrometric limit, with a standard deviation given by $\sigma\phi_{A,\mathrm{thermal}} \sim \frac{1}{SNR}$ in radians, where SNR is the signal-to-noise ratio of the fringe detection. Finally, $2\pi n$ stands for an unknown integer number n of 2π phase cycles that represents the inherent ambiguous nature of the measured phases; n can vary between observations of the same source at different times, and between different sources. It sets the greatest challenge for astrometry using the phase observable.

The group delay observable is determined from the phase slope over the discrete frequencies in the spanned observed bandwidth. A similar qualitative description as shown in Eq. (1) applies to the residual group delay values, but without the 2π ambiguity term, which makes it more usable for absolute position measurements. The group delay is the observable used for VLBI geodesy and absolute astrometry. The phase delay observable is significantly more precise than the group delay, by a factor of $\frac{\nu}{\Delta\nu_{\mathrm{eff}}}$, where ν stands for the observing frequency, $\Delta\nu_{\mathrm{eff}}$ is related to the effective spanned (synthesised) bandwidth ($\Delta\nu_{rms}$ in Thompson et al. 2017, Eq. A12.32), and is the order of 30 for $\nu = 8\,\mathrm{GHz}$ and $\Delta\nu_{\mathrm{eff}} = 0.3$ GHz.

Using the extremely precise phase observable has the potential to reach μas level astrometry; on the other hand the inherent ambiguous nature of the measured phases (i.e., only known to modulo 2π) complicates its direct interpretation. To resolve this issue requires a sufficiently accurate a-priori knowledge of the value of all the contributions in Eq. (1) to a small fraction of the phase ambiguity spacings, which corresponds to the length of the observing wavelength. This is the so called "phase connection" process, which is complicated for the long baselines of VLBI.

An approach to overcome this issue is to use a differential or relative analysis. For example, the differential observables of near-contemporaneous observations of two nearby sources on the sky, a target (T) and a reference (R), reduces the sensitivity to the mismodelling of common contributions. Such an observing schedule consists in general of interleaving scans between a pair of sources for which the angular separation or switching angle and the source switching time are significantly smaller than the isoplanatic patch size and the atmospheric coherence time, respectively, at the observing frequency. The coherence time is conventionally defined as the time for the phase change to be a radian and can be very short at high frequencies.

Following Eq. (1) the residual differential phase observable is given by:

$$\phi_T(t,\nu) - \phi_R(t',\nu) = (\phi_{T,\rm pos} - \phi_{R,\rm pos}) + (\phi_{T,\rm str} - \phi_{R,\rm str})$$
$$+(\phi_{T,\rm geo} - \phi_{R,\rm geo} + \phi_{T,\rm tro} - \phi_{R,\rm tro} + \phi_{T,\rm ion} - \phi_{R,\rm ion} + \phi_{T,\rm inst} - \phi_{R,\rm inst})$$
$$\pm\sigma\phi_{\rm thermal} + 2\pi(n_T - n_R) \qquad n_T, n_R \in \text{integer}$$

where $\phi_{T,\rm geo} - \phi_{R,\rm geo} \sim 0; \phi_{T,\rm tro} - \phi_{R,\rm tro} \sim 0; \phi_{T,\rm ion} - \phi_{R,\rm ion} \sim 0; \phi_{T,\rm inst} - \phi_{R,\rm inst} \sim 0$, when the conditions described above are fulfilled. In this case the differential observable is largely free from the contaminating error contributions and therefore yields an accurate estimate of the relative or differential astrometry between T and R, which is derived from the term $\phi_{T,pos} - \phi_{R,pos}$. The source structure terms and the noise terms do not cancel; the former can be estimated using self-calibration techniques and hence are not an astrometric challenge, the latter, $\sigma\phi_{\rm thermal}$, is the combined thermal error term. To a first order approximation, the magnitude of the residual differential errors for the contaminating contributions are reduced by a so called "dilution factor" given by the pair angular separation, or switching angle, expressed in radians; additionally the switching time is relevant. Similar difference equations can be written for both the other observables the delay and the rate, but the phase observable has the potential to provide the most accurate astrometry and it is the focus of this paper. Implementations of this concept are the so called differential phase delay and phase reference imaging (or simply phase referencing) astrometric techniques.

The main challenge of differential astrometry is to connect the phases and resolve the ambiguity issue for each source, baseline and time. This has been successfully achieved using two approaches: phase-delay fitting (e.g., Wittels 1975; Shapiro et al. 1979; Marcaide and Shapiro 1984; Bartel et al. 1986) and phase reference mapping (e.g., Alef 1988; Lestrade et al. 1990). The former uses an iterative process to determine the value of Δn between consecutive measurements of the phase for both sources using the individual and differential observables; this is followed by a least-squares fit of the unambiguous differential phase delays to measure the relative source separation (Robertson 1975). The latter does not explicitly determine the Δn integer for the target source, but instead uses a Fourier transform of the differential observable to form an image, where the shift in the position of the peak intensity of the source with respect to the centre of the image directly conveys the relative astrometric information in $\phi_{T,pos} - \phi_{R,pos}$ or $\delta\theta$. In general, the residual rates are used for the phase connection between consecutive measurements of the reference source and to interpolate the value to the time of the target source. The approaches of phase-delay fitting or phase-referenced mapping are equivalent, albeit with some differences as described in the next section; they have been evolving since first proposed but without changing their essence. In this paper we refer to both methods as conventional phase referencing or simply PR.

In the last 45+ years there have been steady incremental improvements of phase-based relative astrometry. Important steps forward have come from:

i) improved instrumental stability and sensitivity, ii) longer baselines, iii) improved a-priori models applied to both target and reference data, vi) advanced calibration strategies to mitigate the propagation of "contaminating" residual errors into astrometric errors at different frequency regimes, and vii) improved astrometric VLBI calibrator catalogues.

The low frequency regime has lagged behind, but have had a renaissance with the arrival of the next-generation instruments such as the SKA. We foresee a new era for astrometry with the combined power from the next-generation instruments and breakthrough technologies planned and under construction, and new calibration algorithms.

We highlight that innovative recent calibration developments have come from extending the concept of a 'reference' beyond observations of another source, as in established methods. Therefore we use a generalised expression for the differential phase observable, as a linear combination of the target and reference observables, where the latter can comprise observations of the same target source or another, or multiple other sources, at the same frequency as the target (ν_T) or at a different frequency (ν_R), or a combination of these strategies:

$$\phi_T(t,\nu_T) - \mathcal{R}\times\phi_R(t',\nu_R) = (\phi_{T,\mathrm{pos}} - \mathcal{R}\times\phi_{R,\mathrm{pos}}) \pm \sigma\phi^{\mathrm{cal}} \pm \sigma\phi_{\mathrm{thermal}} + 2\pi(n_T - \mathcal{R}n_R) \quad (2)$$

where $(\phi_{T,\mathrm{pos}} - \mathcal{R}\times\phi_{R,\mathrm{pos}})$ retains the relative astrometry information of interest, with $\mathcal{R}$ a real linear scale factor for the reference phases. $\mathcal{R}$ is method dependent, for example it is equal to 1 for PR, or to the frequency ratio for frequency phase transfer. $\sigma\phi^{\mathrm{cal}}$ stands for the combined residual differential phase errors from mismodelling of the contaminating contributions (*hereafter* calibration errors) for a given calibration method. The other terms are as before. Residual contributions from atmospheric mismodelling are the dominant source of calibration errors and limit the accuracy of the astrometric measurements (i.e., in general one is in the systematic error limited regime); their magnitude is quantified next. Errors in the a-priori geometric parameters, such as in telescope and reference source coordinates, Earth orientation parameters etc., usually have a lesser effect, thanks to improvements from VLBI geodetic observations; all of these are usually larger than the instrumental contribution, due to modern stable electronic systems and maser clocks. In an ideal calibration scenario $\sigma\phi^{cal} \sim 0$ and $\sigma\phi_{\mathrm{thermal}}$ sets the ultimate limit in the astrometric accuracy (i.e., one is in the thermal noise limited regime). The structure terms $\phi_{T,\mathrm{str}}$ and $\phi_{R,\mathrm{str}}$ can be estimated from the images and are excluded from Eq. (2) to simplify the presentation. Nevertheless, see Sect. 2.2 on the stability of reference points for details on some considerations.

Asaki et al. (2007) presented semi-analytic expressions to estimate the magnitude of residual propagation effects for conventional PR from unaccounted refractivity changes over time and space (dynamic and static, respectively) in the troposphere and the ionosphere; we find the latter the most complete description of the various similar investigations (e.g., Pradel et al. 2006; Honma et al. 2008). These are the dominant contributions to $\sigma\phi^{cal}$. We will use a

modified version of those to estimate the calibration errors using different astrometric techniques presented in the next sections. The errors comprise of dynamic (or rapidly varying) components (hereafter $\sigma\phi^{\rm cal}_{\rm dyn,tro}$ and $\sigma\phi^{\rm cal}_{\rm dyn,ion}$) arising from short term fluctuations in the distribution of water vapour (the "wet" component) in the troposphere and of the total electron content (TEC, measured in TEC Units where 1 TECU = 10^{16}el/m^2) in the ionosphere, along the line of sight of the observations, respectively. These introduce random fluctuations with zero mean. The static (or slowly varying) components (hereafter $\sigma\phi^{\rm cal}_{\rm sta,tro}$ and $\sigma\phi^{\rm cal}_{\rm sta,ion}$) arise from relatively stable contributions predominately from the hydrostatic ("dry") components in the troposphere, and the TEC in the ionosphere, respectively. Eq. (3) is a modified version of those in Asaki et al. (2007), adjusted to 8 GHz and for ground to ground baselines (i.e., scaling by 5.4 and multiplying by $\sqrt{2}$, respectively), in units of degrees:

$$
\begin{aligned}
\sigma\phi^{\rm cal}_{\rm sta,tro}(\nu) &= 20.0(\nu/8{\rm GHz})(\Delta\ell_z/3{\rm cm})(\Delta\theta_{\rm tro}/2^\circ) \\
&\times (\sec(Z_g)/\sec(45^\circ))(\tan(Z_g)/\tan(45^\circ)) \\
\sigma\phi^{\rm cal}_{\rm sta,ion}(\nu) &= 20.5(\nu/8{\rm GHz})^{-1}(\Delta{\rm I}/6{\rm TECU})(\Delta\theta_{\rm ion}/2^\circ) \\
&\times (\sec(Z_F)/\sec(41^\circ))(\tan(Z_F)/\tan(41^\circ)) \\
\sigma\phi^{\rm cal}_{\rm dyn,tro}(\nu) &= 7.1\,C_w(\nu/8{\rm GHz})(\sec(Z_g)/\sec(45^\circ))^{1/2} \\
&\times [T_{\rm swt,tro}/60s + 0.16(\sec(Z_g)/\sec(45^\circ))(\Delta\theta_{\rm tro}/2^\circ)]^{5/6} \\
\sigma\phi^{\rm cal}_{\rm dyn,ion}(\nu) &= 3.5(\nu/8{\rm GHz})^{-1}(\sec(Z_i)/\sec(43^\circ))^{1/2} \\
&\times [0.21(T_{\rm swt,ion}/60s) + (\sec(Z_i)/\sec(43^\circ))(\Delta\theta_{\rm ion}/2^\circ)]^{5/6}
\end{aligned}
\tag{3}
$$

where ν is the observing frequency in GHz, Z_g is the mean zenith angle for the two sources in degrees at the ground level for a terrestrial telescope, Z_i and Z_F are the zenith angles at the ionosphere piercing points, for the bottom (∼300 km) and the peak (∼450 km) of the F-layer, respectively. $\Delta\ell_z$ is the residual tropospheric zenith excess path length in cm and ΔI is the residual total electron content (TEC) in TECU in the zenith direction at the ionosphere piercing point. ΔI can be expressed as a frequency dependent excess path length, in cm, as $40.3\Delta{\rm I}\,\nu^{-2}$ with ΔI in TECU and ν in GHz. C_w is a unitless factor to characterise tropospheric conditions (with values of 1, 2 or 4 for good, normal and poor). Some parameters are specific to the calibration strategy: $\Delta\theta_{tro}$ and $\Delta\theta_{\rm ion}$ are the angular separations, between T and R, relevant for the mitigation of the spatial structure of the tropospheric and ionospheric disturbances, respectively, in degrees; $T_{\rm swt,tro}$ and $T_{\rm swt,ion}$ are the equivalent in the temporal domain, corresponding to the switching time between interleaving observations of T and R, respectively, in seconds.

For example, typical values for $\Delta\ell_z$ and ΔI, after calibration solely using ground based measurements for water vapour and GPS-derived TEC corrections, are 3–5 cm and 6–10 TECU, respectively.

Inspection of Eq. (3) leads to several immediate conclusions for the contributions to calibration errors in conventional PR:

- That the tropospheric residual errors scale with frequency and the ionospheric contributions scale with wavelength.
- That the balance between tropospheric and ionospheric calibration errors falls around 8 GHz
- That the smaller the angular separation ($\Delta\theta$) between T and R the smaller are all the phase errors.
- That the faster the switching time ($T_{\rm swt}$) between T and R the smaller the dynamic errors.
- That the static terms, all other contributions being nominal, are the most significant for astrometry.
- That the static tropospheric phase errors scale linearly with the residual path length ($\Delta\ell_z$).
- That the static ionospheric phase errors scale linearly with the residual TEC (ΔI).
- That the errors grow very large at low elevations, particularly for the troposphere.[1]
- That, for the tropospheric dynamical terms, the errors related to switching time dominate those related to the angular separation.
- That, for the ionospheric dynamical terms, the errors related to the angular separation dominate those related to the switching time.

Expressions for the calibration errors arising from the geometrical model are presented in Asaki et al. (2007); Shapiro et al. (1979); Reid and Honma (2014) and other publications and are functionally similar to the static troposphere, but of a smaller scale. The consequences of errors in the reference source position are discussed, for phase reference mapping, in Reid and Honma (2014, Sec. 5.4); to avoid the second-order effects the absolute position of the reference source should be known to better than 10 mas.

Finally we discuss the impact of the calibration errors onto the accuracy of the astrometric measurements or astrometric errors. It is intuitively easy to understand that the propagation onto astrometric errors ($\sigma\Delta\theta^{\rm cal}$) will vary depending on the nature of the calibration errors, as well as the array geometry. For example, the dynamic components introduce random fluctuations with zero mean and average away rapidly. Therefore, if they are not large enough to prevent phase connection, these do not introduce systematic bias in the astrometric measurements. The static components, however, introduce long-term phase gradients above a telescope, which will not average out over the experiment and would propagate into a position error in the image (without loss in the peak flux, if coherent across the array); therefore they are the most important astrometric error contribution. Both components would lead to degraded image quality, with the fractional flux ratio (FFR) being $e^{-\sigma\Phi^2/2}$ (Thompson et al. 2017), where $\sigma\Phi$ is the standard deviation of the phase errors.

Here, we follow a simple approach to estimate the systematic astrometric error for a single epoch of observations: $\sigma\Delta\theta^{\rm cal} \approx \frac{\sigma\phi^{\rm cal}_{\rm sta}[\rm deg]}{360^\circ}\theta_{\rm beam}$, or equiva-

[1] Compare Figs. 13.6 and 14.3 in Thompson et al. (2017) for the difference between the dependence of the troposphere and the ionosphere.

lently $\approx \frac{\Delta\ell}{|b|} \sec Z \tan Z \Delta\theta$, where $|b|$ is the maximum baseline length, $\theta_{\rm beam}$ is the synthesised beam size, Z is the mean Zenith angle, and $\sigma\phi^{\rm cal}_{\rm sta}$ and $\Delta\ell$ correspond to adding in quadrature the residual error terms arising from static tropospheric and ionospheric disturbances for the phase and excess pathlength, respectively. This simple expression assumes that $\Delta\theta$ is common for all contributions; in PR this corresponds to the angular separation between the target and the calibrator sources. Smaller contributions from geometric errors and thermal noise ($\sigma\Delta\theta_{\rm thermal}$; see next section) will also contribute. The simple approximation used here is acceptable for observations with moderate zenith angles with most arrays. A complete characterisation of the astrometric error propagation requires detailed analysis using simulation studies, such as carried out in Pradel et al. (2006); Asaki et al. (2007) or Honma et al. (2008), to correctly account for the impact of the array configuration and source declination, among other considerations.

In Sects. 3 and 5 we review the differential astrometric methods, with emphasis on the relevant aspects to reduce the dominant errors and scope of application in each case. We use Eq. (3) to estimate the phase errors and the astrometric errors as described above to characterise and compare the expected performance of the different methods.

2.2 Definition and stability of fiducial reference points

Astrometry involves the identification of reference points within the source images to which the measurements are referred. Obviously a fixed compact calibrator source provides a solid fiducial point for tracking changes of the target position and facilitates the interpretation in multi-epoch observations; the radio core components of AGNs (QSOs) at high red shifts are good candidates to provide such points in the sky, as suggested by the standard theory of extragalactic radio sources (Blandford and Königl 1979) and supported by measurements of the stringent upper limits on the stability of AGN cores of a few μas yr^{-1}.

The temporal stability and uncertainties in the definition of the reference points (within the target *and* calibrator source images) are expected to become the next dominant source of astrometric errors, once tropospheric and ionospheric effects are precisely calibrated out, particularly in observations at low frequencies. The position measurement uncertainty in an image due to thermal noise is given by $\sigma\Delta\theta_{\rm thermal} \approx \theta_{\rm beam}/(1.2\ {\rm DR})$ where DR is the Dynamic Range: the ratio of the flux density at the position of the reference point to the Root Mean Squared (RMS) noise in the maps (Condon et al. 1998). It represents the lower bound of the astrometric error; higher resolution (from observations at higher frequencies and with longer baselines) and higher DR (from higher source flux and higher array sensitivity) result in smaller thermal errors. Larger errors are expected to be related to the effects from underlying source structure and variability, which can introduce temporal changes in the physical conditions at the base of the jet resulting in intrinsic changes

in the position of the core, defined as the region where the optical depth is equal to unity; this effect is known as core-jitter. Moreover, even in the case of a true stationary core, apparent position shifts can arise, for example, from structural changes on scales below the interferometer resolution near the reference point caused, for example, by the ejection of new components at the base of the jet; these are called structure-blending effects. The magnitude of the apparent shifts can depend on the resolution and is expected to change between multi-epoch observations, following the direction of the source axis. Related structure-blending effects must be considered in any comparison between observations at very different resolutions of sources with asymmetrical source structure, even in the absence of any structural changes. We call these extrinsic effects, to differentiate from intrinsic position changes. Observations at higher frequencies and with higher angular resolutions are less vulnerable to this effect; also, these can indicate the onset of the occurrence of this at lower frequencies, where the effects will be larger. In all cases, using multiple background calibrator sources can help identify unsuitable calibrators.

Examples of detailed studies on the stability of the reference points in AGNs are presented in Rioja and Porcas (2000), with upper limits to secular trends ("core motion") along the source axis for quasars 1038+528 A and B $\leq 5\mu$as yr^{-1} and deviations (i.e., core jitter) $<20\mu$as, from 4 epochs of observations spanning 14 years, at 8 GHz. Similar limits were found by Bartel et al. (1986) between 3C345 and NRAO0512 from 12 epochs over nine years and Fomalont et al. (2011) in the relative positions between multiple pairs of quasars in observations spanning one year, at 43 and 23 GHz.

Image quality is important for astrometry and observations should be designed to optimise both source structure and position information. While the improved quality in the measured brightness distributions of sources with next-generation instruments is expected to partially alleviate this effect, careful strategies to mitigate this source of systematic error are mandatory, particularly for high DR observations, i.e., VLBI with SKA; for example, incorporating extra calibrators to allow for cross-checks and considerations of the uv-coverage to recover the source structure. The requirements on the precision of the amplitude calibration required to achieve a DR of 1000:1 are under study, but will undoubtedly have a significant effect at these levels of sensitivity.

2.3 Absolute radio astrometry catalogues and weak reference source searches

For differential astrometry applications a calibrator list with accurate positions of extragalactic radio sources is fundamental and should comprise of a dense grid of sources for all directions and at all frequencies. The most comprehensive catalogue available to date is the third realisation of the International Celestial Reference Frame, ICRF3 (Charlot et al. 2020), adopted by the IAU in August 2018. ICRF3 is the first multi-frequency reference frame ever realised, comprising positions for 4536 sources at S/X band (2.3/8.4 GHz), 824 sources at K band (24 GHz) and 678 sources at X/Ka band (8.4/32 GHz),

where 600 sources have positions available at all three datasets. These positions have been estimated independently at each of the frequencies in order to preserve the underlying astrophysical content behind such positions. The ICRF3 frame shows median positional errors of the order of 100 μas in right ascension and 200 μas in declination, with a noise floor of 30 μas in the individual source coordinates. Since 1994 the VLBA has carried out a sequence of calibrator surveys (VCS-1 to 10) that have provided a more dense grid of calibrator sources at declinations $> -45°$ (e.g., Petrov et al. 2008 and references therein; Petrov 2016). More recently the LBA has performed calibrator surveys for the Southern hemisphere (LCS-1 and 2) (Petrov et al. 2019a, and references therein). These surveys increase the number of known calibrators to 16,466, which can be compared against the number in the ICRF3 catalogue. Note that the ICRF sources have significantly more accurate positions, as they have been regularly monitored for many years; errors in the coordinates of reference sources propagate into astrometric errors.

At the higher frequencies, a Korean VLBI Network (KVN) Legacy program, the Multi-frequency AGN Survey on KVN (MASK), will greatly increase the number of known VLBI calibrators at the highest frequencies. The only previous large high-frequency VLBI surveys were Lee et al. (2008) and Nair et al. (2019), which give a total of 162 detections on VLBI baselines at 86GHz. MASK uses the calibration solutions at the lowest frequencies to extend the coherence-time at the highest frequencies. Data release of the MASK results are expected shortly, and over 600 sources are currently detected at 86 GHz and about half of that number at 130 GHz.

Having a very close calibrator has great benefits but the probability for finding a known reference less than a degree away from the target is still low. Calibrators that can be observed simultaneously with the target are known as 'in-beam' calibrators and the benefits from these can be sufficient that it is worthwhile searching for a previously unknown VLBI source. There are calibrator search strategies for when a suitable catalogued calibrator sufficiently close can not be found. An effective one is to observe in the direction of the target source but cross-correlate the data for the positions of all suitable compact, flat or steep spectrum sources that fall within the FoV of the telescope. In the past this required multiple passes through the correlator, changing the coordinates of the individual pointing centres, thus had a significant impact on the processing time and no more than a few pointings would ever be provided. The breakthrough came with the software correlator DiFX-2 (Deller et al. 2011), which could form multiple phase centres at the first averaging stage on the intermediate data products. This massively reduced the computational cost, and DiFX-2 has been used to correlate hundreds of individual phase centres from a single experiment (e.g., 556 phase centres in the Orion Star Forming Region, Forbrich et al. (2020, submitted)). Recently LOw Frequency ARray (LOFAR) long-baseline studies have proposed strategies to find suitable compact calibrators for hither-to unexplored low frequency ranges (see Moldón et al. 2015; Jackson et al. 2016). They find the source density to be about 1 suitable source per sq. deg. at 150 MHz.

3 Established precise astrometric calibration methods

Table 1 Indicative temporal sequence of source/frequency scans in observing schedules, for implementation of some of the astrometric techniques discussed in Sects. 3 and 5. Conventional phase referencing (PR) with source switching, in-beam PR with simultaneous source observations, Advanced Tropospheric Calibration with Geodetic blocks (ATC), MultiView (here with source switching but could also be simultaneous), SFPR with two sources (here with simultaneous multi-frequency observations but could also be with fast frequency switching) and MFPR, here with simultaneous multi-frequency observations and ICE-blocks, using only the target source. 'P, R, T' are the scans on the primary calibrator, reference and target sources, respectively; 'G' stands for the GeoBlocks. '–' represents frequency switching, '$\cdots$' represents source switching and one over the other represents simultaneous source/frequency observations. Multiple calibrators combined in the analysis with different weights is represented by $\Sigma_i \alpha_i$, where α_i are real values. Different frequencies ν are indicated by the subscripts R and T for reference and target frequencies respectively, and i, j and k for the ICE-block calibration.

PR	$P \cdots R \cdots T \cdots R \cdots T \cdots R \cdots T \cdots R \cdots$
In-beam PR	$P \cdots \frac{R}{T} \quad \frac{R}{T} \quad \frac{R}{T} \quad \frac{R}{T} \quad \frac{R}{T} \quad \frac{R}{T} \cdots$
ATC	$P \cdots R \cdots T \cdots R \cdots G \cdots R \cdots T \cdots R \cdots$
MultiView	$P \cdots \Sigma_i \alpha_i R_i \cdots T \cdots \Sigma_i \alpha_i R_i \cdots T \cdots \Sigma_i \alpha_i R_i \cdots$
SFPR	$P \cdots T(\frac{\nu_R}{\nu_T}) \cdots R(\frac{\nu_R}{\nu_T}) \cdots T(\frac{\nu_R}{\nu_T}) \cdots R(\frac{\nu_R}{\nu_T}) \cdots$
MFPR	$P \cdots T(\frac{\nu_R}{\nu_T}) - T(\nu_i - \nu_j - \nu_k) - T(\frac{\nu_R}{\nu_T}) \cdots$

3.1 Conventional PR astrometry

The standard approach for phase-based astrometric measurements of a program source (A) consists of using interleaving observations of a nearby calibrator source (B), which is separated up to a few degrees, at the same observing frequency, ν. This approach has been used since the beginnings of phase-based differential or relative astrometry in the 1970s; here we refer to it as conventional relative astrometry (or conventional PR, or simply PR). See Table 1 for an indicative observing schedule.

Following Eq. (2) for the differential phase observables, with $\mathcal{R}$=1 and $\nu_R = \nu_T = \nu$, the PR-calibrated dataset is given by:

$$\phi_T - \mathcal{R}\phi_R = \phi_A(t_1, \nu) - \phi_B(t_2, \nu) = (\phi_{A,\mathrm{pos}} - \phi_{B,pos}) \pm \sigma\phi^{PR} \pm \sigma\phi_{\mathrm{thermal}} + 2\pi\Delta n \qquad \Delta n \in \text{integer}$$

where the indexes A and B refer to the two sources; $(\phi_{A,\mathrm{pos}} - \phi_{B,pos})$ is the astrometric term of interest, for a precise measurement of the angular separation between both sources at the observing frequency ν and $\sigma\phi^{PR}$ stands for the conventional PR calibration errors.

Note that, in general, the observations of A and B are carried out at different times and along different lines of sight. The source switching interval (T_{swt}) and pair switching angle ($\Delta\theta_{AB}$) are crucial parameters to determine the quality of the compensation of the temporal and spatial structure of the residual errors in the term $\sigma\phi^{PR}$, respectively. A careful planning of the observations

is the first step towards improving the astrometric accuracy, by prioritising the compensation of the dominant errors at the observing frequency: fast tropospheric fluctuations in the high frequency regime (i.e., with short $T_{\rm swt}$) and ionospheric spatial gradients above the antennas in the low frequency regime (i.e., with small $\Delta\theta_{AB}$). In practise, the best outcome comes from taking both considerations into account.

The magnitude of the dominant contributions to $\sigma\phi^{PR}$ are given by Eq. (3) using $T_{\rm swt,tro} = T_{\rm swt,ion} = T_{\rm swt}$ and $\Delta\theta_{tro} = \Delta\theta_{\rm ion} = \Delta\theta_{AB}$. The resultant astrometric error $\sigma\Delta\theta_{AB}$ for the high and low frequency regimes, using the approximation as described in Sect. 2.1, are given by:

$$[\sigma\Delta\theta_{AB}]^2 \sim [\frac{\Delta\ell_z}{|b|}\ \sec Z_g \tan Z_g \Delta\theta_{AB}]^2 + [O_{\rm ion}(\frac{\Delta\ell_I}{|b|\nu^2}, \Delta\theta_{AB})]^2 + [O_{\rm geo}(\Delta\theta_{AB})]^2 + [\sigma\Delta\theta_{\rm thermal}]^2;\ \ \nu > 8{\rm GHz}$$

$$[\sigma\Delta\theta_{AB}]^2 \sim [\frac{\Delta\ell_I}{|b|\nu^2}\ \sec Z_F \tan Z_F \Delta\theta_{AB}]^2 + [O_{\rm tro}(\frac{\Delta\ell_z}{|b|}, \Delta\theta_{AB})]^2 + [O_{\rm geo}(\Delta\theta_{AB})]^2 + [\sigma\Delta\theta_{\rm thermal}]^2;\ \nu < 8{\rm GHz}$$

where $\Delta\ell_I$ is the residual ionospheric excess path length at 1 GHz equal to $40.3\Delta I$ cm (Sovers et al. 1998), which corresponds to 2.4 m for the typical value of ΔI=6 TECU. Terms in $O()$ represent smaller contributions. Then, for example, for $|b|$=6,000 km, Z ∼40°, atmospheric errors of $\Delta\ell_z$ ∼5 cm and ΔI=6 TECU gives astrometric accuracy $\sigma\Delta\theta_{AB}$ ∼30μas per degree of pair angular separation (hereafter μas/deg), for strong sources, at ν >8GHz. Note that the (astrometric) accuracy is frequency independent in the high frequency regime, being dominated by non-dispersive tropospheric fluctuations. Instead, in the low frequency regime it is frequency dependent as a consequence of the dominant dispersive ionospheric fluctuations. With the parameters as above, $\sigma\Delta\theta_{AB}$ ∼63μas/deg and 800μas/deg at 5GHz and 1.4 GHz, respectively. Smaller contributions from the thermal noise astrometric errors amount ≤10μas at $\nu \geq$ 10 GHz and ∼20μas and ∼100μas at 5 and 1.4 GHz (L-band), respectively, for DR 100:1.

The current scope of application of PR is in the moderate frequency regime from ∼ 1.4 and up to 43 GHz (with the single unique exception at 86 GHz, Porcas and Rioja 2002), albeit with a rapidly deteriorating performance and usability towards the edges, particularly in the low frequency regime. The upper frequency limit is imposed by the increasingly fast tropospheric fluctuations and the mechanical limitations of the telescopes to perform source switching within the short coherence times, along with sensitivity considerations and scarcity of calibrators. The lower frequency limit arises from the increasingly large spatial ionospheric disturbances, which result in very large calibration errors.

Our definition of PR applies to both phase reference mapping and differential phase delay astrometry techniques. Rioja and Porcas (2000) made a detailed comparison of these approaches and showed that the two methods produce equivalent results, albeit there are differences between them. Differential phase delay astrometry requires direct detection of both sources, which are

then modelled using a least-squares-fitting procedure to determine the source coordinates, and possibly also other parameters used in the a-priori models, which in principle allows for larger angular separations. In phase-reference mapping it is sufficient to detect one of the two sources, therefore it is also applicable for imaging sources too weak for self-calibration. The Fourier transform approach determines the source coordinates only, but has the advantage of being very easy to use and therefore has been very widely applied. Both methods have evolved since their first implementations e.g., VLBI3 (Robertson 1975) to UVPAP (Martí-Vidal et al. 2008) for differential phase delay astrometry and SPRINT (Lestrade et al. 1990) to AIPS (Greisen 2003), VEDA (VEra Data Analyzer Nagayama et al. 2020) or now VLBI-capable CASA (van Bemmel et al. 2018), for phase reference mapping.

Improved instrumental backends and clock stability, rapid switching and settling capabilities and massively increased receiver bandwidths and recording rates (i.e., sensitivity), improved the probability of finding a close calibrator and reducing $\Delta\theta_{AB}$ and $T_{\rm swt}$; the primary calibration mechanism in PR. Furthermore the more complete astrometric catalogues, improved geometric parameters (station coordinates, reference source coordinates, EOP, UT1 and so on) and tropospheric and ionospheric modelling have led to an overall improvement in the astrometric performance, but not any conceptual change from that in its inception (e.g., Shapiro et al. 1979; Alef 1988).

Further improvements have come from dedicated engineering solutions, such as the dual-beam system of VERA that allows for simultaneous observations of pairs of sources up to 2.2° apart, i.e., $T_{\rm swt}$=0. Looking ahead, the increased sensitivity with the next-generation instruments and arrival of innovative technologies to extend the FoV of large single telescopes and arrays and superior frequency agility will result in even better performance. The overall astrometric performance can be improved using advanced strategies and instruments that enable them, as discussed in the following sections.

3.2 In-beam PR astrometry

In-beam PR astrometric VLBI refers to a particularly favourable configuration of conventional PR where the target and the calibrator sources lie within the primary beam of the telescopes (hence the name "in-beam") and can be observed simultaneously. See Table 1 for an indicative observing schedule. This configuration results in a superior error compensation, as a result of small $\Delta\theta_{AB}$. For extremely close sources, the differential analysis can reach the thermal noise limit, $\sigma\Delta\theta_{\rm thermal}$ and results in μas astrometry. The first demonstrations of in-beam PR astrometry with μas-level systematic errors at $\sim$8 GHz, and few tens of μas at $\sim$2 GHz, date from the 1980's using 1058+328A/B, a pair of sources 33″ apart (Marcaide and Shapiro 1984; Rioja 1993; Rioja et al. 1997a).

The considerations for in-beam PR astrometry are largely unchanged since then, but the prospects for in-beam PR, particularly at low frequencies, have

improved because the probabilities for finding suitable in-beam calibrators in the direction of a target of interest have increased significantly. This is a result of observations with higher sensitivity, advances in (weak) calibrator search methods (see Sect. 2.3) and multi-stage analysis using weak nearby calibrators (Fomalont et al. 1999). Currently it is regularly possible to find a suitable calibrator source within the FoV of the 25-m VLBA dishes at 1.4 GHz (i.e., $\sim 30'$) in any arbitrary direction (e.g., in Deller et al. (2019) the minimum calibrator flux density was 5 mJy.) This has had a significant impact, particularly in the low frequency regime, where PR astrometry has very large errors ($\sim$1 mas/deg at L-band). At L-band a nominal goal of 100μas per epoch (or equivalent differential delay errors $\sim$3 mm) can be achieved with a reference source $\leq 10'$ away from the target, following Eq. (3) for the systematic residual ionospheric errors. This would match the typical thermal astrometric limits with current instruments assuming a DR of 100:1.

However the larger uncertainties in the absolute coordinates of weak reference sources is a consideration for the astrometric accuracy and should be taken into account. In science cases that rely on the changes in the sky position of the target across multi-epoch observations (i.e., parallax, proper motion) these uncertainties introduce a constant offset and so are of little relevance. In all cases, for the astrometric error budget one has to take into account the increased thermal noise errors arising from weak sources, along with the systematic residual errors.

In-beam PR astrometry is suitable at any frequency, although the probability of finding a calibrator within the smaller FoV of the telescope at higher frequencies, and shorter coherence times, becomes very low. Table 2 lists the number of sources one would expect to find within the FoV of a 20m radio telescope, with the sensitivity levels of current instruments (Col. 6) and SKA (Col. 8), for a range of frequencies. Therefore at high frequencies >8 GHz even with SKA Phase-2 or ngVLA, the usability of in-beam PR continues to be extremely limited and unless one is lucky, one would have to slew between the source pair, even with next-generation instruments.

If the target and calibrator sources can be co-observed there is no source switching and one would assume that $T_{\rm swt}$ would be zero, nevertheless we note that this term also encompasses the solution interval on the calibrator. In-beam calibrators tend to be weaker, the thermal limits dominate the error budget and $T_{\rm swt}$ becomes the calibration solution interval.

The ideal instrumental requirements to benefit from in-beam PR are high sensitivity, such as provided by large powerful telescopes, and wide FoV, such as provided by small telescopes. This contradiction can be addressed with new technology developments to enlarge the FoV, e.g. using receivers with multiple-pixel capabilities (such as PAFs or multi-beam feeds) on large single telescopes, and the capabilities for multiple tied-array beams in the directions of nearby sources with antenna arrays, as shown in Fig. 1. These are discussed later in Sect. 7.

Table 2 Table to characterise the performance of MultiView and its feasibility for current and next-generation instruments, across the spectrum. Col. 1 is the observing frequency, Col. 2 is the spatial resolution for a 6,000km baseline. Col. 3 is the estimated systematic astrometric error using MultiView, as discussed in Sect. 7.2.4. Col. 4 is the required DR for a matching thermal-noise astrometric error ($\sigma\Delta\theta_{\rm thermal}$). Col. 5 lists the source fluxes that are 100 times the 1 hour image sensitivity with current VLBI arrays (derived from EVNCalc with bandwidths of 16MHz at $\nu < 1$ GHz, 128MHz at 1.6 GHz, otherwise 256MHz). We use DR 100:1 as it is a typical value with current instruments. Col. 6 is the number of sources, with fluxes larger than Col. 5, expected within the FoV of a single pixel 20m antenna if FoV $\leq$1°, otherwise 1° (marked with †), using the parameterisation from Bonaldi et al. (2019). Col. 7 lists the source flux that is the matching DR value (Col. 4) times the 1 hour image sensitivity with SKA-VLBI Phase-1 (taken from Garcia Miro (2019) for the full array combined, 256MHz for SKA1-Low, 2GHz for SKA1-Mid). Col. 8 is the number of sources, with fluxes larger than Col. 7, expected within the FoV of a single pixel 20m antenna if FoV $\leq$1°, otherwise 1°(marked with †). For the higher frequencies we also included in brackets the number of in-beam sources that could be expected for SKA-Phase 2. The number of in-beam sources for ngVLA observations would fall between these two values. Based on Col. 6 and 8, in-beam MultiView would be feasible at frequencies <1.4, <2 and <6.7 GHz, with the sensitivities of current VLBI, SKA-VLBI Phase 1 and Phase 2, respectively, and with switched MultiView at higher frequencies. Therefore the astrometric performance can be significantly improved with the next-generation instruments and MultiView, reaching the MultiView astrometric precision in Col. 3.

Frequency ν (GHz)	Resolution $\theta_{\rm beam}$ (mas)	MV error $\sigma\Delta\theta^{MV}$ (μas)	Matching DR	$\Delta I_{\rm m}^{\rm current,1h}$ ×100 (mJy/beam)	No. of in-beam sources	$\Delta I_{\rm m}^{\rm SKA,1h}$ × DR (mJy/beam)	No. of in-beam sources
0.3	34	150	230	120	1.2†	5.1	14†
0.9	11	17	674	20	3.5	3.1	15
1.6	6.4	6	>1000	4.9	2.9	2.1	5.5
5.0	2.1	∼1	>1000	2.3	0.4	2.4	0.4 (6)
8.0	1.3	∼1	>1000	3.6	0.1	2.6	0.1 (2)
15.0	0.7	∼1	687	6.0	0.0	3.0	0.0 (0.4)

3.2.1 Stacking to increase SNR

Hybrid Double Mapping (HDM) (Rioja and Porcas 2000) is an alternative astrometric path to in-beam PR, where the signals from both sources are combined or stacked into a single hybrid dataset to increase the SNR; hence this is an advanced strategy of interest for weak sources. In HDM the hybrid dataset preserves the signature of the relative (astrometric) separation of the source pair, which can be measured directly from the compound-image produced using self-calibration algorithms to solve for the common antenna based phase and phase derivative residual errors. HDM was demonstrated for a close pair of sources, 33″ apart, using the point-by-point sum of the reference and target source visibilities, at 8.4 GHz, and the results agreed with those from in-beam PR. A more recent demonstration, performed in the low frequency regime, is Multi-Source Self-Calibration (MSSC) (Radcliffe et al. 2016) that combines the signals from multiple weak targets that lie within the FoV, to increase the SNR and allow self-calibration. In this case the relative astrometry is preserved between the ensemble of sources, as long as direction-dependent effects are not significant.

3.3 Advanced PR calibration strategies

Atmospheric effects are one of the most poorly understood components in the a priori theoretical model of VLBI observables, and are the dominant source of astrometric errors. This section is concerned with 'advanced' strategies to improve the tropospheric and ionospheric modelling (i.e., reduce typical a priori model errors $\Delta\ell_z$ and ΔI in Eq. (3)). Improved model values in PR result in equivalent benefits to using a smaller $\Delta\theta_{AB}$, that is achieving higher astrometric accuracy, but with widely separated sources. We dub this approach advanced PR astrometric techniques. Because the nature of tropospheric and ionospheric effects are very different, the advanced strategies are specific for application in the high and low frequency regimes. We refer to these as Advanced Tropospheric and Ionospheric Calibration strategies (ATC and AIC, respectively). These comprise using either dedicated blocks inserted during the VLBI observations, the program data itself or external measurements from an independent technique.

Huge strides have been taken in the last two decades, particularly at the higher frequencies. ATC strategies can reduce typical tropospheric errors for $\Delta\ell_z$ from several cm to the level of $\sim$1 cm. These tropospheric strategies fail at lower frequencies ($\leq$8 GHz) where the dispersive ionosphere is the dominant contribution. The ionospheric disturbances have a high degree of spatial structure, which is responsible for the direction-dependent calibration errors and can not be accurately modelled with a single global value at the Zenith of the telescope. GPS-based TEC global models have errors of about $\sim$10-20% (e.g., Hernández-Pajares et al. 2009), or typical nominal residual errors of ΔI $\sim$6 TECU (Walker and Chatterjee 1999). Such ΔI correspond to an excess path error of 1 m at 1.5 GHz, which is a hundred-fold larger than the best tropospheric residual errors, and scales as ν^{-2}. The AIC strategies improve the ΔI estimate for the line of sight. Here we discuss advanced strategies which can reduce ΔI to $\sim$0.1 TECU.

3.3.1 Advanced Tropospheric Calibration methods

Dedicated tropospheric blocks: The "GeoBlocks" method (Brunthaler et al. 2005; Reid et al. 2009) uses dedicated blocks of observations ($\sim$30 minutes long, scheduled every 3-4 hours) interleaved with the program observations to improve the a-priori value of the tropospheric model. See Table 1 for an indicative observing schedule. The GeoBlocks comprise observations of multiple ICRF sources following a geodetic-like schedule and analysis. That is, strong sources are selected which cover a wide range of Zenith angles, and are observed in short scans in rapid succession with wide bandwidths. The derived group delays are used to solve for the Zenith path length error plus clock errors, for each station. These estimates, mapped to the corresponding elevations, are used to remove the tropospheric static component from the program observations and the differential observables.

Such an approach can reduce the value of tropospheric zenith delay residual errors to $\Delta\ell_z \sim 1$cm, which leads to 10μas/deg relative astrometric errors at moderate antenna elevations (i.e., $Z \sim 45°$ and above). Nevertheless, the differential residual errors at low elevations, amplified by the $\sec Z \tan Z$ term in Eq. (3), can become very large. For example, at a zenith angle $Z \sim 60°$ the systematic errors are eight times larger than those at $Z \sim 45°$, which leads to 80μas/deg relative astrometric errors.

Due to the relative simplicity of the implementation of the GeoBlock strategy, and its versatility and universal application, this approach has led to a significant expansion and has had a major impact in the field of precise astrometry at frequencies around ∼22 GHz, spreading the application of astrometry to many diverse fields (see the references in Reid and Honma 2014). The GeoBlocks superseded earlier approaches by the same team (Reid et al. 1999) that fitted the residual differential phases of the program observations to correct for a tropospheric zenith delay error per station; this method required strong program sources and the estimates, using a single pair of sources, were less precise. Other approaches comparable to GeoBlocks involve using an image optimisation algorithm, simultaneous tropospheric measurements from co-located GPS receivers (see the comparative study in Honma et al. 2008) or Water Vapour Radiometer (WVR) systems (Roy et al. 2006).

Xu et al. (2018) showed the benefits from the combined use of the methods above, compared to outcomes from each individual method, when applied to challenging low elevation observations. We highlight the GeoBlocks and image optimisation calibration strategies for their widespread usage on many targets over a wide scope of research, and as drivers of astrometric surveys, i.e., the VLBA BeSSeL and VERA Key Science Program (KSP) projects, respectively.

Residual Minimisation of Program Observations: The differential phase delay astrometry method uses a least squares fitting of the program observations to estimate the astrometric source coordinate parameters, that can also include fitting of the residual tropospheric zenith path length per telescope, among other parameters.

The University of Valencia Precision Astrometry Package (UVPAP) software is an upgraded version of the VLBI3 program (Robertson 1975), which incorporates new capabilities such as a more robust automatic algorithm to solve for phase ambiguities, using closure conservation conditions for triangles of telescopes, and increased processing capability for a joint fit of the observations of multiple source pairs simultaneously (Martí-Vidal et al. 2008). The former is fundamental to determine the unambiguous observables. The latter can reduce the residual zenith excess path length to the order of $\Delta\ell_z \sim 1$ cm from the added constraints, particularly if the program observations span a significant range of elevations in a rapid temporal succession (see discussions in Martí-Vidal et al. 2016). This is comparable to the outcome from GeoBlocks.

3.3.2 Advanced Ionospheric Calibration methods

S/X group delay correction: The extremely well established geodetic VLBI technique of obtaining an 'ionosphere-free' visibility data, by combining group delays from S-band (2.4GHz) and X-band (8.4GHz) from simultaneous dual-frequency observations, is one of the oldest AIC methods. This was also the most common method for relative astrometry, using S/X observations of the pair of sources, particularly before the availability of GPS derived corrections. Using this approach one can reduce the residual ionospheric errors to ΔI$\sim$1.5 TECU (Ros et al. 1999). We note that these results were achieved without applying a-priori GPS-based corrections, so the initial errors would have been up to ΔI$\sim$40TECU. Ionospheric corrections derived from S/X observations of source pairs have been shown to be significantly better than those from GPS-corrected analysis (Walker and Chatterjee 1999). This method, however, includes the implicit assumption that the source positions have a linear dependence on wavelength (see Porcas 2009, for discussions of this). VLBI observations corrected by direct dispersive delay measurements have not been used much recently, as only the Geodetic (i.e., S/X) single polarisation receivers supported such simultaneous dual-frequency observations. However, with the adoption of wideband cm-wave receivers (see Sect. 7.1.2) on the next-generation of telescopes, this situation is sure to be reversed and this and related approaches will see a regeneration.

Phase-Fitting: An alternative to the S/X group-delay ionospheric method to measure ΔI for each antenna, is to fit the differential residual phases for the dispersive ν^{-1} signature, over the observed frequency range. The improved estimate for ΔI is used to eliminate the ionospheric contribution from the target data. Special considerations are required to avoid phase-fitting problems related to the inherent ambiguity of the phase observable. This method has been demonstrated for pulsar parallax measurements, with VLBA observations of multiple pairs of sources separated a few degrees apart, at L-band. (Brisken et al. 2000; Brisken 2001; Brisken et al. 2002). The approach consisted of making initial phase-referenced snapshot images of the target sources at each sub-band of the frequency span (1.4 – 1.7 GHz) using conventional phase referencing imaging. The astrometric errors in the phase referenced images are expected to be at $\sim$mas level and changing between sub-bands. By fitting the (sub-band) antenna based phase residuals across the frequency span to a function comprising a point-source model with a non-dispersive (i.e., scaling with ν) and a dispersive (i.e., scaling with ν^{-1}) term, one can determine the ΔI ionospheric errors per antenna as a function of time (Brisken et al. 2002). These are used to correct the differential phases and improve the accuracy of the astrometric measurement. Note that the initial phase referenced image is vital to ensure that there were no ambiguity issues in the fitting of phases across the band. Alternatively the residual ionospheric errors can be determined from the characteristic frequency dependent (i.e., dispersive) position-shift signature measured in the image domain. That is, by measuring

the position changes in the snapshot images of the program source across a range of frequencies. The image-based approach improves the signal strength by combining the inputs from across the VLBI array; in this case average ionospheric wedges over the array (or more often a subset of the array) as a function of time could be derived (Brisken et al. 2000).

The residual ionospheric error ΔI after these fitting strategies could be as low as 0.1 TECU (estimated from Brisken et al. 2000, Fig. 4), a fifty-fold improvement over the nominal residual values after GPS-based corrections. With this level of systematic errors one could imagine achieving 10μas/deg astrometry precision at L-band, provided the signal was sufficiently strong. Nevertheless, the complexities of the analysis and the thermal limits of the snap-shot phase-referencing imaging of the pulsars has hither-to prevented wide adoption of this method. Furthermore, this method includes the implicit assumption that the source positions have no dependence on wavelength, which is true for pulsars but not generally true for AGNs. However, with the sensitivity of the next-generation instruments, both due to increased collecting area and wide bandwidths, it is possible that these approaches may yet be useful again.

Dedicated ionospheric blocks: Section 5.3 on multi-frequency phase referencing (MFPR) describes a related multi-frequency approach for reducing ΔI to a fraction of a TECU using dedicated blocks interleaved with the program observations, on the target source; we dubbed this strategy "ICE-blocks" (Ionospheric CorrEction, to resonate with the GeoBlock method for the troposphere). Such strategies should be widely applicable (as for GeoBlocks) thus improving the performance and applicability at low frequencies.

3.3.3 Concluding remark on advanced astrometric calibration methods

A precise astrometric strategy requires high quality spatial and temporal phase calibration solutions. The ATC and AIC strategies presented above have had a large impact in the field of astrometry with PR, particularly in the high frequency regime. Still, the scope of PR-related applications remains unchanged, with an upper frequency limit of 43 GHz. Sections 5.2 and 5.3 discuss methods that allow for precise astrometry above this limit. At low frequencies, the AICs can provide a path to exquisite improvements in the ionospheric calibration. Nevertheless, its implementation is limited by the multi-frequency capabilities of current instruments and as a result precise astrometry at the low frequency regime is driven by in-beam PR, which has a more limited applicability compared to ATC. Both AIC and ATC are able, in principle, to deliver astrometric precision at 10μas/deg level, although in practise this precision has been largely limited to the tropospheric corrections and the high frequency regime, to date. Sect. 5.1 presents a new technique (i.e., MultiView) for ultra precise astrometry with next-generation instruments, which works for both tropospheric and ionospheric corrections for the high and low frequency regimes and is not dependent on a strong target source.

4 The next-generation of radio instruments and the opportunities for astrometry

We present a short summary of the next-generation instruments that are coming online, which will drive forward the field of ultra-precise astrometry with VLBI observations. Table 3 lists crucial parameters for some of these and current arrays. This review is primarily interested in the considerations for astrometric surveys, therefore we have focused on the relevant issues for those. We emphasise our views on the impact that these new instruments can have, in conjunction with established and innovative astrometric methods and technologies.

Table 3 Summary table of some of the current VLBI arrays and next-generation elements with VLBI compatibility (Col. 1) mentioned in this review. Col. 2 and 3 list the frequency range and collecting area. Col. 4 shows the capability for multi-beams, indicating if this is available via formation of simultaneous multiple-pixel beams or by alternating between sources (Yes or Switching, respectively). Col. 5 shows the capability for multi-frequencies, indicating if this is available via observing multiple frequencies simultaneously, by fast frequency switching or not available (Yes, Switching or No, respectively). The VLBA is a full time dedicated VLBI array, formed of 10 25-m antennas, of which 8 can observe at the highest frequency of 86 GHz. EVN is an ad-hoc array, with some large antennas (3>60m) and many (9 for these calculations) smaller ones. x-KVN stands for KaVA (KVN and VERA array) plus Yebes (40m). VERA is the Japanese astrometric array. For the next-generation VLBI elements, the collecting areas of SKA-Low and SKA-Mid Phase-1 are given; Phase-2 values are given in brackets. ngVLA is proposed to also be a standalone VLBI array, by absorbing the VLBA sites. FAST is the 500m diameter Chinese single dish and SKA pathfinder. †: not continuous for current arrays; ⋆: frequency dependent, as not all stations support all frequencies. ♢ KVN only.

Name	Frequency Range†	Collecting Area*	Multi-Beams	Multi-frequency
Current VLBI Arrays				
VLBA	0.3 to 86 GHz	6,000 m^2	Switching	Switching
EVN	0.3 to 43 GHz	28,000 m^2	Switching	No
x-KVN	22, 43, 86, (130$^{\diamond}$) GHz	4,000 m^2	Switching	Yes
VERA	22, 43	2,000 m^2	Yes	Yes
Next-Generation VLBI elements				
SKA-Low	50 to 350MHz	0.4 (1) km^2	Yes	Yes
SKA-Mid	0.35 to 15GHz	0.04 (1) km^2	Yes	Switching
ngVLA	1.2 to 120GHz	0.1 km^2	Yes	Maybe Yes
FAST	0.07 to 3GHz	0.1 km^2	Yes	No

4.1 m and cm radio astrometry in the SKA era

The Square Kilometre Array (SKA) is an international collaboration to build an array with a collecting area that will be eventually a hundred times greater than current facilities. It is being built in two stages, an initial roll-out (Phase-1) and then the final full array (Phase-2). It comprises of two arrays and frequency ranges, SKA-Low covering 50 to 350MHz, sited in Western Australia, and SKA-Mid covering 0.35 to 15.3 GHz (and potentially higher), sited in

South Africa and eventually eight other African countries. SKA-Low Phase 1 will consist of 512 stations each of 256 log-periodic dipoles (equivalent to ∼40% of the full SKA-Low), spread over a diameter of 65 km. SKA-Mid Phase 1 will consist of 197 ∼15m offset-Gregorian parabolic dishes (equivalent to ∼3.5% of the full SKA-Mid), spread over a diameter of 150 km. The full SKA will have baselines of thousands of km, and can be considered a VLBI instrument in its own right.

The arrival of SKA has revitalised the research at m to cm wavelengths in many fields (Braun et al. 2015) and this includes a long baseline component. To exploit the full potential of the first phase, both SKA-Low and SKA-Mid will perform joint observations with other telescopes, hereafter SKA-VLBI. These can potentially perform high precision astrometry (providing the mechanisms are in place). Given the collecting area of the SKA telescope, which will be an order of magnitude (Phase-1) to two orders of magnitude (Phase-2) times greater than that available currently, the sensitivity of VLBI baselines from existing infrastructure to the SKA is expected to increase by an order of magnitude or more with respect to current levels; this offers a great opportunity for VLBI studies.

Observations with SKA-Low will be dominated by ionospheric systematic propagation effects, with spatial variations at scales much smaller than the wide FoV of the individual dipole elements. Each SKA station has a diameter of 38m (and a FoV from 15 to 1.3°), and can form multiple station beams towards any point visible to the individual elements. Multiple tied-array beams can be formed within these station beams, from the sum of the station outputs; the current specifications are for 4 full bandwidth coherent VLBI beams. The backend processing hardware can support a maximum of 16 full bandwidth VLBI beams, but this would require an increase in the number of planned VLBI servers.

The frequency range for SKA-Mid observations comprises regimes with dominance of either the ionospheric or tropospheric systematic propagation effects, and a regime where both are significant. The SKA-Mid dishes have a significantly smaller FoV on the sky than for SKA-Low, but will still see nearly 4° at the lowest frequency. Similar backend hardware is planned for SKA-Mid as for SKA-Low, but with the greater instantaneous bandwidth for SKA-Mid a smaller number of tied-array beams can be formed. Currently 4 full bandwidth (2GHz) coherent VLBI beams would be possible; the number of beams can be increased by compromising on the bandwidth (for details see Garcia Miro 2019).

With the phased-up SKA Phase-2 acting as an extremely sensitive station in a VLBI array the sensitivity for the SKA baselines will be an order of magnitude better than those for the best 100m-class radio telescopes available today (see Table 3). Furthermore the capability to tie together all the outputs of the stations to form multiple tied-array beams for VLBI (and also pulsar studies) will be essential for the science cases which require astrometry with SKA-VLBI, as a number of simultaneous tied-array beams are vital to obtain highly precise outcomes; moreover this will allow VLBI surveys to be

performed. Whilst the VLBI baselines will still be Earth bound we may reasonably assume that the achievable sensitivity will be ten times better than current limits, achieving dynamic ranges (DR) of ∼1000:1. We note that nearly such levels are being achieved currently for a few objects (Yang et al. 2016; Miller-Jones et al. 2020). A thousandth of the beamsize, if the observations are thermally limited, would potentially allow for 8μas astrometric precision at L-band (∼1.4GHz) and 1μas precision at X-band (∼8.4 GHz), with global baselines of 6,000 km; Sect. 4.4 discusses Space-VLBI possibilities that allow for much longer baselines. These limits would open up a huge parameter space for SKA-VLBI to explore, in a multitude of scientific fields (see Paragi et al. 2015). However this is predicated on the actual measurements matching the potential astrometric accuracy. MultiView is a calibration method that can provide the matching accuracy as discussed in Sect. 5.1. Sect. 9 describes some of the science cases for SKA-VLBI where ultra-precise astrometry is key.

The SKA precursors and pathfinders play an essential role in developing and demonstrating the SKA technologies and techniques now, before the instrument is finalised. A number of them have performed a limited amount of VLBI. The LOFAR has made long baseline observations (e.g., Jackson et al. 2016) between the international stations. The Murchison Widefield Array (MWA) has performed VLBI in conjunction with the Indian Giant Metrewave Radio Telescope (Kirsten, per. comms). MeerKAT has formed fringes between their stations and the European VLBI Network (EVN). ASKAP has plans for a VLBI beam-former. The massive boost in low frequency astrometry that will be provided by the FAST telescope (China, 500m diameter), the world's most sensitive radio telescope (Li and Pan 2016), should be noted. FAST is a SKA pathfinder with a collecting area similar to SKA Phase-1, which makes it highly desirable for joint VLBI astrometric observations; see Table 3. The narrow FoV and limited pointing capabilities put a constraint, in principle, on VLBI astrometric measurements. Nevertheless it is currently equipped with a 19-beam receiver, which could enable precise astrometry using MultiView. The multiple-pixel effectively extends the narrow FoV to that of a 30m diameter single pixel telescope. There are plans to install a Phased Array Feed (PAF), which will result in an even better performance with denser coverage of the FoV and wider bandwidths. Detailed discussions on the impact of technological developments, such as multiple-pixel capability, on astrometry are to be found in Sect. 7.

4.2 cm and mm radio astrometry in the ngVLA era

The next-generation VLA (ngVLA) project is an American proposal for a cm to mm antenna array (Murphy 2018). It includes long baselines, spanning at least ∼500 km, and covers the frequency range from 1.2 to 120 GHz (Murphy et al. 2018), with a planned collecting area larger than SKA-Mid Phase-1. The ngVLA will be built out from the current VLA site in New Mexico, which is a high and dry plane with a good view of most of the sky. It consists of a dense

core of 160 close-packed 18m diameter parabolic antennas, almost completely covering the inner kilometre, then transitioning to a log spiral pattern out to 20km in radius. Longer baselines, with a further 50 or so antennas, then extend across Southern USA, and even into Mexico (Selina et al. 2018). Furthermore, the VLBA sites are envisaged as being added to this, with two to three dishes at each site, to increase the sensitivity of these longest baselines; see Table 3. The receiver systems sit at the off-axis Gregorian focus, and the proposed design has six feeds for six bands with a very fast translator, which allows switching between frequencies on the timescale of seconds. Such an instrument will be an exciting partner for SKA and the Atacama Large Millimeter/submillimeter Array (ALMA) .

ngVLA, with baselines of at least 500 and potentially 8,000km, is essentially a VLBI instrument with spatial resolution at the milliarcsecond scale. ngVLA has larger dishes than SKA-Mid and is not envisaged as a survey instrument. As such it is well matched in both capabilities and in organisation to be an outstanding VLBI instrument (Reid et al. 2018). With the enhanced sensitivity from a phased-up core and wide recorder bandwidths, multiple calibrator sources within the FoV of an antenna could be expected to be found for most directions up to frequencies of ∼8GHz, where the FoV would be 0.1°(see Table 2 for the predicted number of sources to be found in a primary beam). ngVLA will be able to output multiple tied-array voltage streams for simultaneous observations of multiple sources within the FoV (Selina et al. 2018). In general at higher frequencies (>8 GHz) astrometry would be carried out with source switching, and the telescopes are being designed with the capability to switch rapidly between different lines of sight (4° in 10 sec). With these capabilities ngVLA is highly suitable for observations using the latest astrometrical techniques, such as MultiView as discussed in Sect. 5.1.

Astrometry at high frequencies using conventional techniques is extremely challenging, due to the fast fluctuations of water vapour in the troposphere. Water Vapour Radiometer (WVR) systems, which have proved invaluable on the ALMA site, will monitor the precipitable water vapour content in the direction of the antenna pointings to improve the estimates of the tropospheric model contributions. Nevertheless there are significant risks in depending entirely on this approach. The WVR for ngVLA will be using the less sensitive 22GHz line, rather than that at 183GHz used for ALMA, and this tends to saturate and has a spotted history (Clark 2015).

Innovative methods to correct for the tropospheric effects that use multi-frequency observations, i.e. Source Frequency Phase Referencing (SFPR), are described in detail in Sect. 5.2. The ngVLA feed translator enables very fast switched-frequency observations (significantly faster than currently possible with the VLBA). However, this is a sub-optimal solution; the best solution is to have simultaneous observations at multiple frequencies. These provide enhanced coherence at the highest frequencies and more robust and straightforward operations. In the design of a Gregorian feed the focal length is very short; this in turn makes it very difficult to introduce complex optical paths for simultaneous frequency systems such as used on the KVN. Nevertheless,

technical solutions have been proposed; also we have carried out simulation studies to investigate the performance costs of using fast frequency switching in comparison to simultaneous observations at multiple frequency bands. The outcome is described in detail in Sect. 7.1.3.

Some of the high-frequency considerations for ngVLA are being tested on the KVN, which is the first dedicated full-time mm-wavelength VLBI (mm-VLBI) array and was commissioned in 2009. In this respect, we consider the KVN as a pathfinder for ngVLA. Currently KVN consists of three 21-m diameter antennas across South Korea, hosted at the campus of the Universities of Yonsei, Ulsan and Tamna (Lee et al. 2014), with a maximum baseline length of ∼500 km. Each antenna is equipped with an innovative quasi optical design of mirrors and low pass frequency filters that enables simultaneous observations at four frequencies: 22, 43, 86 and 130 GHz (Han et al. 2013). This design is a technological solution for effective tropospheric calibration and enables astrometry at frequencies three times higher than that achievable previously, using measurements at a lower frequency band. A detailed description of the method is presented in Sect. 5.2.

4.3 mm and sub-mm radio astrometry in the EHT era

The latest of the new global radio astronomy facilities to be opened is the Atacama Large Millimeter/submillimeter Array (ALMA).[2] This consists of extremely high precision antennas, with 54 having diameters of 12 m and another 12 of 7 m, in the Atacama desert (Chile), at about 5000 m above sea-level. The frequency coverage is from 84 up to 950 GHz, with plans for frequencies as low as 35 GHz. The antennas can be phased up to provide the equivalent sensitivity to that of a 85-m diameter single dish, from which the tied-array voltage signal can be recorded for VLBI observation. The ultra-sensitive phased-up ALMA is providing the corner-stone for VLBI at the highest frequencies ever performed, at hundreds of GHz. At these frequencies, where the atmospheric coherence times are extremely short, ALMA has allowed for a huge leap in performance for the Event Horizon Telescope (EHT) (Doeleman et al. 2009). The chief design goal of the EHT is the imaging of the shadow of a black hole, for which both frequencies above 200GHz and spatial resolutions greater than 40μas are required. The former is to overcome the intrinsic scattering around these sources and the latter is to provide the resolution to separate the black hole shadow from the bright disk of in-falling matter (Event Horizon Telescope Collaboration 2019). So far EHT has exclusively focused on making self-calibrated images, but when the small number of sufficiently strong sources are fully explored there will be a demand for more sensitive observations. Greater sensitivity can be achieved by longer coherent observations, such as provided by PR-type techniques regularly used at lower frequencies.

A conventional PR experiment at hundreds of GHz is probably impossible, as the atmospheric coherence times at these wavelengths are extremely short.

[2] https://www.almaobservatory.org

Nevertheless an alternative innovative method has been demonstrated up to 130GHz, the highest frequency with KVN, and we foresee no issues in application to higher frequencies, such as those relevant to EHT; ALMA has used a similar technique ("band-to-band") on their internal baselines (Asaki et al. 2020). The approach of SFPR is discussed in Sect. 5.2. Early discussion about next-generation EHT (ngEHT) is considering such a plan.

4.4 Space missions: astrometry from above the atmosphere and extraterrestrial baselines

Millimetron is a cm to sub-mm Russian space mission which envisages a radio telescope located at the L2 Lagrangian point (and later moving to a highly elliptical orbit), observing at frequency ranges from 15 GHz to 15THz (Smirnov et al. 2018). The space platform would host a single dish of 10m diameter, and will alternate operations between single dish and VLBI observations (at frequencies between 30 and 690 GHz), jointly with ground telescopes including the EHT antennas. The long baselines to the satellite telescope will provide a huge leap in the achieved angular resolution of the images and potentially astrometry, compared to ground arrays. Calibration of this instrument for VLBI will be a huge challenge, and therefore the capability to observe at multiple frequencies simultaneously is part of the design; this is also relevant to enable astrometry. For terrestrial VLBI the antenna positions are usually known to better than a cm, but this is not the case for the orbit error in Space-VLBI and this becomes the dominant source of astrometric error. VSOP had orbit errors of about 5 m (Porcas and Rioja 2000) and those for RadioAstron were significantly worse. It has been very hard to meet the requirements for astrometry with the satellite antennas (Tsuboi 2009) (with the exception of two particular cases: Porcas and Rioja 2000; Guirado et al. 2001) thus new approaches for astrometry are required. Details on the benefits of multi-frequency observations for astrometric calibration of mm-VLBI using SFPR, such as the removal of orbit errors, are described in Sect. 5.2 and in Rioja et al. (2011a).

Another high-frequency VLBI mission not bound to Earth is the proposed Japanese balloon-VLBI mission (Doi et al. 2019), in which the telescope is mounted on a balloon-borne platform. Here the purpose is to observe from the stratosphere, avoiding the tropospheric contributions. The baselines are not significantly longer than those of the global Earth-bound stations, and will have significant positional uncertainties. Nevertheless, if such a system was fitted with a multi-frequency receiver it would be suitable for astrometric observations, in the same manner as Millimetron.

Cosmic Microscope is a low frequency dual element space-VLBI concept by the Shanghai Astronomical Observatory of the Chinese Academy of Sciences, for state-of-the-art high resolutions studies at low frequencies. The Chinese space-VLBI mission is still in an exploratory phase, but has ambitious goals including astrometric capabilities. This Cosmic Microscope mission consists of two space-based 30m radio-telescopes in highly elliptical orbits with apogee

heights of 90,000 and 60,000 km respectively, with operational frequency bands at 30, 74, 330 and 1,670 MHz (An et al. 2019). The modes of operation will comprise: space-ground VLBI with the most sensitive ground infrastructure, such as the SKA, FAST and Arecibo telescopes, resulting in a powerful combination of high sensitivity and extremely long baselines for astrometric studies; space-space single baseline VLBI, resulting in observations free of atmospheric propagation medium effects (but not from orbit positional errors); and single dish mode, to monitor the sky for transient events that will be followed up with VLBI. The astrometric measurements will be carried out using the recently developed MultiView (Rioja et al. 2017) technique, with multiple in-beam calibrators (Sect. 5.1); this technique has important benefits for space-VLBI since, by correcting for the orbit errors (Dodson et al. 2013) as well as atmospheric contributions, it enables astrometry.

4.5 The VLBI Global Observing System for Geodesy and Astrometry

Accurate geodetic data is vital for astrometry, through the better modelling of source coordinates with the International Celestial Reference Frame (ICRF), the Earth Orientation Parameter (EOP) and telescope coordinates with the International Terrestrial Reference Frame, so astrometry and geodesy improve hand in hand. The next-generation instrument for geodesy was proposed by the International VLBI Service for Geodesy and Astrometry and is known as the VLBI Global Observing System (VGOS). VGOS is designed to deliver an order of magnitude improvement in the precision of the delay observable, which propagates into a similar improvement in the geodetic outcomes, amongst these the quality of the ICRF. This comprises a dedicated VLBI network, rather than a single station for VLBI. In the last decade it has steadily worked forwards from proposal to delivery, and now the concept and important demonstrations are established. To provide an order of magnitude improvement the requirements are: observations of many sources with-in the coherence time; rapid sky coverage to separate systematic terms; and sufficient sensitivity to be able to detect sources with flux densities greater than 250 mJy, in that time. Thus the system is based around fast slewing ($\sim 10^\circ$/sec), 12-m class antennas (System Equivalent Flux Density (SEFD) of $\sim$2,500Jy), capable of recording broad bandwidths from a 2–14 GHz continuous frequency band, and data processing technology at a high data rate of up to 16 Gbps (SNR of 20 in 10 sec). A number of new telescopes conforming to the VGOS specifications have been built or are planned globally. These, with improvements in analysis procedures and the optimisation of scheduling, should provide residual pathlength errors of the order of 1 mm, or a delay precision of four pico-seconds.

The unambiguous ‘group delay’, or delay across the observed bandwidth, has traditionally been the prime observable for geodesy and absolute astrometry since the 1970’s (see discussions and references in Counselman 1976). For VGOS these will come from observations of four 1-GHz bands spread across the frequency coverage. The demonstrations have shown that the group de-

lay uncertainties, with the improved sampling and bandwidth, are an order of magnitude less than those of the previous products and that the system calibration and stability is sufficient to meet the requirements (Niell et al. 2018).

4.6 Cross-over between radio and optical astrometry in the GAIA era

In the era of GAIA some aspects of radio astrometry will change considerably, therefore we quickly review GAIA and its impacts. The ESO satellite mission GAIA was launched in 2013, and is surveying the visible sky from the Earth-Sun Lagrangian point. It is expected to produce a catalogue of parallax and proper motions for one billion stars and AGNs with magnitudes brighter than 20. The final goal for astrometric precision is 7μas for $\sim 10^{\text{th}}$ magnitude stars, 20μas at 15^{th} magnitude, and 200μas at 20^{th} magnitude (Lindegren et al. 2018). Additionally, GAIA performs photometry and radial-velocity measurements on the brighter targets. The observations are relative between two telescopes pointing 106.5° apart. All objects should be observed about seventy times in the lifetime of the mission, which is currently about half way through. The point spread function is about 300mas, and the astrometric position is derived from a precise fit to the optical centroid.

The billion optical sources that GAIA (Gaia Collaboration et al. 2018a) will survey will include approximately 550,000 quasars (Gaia Collaboration et al. 2018b), which is better than 10 sources per sq. deg., so will be able to form a high precision optical inertial reference frame that can be compared to the radio-based ICRF. Given the large number of sources that GAIA will measure, the derived reference frame will be of an extremely high quality. One of the greatest weaknesses in the ICRF is that it is based on a small number of targets, particularly in the Southern Hemisphere (Titov 2007). The GAIA observations will resolve this issue providing a link between the Radio-measured Reference Frame and that of GAIA based on quasar positions. Lindegren (2020) discusses the important distinction between the 'faint' GAIA reference frame, which would include the AGN's that form the reference frame and the 'bright' reference frame, made up on the whole with stars from the Galactic population. There are instrumental difficulties directly connecting these two frames, and relative VLBI-astrometry of radio stars in the latter, referenced to the ICRF, will provide a crucial direct link between the two GAIA data products. Additionally, given the limited life time of any space mission, the long term radio-derived ICRF provides a vital cross-reference. The ICRF is based on observations from the 1980's onwards, albeit with continuous improvements, and thus is robust against long term systematic drifts such as the rotation of the frame. Currently, on going improvements of the VLBI geodetic and astrometric observations within VGOS are expected to result in an order of magnitude improvement, as discussed in Sect. 4.5.

The GAIA Data Release 2 included mapping of the Galactic plane stellar kinematics (Gaia Collaboration et al. 2018c) with 3.5 million measurements

of proper motion and parallax of stars down to 12^{th} magnitude from the local Galactic quadrant. I.e., 5 to 13kpc from the Galactic Centre, out to ±2kpc above and below the plane (see Fig. 9 Gaia Collaboration et al. 2018c). This allows for a phenomenally rich and detailed reconstruction of the Galactic dynamics and history of the optical stellar population. However, the global parameters for the disk rotation were still taken from Reid et al. (2014), underlining the importance of independent radio astrometric observations. Hitherto the research areas of geodesy and astrometry have been dominated by radio VLBI. Clearly the role of the radio investigations will need to adapt to the new landscape forged by GAIA, but given the respective strengths and weaknesses their complementary nature will only benefit both.

5 Next-generation astrometric calibration methods

There have been a number of new methods developed over the last decade that have had a significant impact on the field of precise astrometry, as they have provided a breakthrough in its application across the radio spectrum compared to previous methods. They are coming to fruition now with wide spread usage, being applied to KSPs of existing instruments, and driving the planning of the next-generation instruments.

In the low frequency regime, MultiView effectively reduces the impact of the large residual direction-dependent ionospheric effects between the target and the reference sources, and has a wide applicability. Section 5.1 describes the basis for MultiView and the astrometric outcomes.

In the high frequency regime, new approaches such as Source Frequency Phase Referencing (SFPR), and variations of it, breakthrough the upper frequency threshold imposed by the very fast tropospheric fluctuations and enables astrometry at much higher frequencies. Section 5.2 describes the basis for SFPR and the astrometric outcomes.

In both cases they open the prospects for precise astrometry at all frequency regimes, including with space-VLBI.

5.1 MultiView astrometric method

The MultiView calibration method (Rioja et al. 2017) offers the potential to achieve 'universal' high precision astrometry, including in the low frequency regime dominated by ionospheric disturbances, where other PR methods result in large errors. These arise from the spatial structure in the distribution of electrons in the ionosphere above each antenna, which introduce direction-dependent phase changes resulting in quasi-stationary spatial phase gradients; errors with similar signatures arise from residual tropospheric and geometric errors, albeit with smaller impact at the lower frequencies.

The strength of the MultiView method is in that it uses an appropriate combination of the observations towards multiple reference calibrator sources,

at least three, surrounding the target, to measure those phase gradients and its temporal variation, and thus calibrate the target observations accurately. See Table 1 for an indicative observing schedule. All sources are observed at the same frequency. MultiView calibration is ideally carried out in the visibility domain and uses 2D linear interpolations of the residual phases sampled along the calibrator directions. Effectively, this is equivalent to PR with a source pair whose relative separation is $\Delta\theta_{AB} \sim 0$ and therefore minimises the calibration errors. Instead, the MultiView calibration errors arise from the deviations of the ionospheric disturbances from a planar fit, in its most basic implementation with three calibrators.

Our demonstration of MultiView astrometry using VLBA observations at L-band (Rioja et al. 2017) using three calibrators with angular separations between 2 and 6 degrees away from the target, reached the thermal noise error regime of $\sim 100\mu$as. For comparison, this accuracy is equivalent to that achieved with in-beam PR observations with a calibrator separated by $10'$. The MultiView (MV) strategy results in excellent error compensation, even using distant calibrator sources that therefore place less stringent constraints for the angular separation and thus increases the applicability.

Following Eq. (2) for the differential phase observables, with $\nu_R = \nu_T = \nu$, a MV-calibrated dataset is formed with a linear combination of observations of N calibrators (C_i) that surround the target source (A):

$$\begin{aligned} \phi_T - \mathcal{R} * \phi_R &= \phi_A(t_o, \nu) - \sum_{i=1}^{N} \alpha_i * \phi_{C_i}(t_i, \nu) \\ &= (\phi_{\mathrm{A,pos}} - \phi_{\mathrm{C_v,pos}}) \pm \sigma\phi^{MV} \pm \sigma\phi_{\mathrm{thermal}} + 2\pi(n_A - \Sigma_i \alpha_i n_i), \\ &\quad \text{with } \alpha_{\mathrm{i}} \text{ real} \end{aligned} \tag{4}$$

where α_i are the weights used for the 2D linear spatial interpolation of the residual calibrator phases $\phi_{C_i}(t_i, \nu) + 2\pi n_i$ from the scans on the N calibrators to the direction and scan time of observations of the target source A. α_i are real and their values depend on the distribution of the sources in the sky. The values for α_i used in Dodson et al. (2017b), for example, are simply the linear fractional weights between the on-sky source positions; more complicated functions could be fitted, but are unlikely to be significantly better except where angular separations or the phase surface curvature are extremely large. The sum of α_i will be one if the calibrators surround the target, so the errors are not inflated. Beyond the preference for the target to lie within the locations of the calibrators on the sky, which ensures the corrections are interpolated rather than extrapolated, there are no particular limitations on their arrangement, other than to note that degenerate configurations (e.g., all in a line) will not allow accurate estimates for the phases as a function of the orthogonal direction. If all sources are observed simultaneously (dubbed in-beam MultiView) only the spatial interpolation is required. MultiView uses the FT-inversion approach to resolve the ambiguity issue, hence it is important to "phase connect"

the sequence of N calibrator phases prior to the interpolation, whilst there is no such requirement for the target.

The MV-calibrated target dataset is Fourier inverted and deconvolved to yield a synthesis image of the target source, which conveys a measure of its position relative to a virtual point in the sky (i.e., not the position of a particular object) determined by the ensemble of calibrators; this is indicated by the term $(\phi_{\mathrm{A,pos}} - \phi_{\mathrm{C_v,pos}})$ in Eq. (4). We note that, for comparison, the measured target positions using PR methods are tied to the assumed position of the corresponding (single) calibrator. Nevertheless, as long as the calibrator sources provide good fiducial points (i.e., are stationary), this virtual point is also stationary and any changes between the astrometric measurements in multi-epoch observations trace the motion of the target in both MultiView and PR. $\sigma\phi^{MV}$ are the phase calibration errors using MultiView and are quantified below, with all other terms as before. As mentioned above, special considerations are required to avoid inherent phase ambiguity issues in the multi-calibrator phase fitting strategy. MultiView, as implemented in Rioja et al. (2017), includes an automatic ambiguity check mechanism, based on the approach used in UVPAP (Jimenez-Monferrer et al. 2010), to avoid these issues. Those are expected to be increasingly relevant at lower frequencies (<5 GHz) or in cases when the calibrator source positions are poorly known. In the demonstration paper of MultiView (Rioja et al. 2017), at 1.7 GHz, we found that, typically, a few antennas over the VLBA array had one turn of phase to be corrected for, which is consistent with 6TECU residuals.

$\sigma\phi^{MV}$ is given by a linear combination of the calibration errors for the N target-calibrator pairs $(\sigma_i\phi)$, each following Eq. (3); i.e., $\sigma\phi^{MV} = \sum_{i=1}^{N} \alpha_i * \sigma_i\phi$, using $T_{\mathrm{swt,tro}} = T_{\mathrm{swt,ion}} = T_{\mathrm{swt}}$, where T_{swt} is the duty cycle of the observations, and $\Delta\theta_{\mathrm{tro}} = \Delta\theta_{\mathrm{ion}} = \sum_{i=1}^{N} \alpha_i \hat{s}_i - \hat{s}_{\mathrm{true}} \sim 0$, for the propagation effects. The latter applies under the assumption of the phase errors above a telescope having a planar spatial structure, in this case the static residual errors are fully compensated both for tropospheric and ionospheric components, including the case of low elevation observations that result in significant PR errors. This assumption is supported by empirical measurements of the small contribution from fine scale structure or "roughness" of the atmospheric disturbances after the subtraction of the low-order fit; these studies are discussed in Sect. 7.2.4. In the case of simultaneous observations of the target and calibrator sources, so called in-beam MultiView dynamical terms are largely cancelled as well. Thus we find the predicted phase errors for MultiView, using the terms from Eq. (3), to be:

$$\sigma\phi^{MV}_{\mathrm{sta,tro}} = \Sigma\alpha_i\sigma_i\phi_{\mathrm{sta,tro}} \approx 0$$

$$\sigma\phi^{MV}_{\mathrm{sta,ion}} = \Sigma\alpha_i\sigma_i\phi_{\mathrm{sta,ion}} \approx 0$$

$$\sigma\phi^{MV}_{\mathrm{dyn,tro}} = \Sigma\alpha_i\sigma_i\phi_{\mathrm{dyn,tro}} \approx 0$$

$$\sigma\phi^{MV}_{\mathrm{dyn,ion}} = \Sigma\alpha_i\sigma_i\phi_{\mathrm{dyn,ion}} \approx 0$$

Moreover MultiView also calibrates the residual geometric errors, such as antenna coordinate errors, which result in spatial phase gradients above the antennas as well, that is: $\sigma\phi^{MV}_{\rm geo} \sim 0$. This would include 'tip-tilt' errors in the alignment of a multi-beam feed such as that on FAST. Therefore, MultiView provides a very effective mitigation of the dominant sources of calibration errors that remain with other methods, arising from propagation medium effects and geometry errors, leading to astrometry accuracies in the thermal noise regime across the spectrum.

Table 2 lists the estimated systematic astrometric errors $\sigma\Delta\theta^{MV}$ (Col. 3), from the propagation of MultiView residual atmospheric errors, taking into account the empirical studies (Sect. 7.2.4), at a range of frequencies. For comparison, these are about one order of magnitude smaller than those for in-beam PR with a calibrator $10'$ away ($\rm PR_{10'}$) (see Sect. 9 and Fig. 2, for the direct comparison between the outcomes of both methods). As a result, MultiView astrometric accuracy easily reaches the thermal limit with current instruments, which corresponds to $\sim 100\mu$as at 1.6 GHz, with DR of 100:1; that is $\sigma\Delta\theta^{MV} \ll \sigma\Delta\theta_{\rm thermal}$. In comparison in-beam $\rm PR_{10'}$ results in a similar astrometric performance, but where $\sigma\Delta\theta^{PR_{10'}} \sim \sigma\Delta\theta_{\rm thermal}$. MultiView systematic calibration errors are comparable to the thermal noise levels from the next-generation instruments (i.e., DR of 1000:1), for example 6μas at 1.6 GHz (Table 2 Col. 3). The prospect is for MultiView to achieve ultra-precise μas-level astrometry at frequencies where today's measurements are carried out, with SKA and ngVLA, and enable precise astrometry at the much lower frequencies with SKA. Ultra precise astrometry is one of the most innovative outcomes of VLBI with the next-generation instruments and some example projects are presented in Sect. 9.

Recently suitable technologies for forming simultaneous multiple beams have been developed. We discuss multiple tied-array beams for antenna arrays in Sect. 7.2.1 and multiple beams for large telescopes in Sect. 7.2 and their implementation on the next-generation instruments in Sect. 4. Observations of at least three calibrators surrounding the target is the minimum requirement, which requires $\geq$4 tied-array beams. With more than the minimum number of calibrators one could over-fit the plane (or fit higher order surfaces) to reduce the measurement errors. However, the main advantage, in general, would be in the identification and removal of unsTable reference points (Sect. 2.2). It is such systematic errors that we believe will become a new dominant source of errors and determine the ultimate astrometric limit with the next-generation instruments.

MultiView is also relevant for enabling highest precision astrometry from the extra-terrestrial baselines with space-VLBI, where the large orbit errors have traditionally prevented astrometry using PR methods (see Sect. 4.4). Instead, MultiView results in an effective calibration of geometric errors, such as the position errors of the orbiting antenna, along with the propagation medium effects. Dodson et al. (2013) carried out MultiView simulation studies with realistic atmospheres and orbit errors, to demonstrate the feasibility of

MultiView for Space-VLBI astrometry and found $3\pm1\mu$as systematic errors in the best cases, at 1.6 GHz.

Other related implementations are the recent Reid et al. (2017) demonstration of MultiView spatial interpolation in the image domain. Earlier approaches were: 'Cluster-Cluster' VLBI, proposed in the 1990's (Rioja et al. 1997b, 2002), similar slewing strategies (Fomalont and Kopeikin 2002; Fomalont and Kogan 2005), and the bi-gradient method (Doi et al. 2006). None of the latter have had great usage, perhaps because they lacked methods for correcting for ambiguities. Future implementations of MSSC plan to fit higher order functions to the multiple calibrators used in that method (Sect. 3.2.1), which would be similar.

5.2 Source/Frequency Phase Referencing astrometric method

The Source Frequency Phase Referencing (SFPR) calibration method (Rioja and Dodson 2011) provides a breakthrough for mm-VLBI astrometry beyond the scope of PR methods. SFPR achieves an effective calibration of the residual fast tropospheric error fluctuations and the geometric errors, both with a non-dispersive nature, along with the dispersive ionospheric errors. SFPR is widely applicable with no upper frequency limit, if the instrument has the required capability.

The fast tropospheric fluctuations limit the coherence time and are the main challenge in VLBI observations at high frequencies, which combined with intrinsically lower source fluxes and higher instrumental noise limits the observations to stronger sources. Astrometry has even more stringent considerations than imaging, therefore PR astrometric measurements have traditionally been limited to frequencies up to 43 GHz.

Multi-frequency calibration is an approach that has only recently begun to deliver on its promise for mm-VLBI, based on the longstanding recognition of the non-dispersive nature of the tropospheric propagation effects. Strategies involving dual frequency observations, where the high frequency (i.e., target frequency $\nu^{\rm high}$) observations are calibrated using the scaled solutions from a lower (i.e., reference frequency $\nu^{\rm low}$) and more amenable frequency have been proposed in the past (Asaki et al. 1996; Carilli and Holdaway 1999; Middelberg et al. 2005). We refer to these as "frequency phase transfer" strategies (FPT). But it was not until the development of calibration methods that precisely accounted for all, non-dispersive and dispersive, error contributions that successful mm-VLBI high precision astrometry was achieved.

In SFPR the small and slow changing differential residual ionospheric dispersive error contributions, are mitigated with interleaving multi-frequency observations of the target (A) and a second source (B, reference source or calibrator); here, the angular separation between the two sources ($\Delta\theta_{AB}$) can be up to many degrees and the duty cycle ($T_{\rm swt}$) up to many minutes. This is unlike the case for PR methods which require fast switching to match the fast tropospheric fluctuations. We note that the SFPR mitigation applies to other

dispersive contributions as well, such as instrumental terms. See Table 1 for an indicative observing schedule.

A detailed description of the basis of SFPR and the first demonstration of the astrometric capability was presented in Rioja and Dodson (2011), using fast frequency switching VLBA observations at 43/86 GHz, of a pair of sources 10° apart. Superior performance comes from the technical solution adopted by the KVN, where the multi-frequency receivers (Han et al. 2008, 2013) enable simultaneous observations at four frequency bands (22, 43, 86, 130 GHz). This results in much improved error mitigation and therefore allows application to much higher frequencies. Rioja et al. (2015) describes a SFPR demonstration at the highest KVN band, at 130 GHz (see Fig. 4).

Following Eq. (2) for the differential phase observables, with $\nu_R = \nu^{\rm low}$, $\nu_T = \nu^{\rm high}$ and $R = \frac{\nu^{\rm high}}{\nu^{\rm low}}$, a SFPR-calibrated target dataset is formed with a linear combination of observations at the reference and the target frequencies ($\nu^{\rm low}$ and $\nu^{\rm high}$, respectively), and of the target and reference (or calibrator) sources (A and B, respectively) as:

$$\begin{aligned}\phi_T - \mathcal{R} * \phi_R &= \left(\phi_A(t,\nu^{\rm high}) - \mathcal{R} * \phi_A(t,\nu^{\rm low})\right) \\ &\quad - \left(\phi_B(t',\nu^{\rm high}) - \mathcal{R} * \phi_B\left(t',\nu^{\rm low}\right)\right) \\ &= \left(\phi^{\rm high}_{A_{\rm pos}} - \mathcal{R} * \phi^{\rm low}_{A_{\rm pos}}\right) - \left(\phi^{\rm high}_{B_{\rm pos}} - \mathcal{R} * \phi^{\rm low}_{B_{\rm pos}}\right) \pm \sigma\phi^{\rm SFPR} \\ &\quad \pm \sigma\phi_{\rm thermal} + 2\pi\left(\mathcal{R}n^{\rm low} - n^{\rm high}\right)\end{aligned} \tag{5}$$

where the superscripts 'high' and 'low' are for observations at $\nu^{\rm high}$ and $\nu^{\rm low}$, respectively. $\sigma\phi^{\rm SFPR}$ stands for the SFPR calibration errors, and all other terms as for those in Eq. (2). The SFPR-calibrated dataset is Fourier inverted and deconvolved to yield a synthesis image of the target source at the target frequency ($\nu^{\rm high}$); the SFPR-map. The position offset of the target source relative to the SFPR-map center is a bona-fide astrometric measure of the combined spectral position-shifts (i.e., $\delta\theta^{\rm high-low}$) for sources A and B, between the observed frequencies (e.g., core-shifts in AGNs, emission from different molecular species or transitions, etc). This astrometric outcome is retained in the terms $(\phi^{\rm high}_{A_{\rm pos}} - \mathcal{R} * \phi^{\rm low}_{A_{\rm pos}})$ and $(\phi^{\rm high}_{B_{\rm pos}} - \mathcal{R} * \phi^{\rm low}_{B_{\rm pos}})$ in Eq. (5). In general, using multiple combinations of source pairs, it is possible to disentangle the individual contribution from each source as for PR measurements; for an example see the solution for the five sources scheduled in the observations for Rioja et al. (2015).

Simultaneous multi-frequency observations greatly facilitate the phase connection, as the typical phase rate ($\simeq 10^{-13}$s/s) at these high frequencies ($\sim$100 GHz) requires the frequency switching duty cycle to be significantly less than a minute. If $\mathcal{R}$ is an integer, then $\mathcal{R}n$ is also an integer and the 2π phase ambiguity issue is implicitly dealt with in the Fourier mapping approach. For this reason it is highly recommendable to select integer frequency ratios. The special considerations for observations with non integer $\mathcal{R}$ values (particularly

for unrelated maser species) are described in Dodson et al. (2014). In essence, this requires ensuring good a-priori model values (so that $n^{\rm low}$ is zero).

The direct outcomes of SFPR are: i) inter-band astrometry (or λ-astrometry), for precise registration of images at different bands, ii) increased sensitivity, from the extension of the coherence times, which can be extended up to several hours at 130 GHz (Rioja et al. 2015), and, moreover iii) astrometry of the target source at $\nu^{\rm high}$ with respect to an external reference source in the sky, by also including PR observations between the pair of sources A and B at $\nu^{\rm low}$ (as for the example in Dodson et al. 2014).

The propagation of errors for SFPR is discussed in detail in Rioja and Dodson (2011). Briefly, the magnitude of $\sigma\phi^{\rm SFPR}$, at the target frequency $\nu^{\rm high}$, can be estimated using the Eq. (3), taking into account: i) the scaling by $\mathcal{R}$ and $\mathcal{R}$-1/$\mathcal{R}$ of the tropospheric and ionospheric terms at $\nu^{\rm low}$, respectively, along with ii) $\Delta\theta_{\rm tro} = \delta\theta^{\rm high-low} \sim 0$ and $T_{\rm swt,trp} = 0$, iii) $\Delta\theta_{\rm ion} = \Delta\theta_{AB}$, $T_{\rm swt,ion} = T_{\rm swt}$. That is:

$$\sigma\phi^{\rm SFPR}_{\rm sta,tro}(\nu^{\rm high}) = \mathcal{R}\ \sigma\phi_{\rm sta,tro}(\nu^{\rm low}) = 0$$

$$\sigma\phi^{\rm SFPR}_{\rm sta,ion}(\nu^{\rm high}) = (\mathcal{R} - 1/\mathcal{R})\ \sigma\phi_{\rm sta,ion}(\nu^{\rm low}) = O(\Delta\theta_{AB}, \mathcal{R}),$$

$$\sigma\phi^{\rm SFPR}_{\rm dyn,tro}(\nu^{\rm high}) = \mathcal{R}\ \sigma\phi_{\rm dyn,tro}(\nu^{\rm low}) \approx 0$$

$$\sigma\phi^{\rm SFPR}_{\rm dyn,ion}(\nu^{\rm high}) = (\mathcal{R} - 1/\mathcal{R})\ \sigma\phi_{\rm dyn,ion}(\nu^{\rm low}) = O(\Delta\theta_{AB}, T_{\rm swt}, \mathcal{R})$$

The residual ionospheric terms in $O()$ represent small contributions. Moreover, SFPR also calibrates the residual geometric errors, being non-dispersive, and $\sigma\phi^{\rm SFPR}_{\rm geo} \sim 0$; this is particularly relevant for space-VLBI, as discussed above. Note that both components of the residual tropospheric errors are completely calibrated, $\sigma\phi^{\rm SFPR}_{\rm tro} \approx 0$, thanks to the same-line-of-sight calibration and simultaneous observations at the two frequencies; the same applies to the contributions arising from residual geometric errors (i.e., errors in reference source and antenna position coordinates), and in general any other non-dispersive residual contributions. Therefore, $\sigma\phi^{\rm SFPR}_{\rm sta,ion}$ is likely to be the dominant source of errors, particularly in cases where the angular separation between the two sources is several degrees and R is large. Its magnitude can be minimised by using values for $\mathcal{R}$ and $\nu^{\rm low}$ as low and as high as possible, respectively. For example, the value for $\sigma\phi^{\rm SFPR}_{\rm sta,ion}$ at $\nu^{\rm high} = 132$ GHz with $\nu^{\rm low} = 22$ GHz, where the scale ratio $\mathcal{R} - 1/\mathcal{R}$ is 5.8 and the residual excess ionospheric path length at 22 GHz is ∼0.5cm, is an order of magnitude larger than using $\nu^{\rm low} = 44$GHz, for which $\mathcal{R} - 1/\mathcal{R}$=2.7 and the residual path length is ∼0.1cm. In this case the systematic limits to the SFPR astrometric accuracy $\sigma\Delta\theta^{\rm SFPR}$ at 88 GHz would be 0.9μas/deg and at 132 GHz it would be 1.6μas/deg, using $\nu^{\rm low} = 44$ GHz and nominal parameters for the atmosphere; the corresponding thermal astrometric limits $\sigma\Delta\theta_{\rm thermal}$ would be 1.2 and 0.8μas, at 88 and 132 GHz, respectively, for a DR 100:1.

With an increasing number of telescopes equipped with simultaneous multi-frequency capabilities the perspectives for mm-VLBI are most promising. The KVN is leading the effort towards exploring the advantages of this technological solution at the highest frequencies, together with the East Asian VLBI Network for longer baselines such as those to the VERA antennas (Zhao et al. 2019). In addition, in Europe, Yebes-40m (Spain) has a multi-frequency system installed and carries out regular observations with KVN and KaVA (Sohn et al. 2018); Medicina-32m, Noto-32m and SRT-64m telescopes in Italy are being equipped with compatible multi-frequency receivers, and several other telescopes are expected to be simultaneous multi-frequency ready in the near future, both in Europe and across the globe.

We expect that the current promising results will further improve with the ongoing developments and observations with the next-generation instruments. The specifications of ngVLA include the (near) simultaneous multi-frequency capability, and this is further discussed in Sect. 7.1.3. SFPR is also relevant for high frequency space-VLBI missions, such as Millimetron, a regime where astrometry is challenging (see Sect. 4.4). The large a-priori orbit errors of the satellite antenna(s) are an unsurmountable issue for PR methods; instead these are readily compensated for, with the dual frequency calibration.

5.3 Multi-Frequency Phase Referencing astrometric method

Multi-Frequency Phase Referencing (MFPR) is a multi-frequency technique that builds on SFPR and is equally of relevance for high precision astrometric measurements in the highest frequency regime. It also relies on near simultaneous multi-frequency observations for tropospheric calibration, but unlike SFPR it does not require a second source to remove the remaining dispersive residual terms. It is unique in enabling precise phase astrometry with observations of only the target source. Instead MFPR explicitly measures the dispersive terms on the target source itself, with dedicated blocks of observations at multiple bands spanning a wide frequency range between 1.3 and 22 GHz (ν_i, ν_j and ν_k in the observing schedule in Table 1). The basis of the method and the first demonstration are described in detail in Dodson et al. (2017b), along with special considerations for instrumental calibration and other effects during the analysis. These ionospheric calibration blocks (ICE-blocks) are interleaved with the program multi-frequency (near) simultaneous observations in the highest frequency regime, and do not require the same simultaneous, or near-simultaneous, frequency coverage. Therefore standard frequency switching capabilities between the frequency scans in the ICE-blocks provides a sufficiently accurate measurement of the dispersive residual ionospheric contribution (i.e., $\Delta I \lesssim 0.1$ TECU) which is calibrated out from the program observations. The experiment measured a 21μas core-shift between 22 and 43-GHz for BL-Lac (for which no suitable high frequency calibrator could be found), which deviated from the expectation based on the Blandford and Königl standard model. An instrument with great frequency agility is required

to carry out MFPR observations and currently only the VLBA, with its fast frequency switching capability and wide frequency coverage, is suitable.

The MFPR-calibrated target dataset is formed with a linear combination of the phases from observations of the target source A at the reference and the target frequencies ($\nu_R = \nu^{\rm low}$ and $\nu_T = \nu^{\rm high}$, respectively) and $\mathcal{R} = \frac{\nu^{\rm high}}{\nu^{\rm low}}$, following Eq. (2):

$$\begin{aligned}\phi_T - \mathcal{R} * \phi_R &= \left(\phi_A(t,\nu^{\rm high}) - \mathcal{R} * \phi_A(t,\nu^{\rm low})\right) \\ &= \left(\phi^{\rm high}_{A,{\rm pos}} - \mathcal{R} * \phi^{\rm low}_{A,{\rm pos}}\right) \pm \sigma\phi^{\rm MFPR} \pm \sigma\phi_{\rm thermal} + 2\pi(\mathcal{R}n - n')\end{aligned} \tag{6}$$

where $\sigma\phi^{\rm MFPR}$ stands for the MFPR calibration errors and the other terms are as for Eq. (5). The same considerations as for SFPR apply if $\mathcal{R}$ is a non-integer ratio.

Following the same steps as for SFPR, the position offset of the target source relative to the MFPR-map center is a bona-fide astrometric measure of the "core-shift", or more generally the spectral position shift, in the target source between the two observed frequencies, $\delta\theta_A^{\rm high-low}$. The calibration errors are obtained following Eq. (3), with $\Delta I \sim 0$, $\Delta\theta_{\rm tro} = 0$, $\Delta\theta_{\rm ion} = 0$, $T_{\rm swt,trp} = 0$ and where $T_{\rm swt,ion}$ is the interval between the ICE-blocks. However, any core-shift in the prime calibrator would introduce a fixed phase offset between frequency bands. Care is needed to avoid or correct for this (see Dodson et al. 2017b, for an example). The propagation of errors for MFPR is discussed in detail in Dodson et al. (2017b), and is similar to that for SFPR. That is:

$$\sigma\phi^{\rm MFPR}_{\rm sta,tro}(\nu^{\rm high}) = \mathcal{R}\ \sigma\phi_{\rm sta,tro}(\nu^{\rm low}) = 0$$

$$\sigma\phi^{\rm MFPR}_{\rm sta,ion}(\nu^{\rm high}) = (\mathcal{R} - 1/\mathcal{R})\ \sigma\phi_{\rm sta,ion}(\nu^{\rm low}) = 0$$

$$\sigma\phi^{\rm MFPR}_{\rm dyn,tro}(\nu^{\rm high}) = \mathcal{R}\ \sigma\phi_{\rm dyn,tro}(\nu^{\rm low}) = 0$$

$$\sigma\phi^{\rm MFPR}_{\rm dyn,ion}(\nu^{\rm high}) = (\mathcal{R} - 1/\mathcal{R})\ \sigma\phi_{\rm dyn.ion}(\nu^{\rm low}) = O(T_{\rm swt,ion}, \mathcal{R})$$

In MFPR, like SFPR, both tropospheric residual contributions are perfectly compensated for ($\sigma\phi^{\rm MFPR}_{\rm tro} = 0$), as they are derived from simultaneous multi-frequency observations of the target source. Likewise, the ionospheric residual errors are solved for in the direction of the target, hence $\sigma\phi^{\rm MFPR}_{\rm sta,ion} = 0$. The residual dynamic ionospheric errors $\sigma\phi^{\rm MFPR}_{\rm dyn,ion}$, which are a function of $T_{\rm swt,ion}$ and $\mathcal{R}$, will be small as the multi-frequency ICE-blocks are closely interleaved with the program observations. Therefore the systematic astrometric precision for MFPR will easily be able to exceed that of the thermal limits from a DR of 1000:1, i.e. $\sigma\Delta\theta^{\rm MFPR} < \sigma\Delta\theta_{\rm thermal}$.

MFPR requires an instrument with great frequency agility, and enables precise $\lambda-$astrometry, between high-frequencies, using only observations of a single source. This is relevant because the availability of calibrator sources

is an increasingly significant issue at higher frequencies. We note that, however, the instrument stability is vital, as that can not be separated from the measurement of the ionospheric dispersive terms.

Wide band receivers that allow for simultaneous observations at multiple bands spanning a large frequency range are ideal for the ionospheric calibration using the ICE-blocks (e.g., the BRAND and VGOS technological developments, see Section 7.1.2). Simultaneous multi-band high frequency receivers are the optimum solution for the tropospheric calibration, as for SFPR. We believe that ngVLA could fulfil all of these requirements.

5.3.1 Beyond Frequency Phase Transfer: FPT-squared

FPT-squared is an alternative calibration method to MFPR that uses two pairs of simultaneous dual-frequency observations at mm-wavelengths, of the target source only. It builds on the Frequency Phase Transfer (FPT) method described above but applies the scaled-correction twice, to allow for the cancellation of ionospheric contributions, using the multiple frequency pairs from the KVN. Zhao et al. (2018) describe the basis of this approach and its suitability for high-frequency all-sky surveys including very weak sources, such as in iMOGABA (Sect. 8.3.3) providing coherence times up to several hours at 86 GHz. The demonstration using KVN observations at 22/43 GHz and 22/86 GHz confirmed the validity of the FPT-squared calibration across large angular separations and temporal gaps and confirmed the feasibility to calibrate sources distributed across the sky with a few calibrators. This method is, as with MFPR, very sensitive to the instrumental stability. Additionally the astrometrical signature, which is a mixture from both frequency pairs, can be complex to disentangle. On the other hand it provides an approach which does not require low frequency measurements such as ICE-blocks; therefore this is of interest for arrays which do not have that capability, such as the KVN. Given the rapid expansion of the SFPR network this technique may find useful astrometric applications.

6 Historical development and advances

In this section we review the historical progress on astrometric precision and the scope of application, since the foundational work. Here we are focusing on the developments that enabled the improvements in astrometric performance.

Figure 2 illustrates the comparative performance between astrometric techniques as a function of the observing frequency, assuming a baseline of 6,000 km. The grey dotted line is for the astrometric limits imposed by the thermal noise (or sensitivity) of the instrument, in the absence of systematic errors, assuming a DR of 100:1. The other lines show the single epoch systematic astrometric limits $\sigma\Delta\theta^{\rm cal}_{\rm sta}$, estimated for nominal values of $\Delta\ell_z$ and ΔI that model the dominant propagation medium effects, as presented in Sections 3 and 5, for

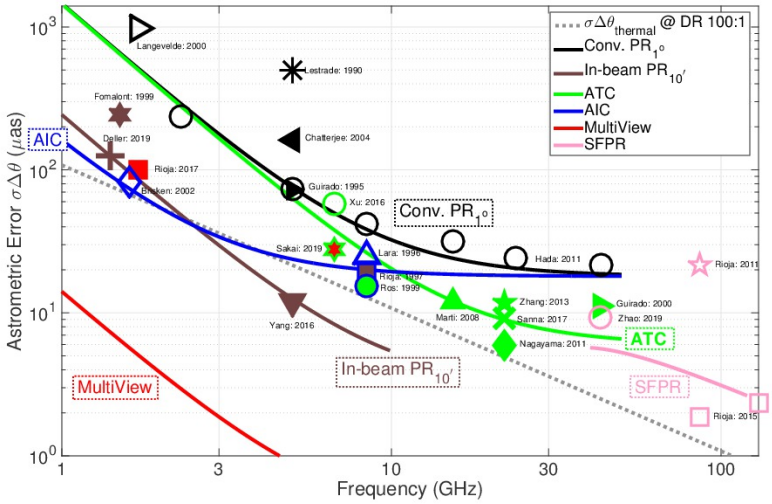

Fig. 2 Plotted with lines are the estimates of astrometric performance, over the range of frequencies with published results, arising from thermal noise with a DR of 100:1 (grey dotted line; $\sigma\Delta\theta_{\rm thermal}$) and systematic calibration errors $\sigma\Delta\theta^{\rm cal}$ from the techniques described in Sections 3 and 5, with a baseline of 6,000 km. For conventional PR with an angular separation of 1° (black solid line; $\sigma\Delta\theta^{\rm PR}_{1^\circ}$), typical atmospheric residuals are ΔI=6 TECU for the ionosphere and $\Delta\ell_z$=3 cm for the troposphere; these are the same for in-beam PR, except for the angular separation being 10′(brown solid line; $\sigma\Delta\theta^{\rm PR}_{10'}$). The former line extends up to 50 GHz and the later extends up to 10 GHz, to indicate the typical limits of those techniques. Also plotted are the expected performance for PR with Advanced Tropospheric Calibration (ATC), with the same parameters as PR except for $\Delta\ell_z$=1 cm (green solid line), and for PR with Advanced Ionospheric Calibration (AIC), with the same parameters as PR except for ΔI=0.6 TECU (blue solid line). For comparison the astrometric errors from MultiView (red solid line; $\sigma\Delta\theta^{\rm MV}$), with parameters from Sect. 7.2.4, are significantly smaller than the thermal limits and would extend up to 50 GHz. SFPR enables astrometry at the highest frequencies, beyond the thresholds of PR. The astrometric errors from SFPR, with a 5° angular separation (pink solid line; $\sigma\Delta\theta^{\rm SFPR}$), are shown between 40 and 130 GHz, using $\nu^{\rm low}$=22 GHz observed simultaneously. The final astrometric error is the combination of the thermal noise and the systematic contributions, for each technique. Over plotted with symbols are some empirical results for a single epoch from the literature. They illustrate that the theoretical formulae match the empirical trends, and also indicate the improvements over time to arrays and a-priori models. The results correspond to a range of different targets (pulsars, masers, AGNs), source flux densities, schedules, weather conditions, analysis pipelines and instruments; thus significant differences are to be expected. For a meaningful direct comparison they are normalised to correspond to 1° angular separation (except for in-beam PR, where there was no normalisation, and SFPR where they are normalised to 5°), single epoch accuracies and to approximately 6,000km baselines. The colours match the techniques as described above and the symbols reproduce the trend of the systematic limits, except where other limitations apply as discussed fully in Sect. 6.

the different methods. Between these two competing contributions, sensitivity versus calibration errors, whichever is the largest determines the expected measurement precision. Overplotted symbols correspond to observational results from the literature, to show how these conform to the expectations. To allow for comparison of the multitude of different observations and reported information the results are scaled to 1° angular separation between the target and calibrator for conventional PR and to 5° for SFPR; no scaling is applied for in-beam PR. VERA, KVN and KaVA observations are scaled to 6,000 km baselines. All are converted to the equivalent of a single epoch, i.e. parallax errors are scaled by the square root of the number of observations. This ignores significant effects from: source declination, weather conditions, error analysis, source flux density and scheduling strategy. These normalised values provide guidance to how astrometric methods have improved over time, and therefore how we may improve further, as required with the next-generation instruments (Sections 4 and 7).

6.1 Conventional PR

The solid black line in Fig. 2 corresponds to the theoretical expectations for astrometric errors in PR, arising from residual tropospheric and ionospheric errors characterised with $\Delta\ell_z$ = 3cm and ΔI = 6TECU, for a source pair separation of 1°. One can clearly appreciate how the astrometric errors are expected to rapidly degrade towards low frequencies. As PR is impracticable above 43-GHz, the line truncates at 50-GHz. Symbols in black are historical astrometric measurement errors selected from the literature to represent the performance of conventional PR methods across the spectrum, scaled to a common angular separation of 1°. Open circles are from the M87 observations by Hada et al. (2011), which mapped out the frequency dependent core-shift effect with exquisite accuracy. Matching precision was found by Guirado et al., (1995, black triangle-right) at 5 GHz, using phase-delay differential astrometric analysis, for a single pair of sources. This can be compared to the accuracy from only 5 years earlier for Lestrade et al. (1990, star). As GPS corrections were not available at that time ΔI could have been as high as 40. The early observations of OH-maser parallaxes at 1.6 GHz by van Langevelde et al. (2000, open triangle-right) were for many years the most accurate low frequency astrometric maser result, but also limited by the accuracy of the ionospheric model. Chatterjee et al. (2004, triangle-left) showed that better pulsar astrometry precision could be obtained with conventional PR by observing at (much) higher frequencies, 5 GHz in this case, even though the targets were much weaker. The sensitivity is not given for the latter observations, but we estimate that the DR would have been ∼30.

6.2 In-beam PR

The in-beam PR strategy to mitigate the astrometric challenges relies on using very nearby reference sources; its main application is at the low frequencies. The brown line in Fig. 2 gives the astrometric performance expected, for the same nominal conditions as in Sect. 6.1, but scaled to an angular separation of $10'$. The dilution factor is six times greater and therefore the errors are six times smaller, compared to the black solid line for conventional PR. It becomes harder to find in-beam calibrators for a target within the smaller antenna FoV at higher frequencies (see predictions in Table 2), therefore the usability of in-beam PR is reduced above L-band. Thus the line truncates at 10-GHz. The brown symbols in Fig. 2 are demonstrations of its effectiveness; the pulsar astrometry of Fomalont et al. (1999, star) at 1.5 GHz was the first demonstration using a close-but-weak reference source at $12'$. The pulsar astrometry from Deller et al. (2019, plus) at 1.4 GHz are for a target-calibrator angular separation of $10'$. The difference between these two represents the improvement in the systems (instrument, and a priori models) over the two decades separating them. Rioja (1993) and (Rioja et al. 1997a) observed the 1038+528 source pair at 8.4 GHz, which is the closest pair of strong sources, being separated by only $33''$ (it is worth noting that the latter analysis also included S/X AIC corrections, so it is marked as a brown square outlined in blue). Their analysis is dominated by the thermal noise, with a DR of ∼30. Yang et al. (2016, triangle-down) performed a very deep EVN observation of a Swift-detected tidal burst with an in-beam calibrator only $2'$ away and with a DR of up to 537 that had extremely high precision, leading to a very strict limit on the speed of the outflow.

6.3 Advanced Tropospheric Calibration

ATC methods to reduce the value of $\Delta\ell_z$ to ~ 1 cm are described in Sect. 3.3.1. Amongst these are GeoBlocks and simultaneous source-pair fitting, with phase reference imaging and differential phase delay astrometry, respectively. Its main impact is at the high frequencies regime, whilst at low frequencies the limitations would be the same as for conventional PR. The green line in Fig. 2 corresponds to the theoretical expectations for residual tropospheric and ionospheric errors characterised with $\Delta\ell_z$=1 cm and ΔI=6 TECU, respectively, for a target-calibrator angular separation equal to 1° and terminating at 50-GHz, as for conventional PR. Examples of published measurements are shown with symbols in green, scaled to 1°. Guirado et al. (2000) and Martí-Vidal et al. (2008) carried out at 43 (triangle-right) and 15 GHz (triangle-up) respectively and used UVPAP. A similar analysis in Ros et al. (1999, green filled circle with blue outline), at 8.4 GHz (X-band) using dual band S/X observations, where both advanced tropospheric and ionospheric corrections were made, lies slightly below the nominal ATC line. We include only two of the many BeSSeL results at 22 GHz that use GeoBlocks, Sanna et al. (2017, cross), which mea-

sured a record distance to a star-forming region on the far side of the Galaxy of $20.4^{-2.8}_{+2.2}$kpc and Zhang et al. (2013, star), which has the record parallax precision of $\pm 3\mu$as. Nagayama et al. (2011, diamond) reports the best VERA parallax, with a precision of $\pm 7\mu$as. This VERA result is scaled down by a factor of 3, to allow direct comparison with the VLBA results. The BeSSeL observations of Xu et al. (2016, open circle) at 6.7 GHz sits in the frequency regime where ATC corrections have little effect and it is appreciably above the other ATC results.

6.4 Advanced Ionospheric Calibration

AIC methods to reduce the value of ΔI are described in Sect. 3.3.2 and their main impact is at the low frequency regime, whilst the high frequency regimen remain as for conventional PR. The blue line in Fig. 2 corresponds to the theoretical expectations for systematic astrometric errors with residual tropospheric and ionospheric errors characterised with $\Delta\ell_z = 3$cm and $\Delta I = 0.6$TECU, respectively, for a target-calibrator angular separation equal to 1°. Note that the value of ΔI is reduced by a factor of ten, compared to conventional PR, achieving similar precision as in-beam PR. Examples of measurement errors per epoch from the literature are scaled to 1° and shown as blue symbols: Brisken et al. (2002, open diamond), for pulsar parallaxes measurements at 1.6 GHz with fits to the residual phases to reduce ΔI; and Lara et al. (1996, triangle), for AGN astrometry at 8.4 GHz, using dual frequency S/X observations where analysis of the delays provide 'ionosphere-free' data products.

6.5 MultiView

MultiView results in a superior compensation of both $\Delta\ell_z$ and ΔI by using multiple calibrators as described in Sect. 5.1. The red line in the bottom left corner of Fig. 2 corresponds to the theoretical expectations for systematic astrometric errors with residuals as described in Sect. 7.2.4 and listed in Table 2 (Col. 3). As both the tropospheric and ionospheric errors are near-perfectly compensated MultiView outperforms all other PR-related methods across the frequency spectrum. It is relevant across the radio spectrum, but particularly in the low frequency regime where the conventional errors are large. MultiView calibration is most naturally carried out in the visibility domain. The measurement of Rioja et al. (2017, square) in Fig. 2 is a MultiView demonstration on an AGN with calibrators up to several degrees from the target, where the final astrometric errors are dominated by the thermal errors that greatly exceed the systematic errors, which are negligible. Fig. 3 demonstrates the astrometric repeatability of these observations and compares them to PR. Sakai et al. (2019, red star with green outline) used an alternative implementation, in the image domain (Reid et al. 2017, so is only effective for the errors coherent

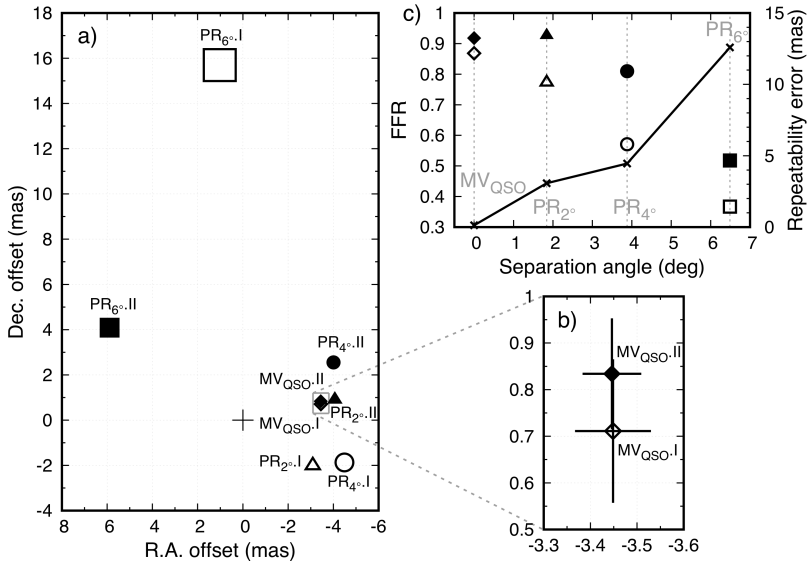

Fig. 3 *a)* Astrometric measurements with MultiView and PR at 2°, 4° and 6° (see Rioja et al. 2017, for description), from the observations of quasars at two epochs, with respect to the catalogue position. The size of the plotted symbols corresponds to the estimated thermal noise error in each case. The labels describe the calibration methods (MV, PR with the angular separation as a subscript) and epoch of observations (I, II). *b)* Zoom for MultiView astrometric solutions, which lie within 100μasof each other. The error bars are for the estimated thermal noise; both epochs agree to within thermal errors. *c)* Solid line shows the corresponding repeatability astrometric errors versus the angular separation between target and calibrator for PR analysis, and for an effective 0° separation for MultiView. Filled and empty symbols show the Flux Fractional Recovery (FFR) quantity versus angular separation for MultiView (diamond), PR_{2° (triangle), PR_{4° (circle), and PR_{6° (square), for epochs I (empty) and II (filled).

over the array during the observations), applied to BeSSeL measurements of Methanol masers at 6.7 GHz. Sakai et al. (2019b) used both MultiView in the image domain and ATC corrections and can be compared to Xu et al. (2016), which only had the latter, to demonstrate the impact.

6.6 Source Frequency Phase Referencing

SFPR results in a superior compensation of the fast tropospheric fluctuations in $\Delta\ell_z$ that sets the upper frequency threshold of any PR-method, and opens a new window for VLBI-astrometry. The pink line in Fig. 2, starting at 40 GHz and continuing to 130 GHz, is for the expected SFPR astrometric errors $\sigma\Delta\theta^{\rm SFPR}_{\rm sta}$ with a reference frequency ($\nu^{\rm low}$) of 22 GHz and a calibrator 5° away. See Sect. 5.2 for details. Examples of published measurement errors are from KaVA (Zhao et al. 2019, open circle), at 43 GHz. Higher frequencies plotted are from Rioja and Dodson (2011) using fast switching observations with VLBA at 86 GHz (open star) and Rioja et al. (2015) using simultaneous

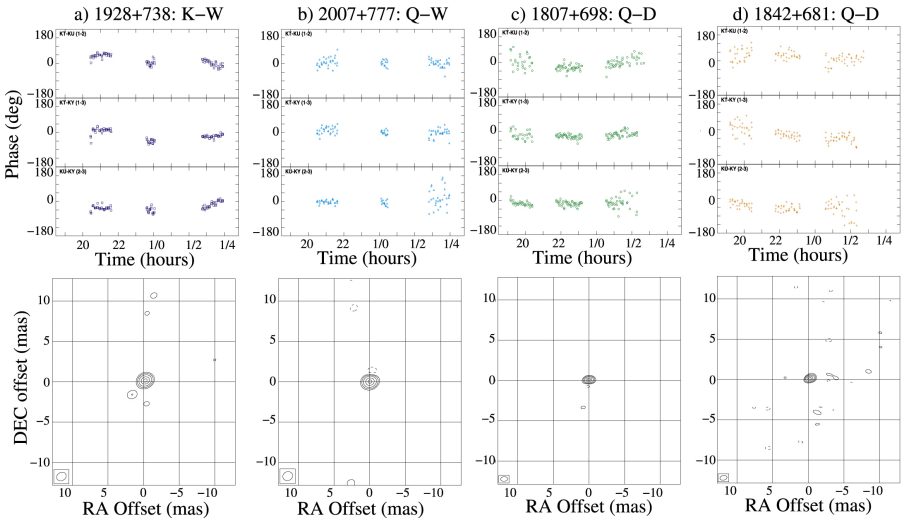

Fig. 4 Outcomes of SFPR astrometric analysis using KVN observations at the four frequency bands K/Q/W/D (22/43/86/130 GHz, respectively), from Rioja et al. (2015). Upper row: SFPR residual visibility phases for source and frequency pairs. The target source and target frequency band (i.e., $\nu^{\rm high}$), along with the angular separation from reference source, the reference frequency band (i.e., $\nu^{\rm low}$), and the frequency ratio $\mathcal{R}$, in parentheses, are specified next for each plot. From left to right: 1928+738 at W band (6° separation from reference, K band, $\mathcal{R} = 4$); 2007+777 at W band (6° separation, Q band, $\mathcal{R} = 2$); 1807+698 at D band (8° separation, Q band, $\mathcal{R} = 3$); 1842+681 at D band (10° separation, Q band, $\mathcal{R} = 3$). Lower row: SFPR astrometric maps from left to right: 1928+738 at 87 GHz (W band), 2007+777 at 87 GHz; 1807+698 and 1842+681 at 130 GHz (D band). Peak fluxes are 2 Jy beam^{-1}, 266 mJy beam^{-1}, 415 mJy beam^{-1}, and 216 mJy beam^{-1}, respectively. The contour levels in the maps start from 0.75% of the corresponding peak fluxes, respectively, and double thereafter in all cases. Each map includes a negative contour level at the same percent level of the peak flux as the first positive one. The beam size is indicated at the bottom left of the image.

multi-frequency observations with KVN at 86 GHz and 130 GHz (open square), referenced to 43 GHz. All of the KVN and KaVA SFPR results are scaled to 6,000 km and 5° and are dominated by the thermal errors. Figure 4 shows the astrometric measurements at the highest KVN band, 130 GHz, using pairs of sources several degrees apart; full details are in Rioja et al. (2015). The SFPR-calibrated visibility phases are shown along with the SFPR images at 86- and 130-GHz, after correcting with simultaneous observations at 22- or 43-GHz. Small core-shifts for these sources could be detected, although this analysis was limited by the resolution from the relatively short KVN baselines. Recent and on-going developments towards a global simultaneous multi-frequency ready network will enable high precision astrometry measurements at frequencies never achieved before. SFPR underpins the successful KVN AGB KSP, which is discussed in Sect. 8.2.4.

7 Technological developments

Since its beginnings astrometry has benefited from the relentless pursuit of technological developments in radio astronomy, that have allowed leaps in performance. Historical examples of this would be the ever increasing capability to record wider bandwidths (that improves the sensitivity, therefore reduces the thermal noise errors and enables faster source switching for more precise phase and delay measurements) and the dual band S/X receiver system (that allowed for the formation of 'ionosphere-free' data products). In parallel improvements in the a priori models have reduced the intrinsic residuals to manageable levels. These include improved station coordinates and atmospheric models (from GPS data for example), amongst others. Current ongoing developments are providing the required technological solutions to enable optimum performance of the next-generation calibration astrometric methods described above. They address the required capacity for broadband and simultaneous multiple-frequency bands and multiple-calibrator observing modes, for antenna arrays and single dish telescopes.

7.1 Capability for multi-frequency observations

There are clear science benefits from observations of the sky in a large range of radio frequencies. The previous state-of-the-art has been to use a combination of different radio receivers, each optimised for a specific range of frequencies to provide a wide frequency coverage. Frequency agility comes from, for example, switching between these receivers, which can be done within 10 secs for VLBA (USA), 30 secs at Effelsberg-100m (Germany) and 1 min at the TianMa-65m (China). New developments include the capability for simultaneous observations at multiple frequency bands and broadband systems, with continuous frequency coverage that is up to one order of magnitude increased over the previous generation of receivers. Broadband, multi-frequency systems have played an essential role in breaking through the frequency thresholds for precision astrometric measurements. Likewise the next-generation of instruments will open up both the low and high frequency regimes.

7.1.1 Simultaneous multiple frequency systems

The KVN innovative engineering solution for mm-VLBI provided a breakthrough in both astrometry and also the detection of weaker sources through extended coherence times, using a simultaneous multi-band quasi-optical design for 22/43/86 and 130 GHz (Han et al. 2013), which is shown in Fig. 5 *left*.

The impact of this multi-band system on spectral line VLBI is significant, as several different maser types in different frequency bands could be observed simultaneously, to obtain images of the emission with bona-fide astrometric registration for the first time; Dodson et al. (2017a) provides a compilation

Fig. 5 Two broad band technological solutions: *left)* The mm-wave KVN optical bench, with separate receivers (with equalised path length) for simultaneous observations at 22, 43, 86 and 130GHz. *right)* the RadioNet BRoad bAND (BRAND) QRFH cm-wave receiver, which is able to record a decade of bandwidth from 1.5 to 15.5 GHz (Flygare and Pantaleev 2019).

of possible scientific applications and the performance impact is estimated in Sect. 7.1.3.

The Compact Triple-band Receiver (CTR) (Han et al. 2017), is a new and much more compact implementation of the KVN multi-frequency receivers, with three frequency bands, K (18-26GHz), Q (35-50GHz) and W (85-115GHz), fitted into a single cryostat. The reduction in size makes this technical solution very versatile for installation in telescopes where space availability is an issue, as is usually the case. A similar configuration is being developed for the Yebes-40m (Spain) (Tercero and García-Pérez 2019). Their new Q-band (31.5–50.0 GHz) and W-band (72–116 GHz) receivers, combined with the existing K-band receiver, provide an alternative solution to the CTR that has slightly wider bandwidths. Both these systems show that there is great promise for providing mm-wavelength multi-band capability to a wide number of observatories, greatly enhancing the VLBI array suitable for SFPR and the next-generation instruments (as discussed in Sections 5.2 and 4.2, respectively).

7.1.2 Broadband receivers

We note that a wide-band receiver can cover multiple 'traditional' frequency bands, hence also providing the simultaneous multi-band observing capability. In the cm-wavelengths, BRAND-EVN (BRoad bAND European VLBI Network) (Alef et al. 2018; Flygare and Pantaleev 2019) is a RadioNet project to build a prototype quad-ridge flared horn (QRFH) prime-focus receiver for Effelsberg-100m (and other telescopes) that spans 1.5 to 15.5 GHz, which is shown in Fig. 5 *right*. It follows on from earlier designs, such as the decade-bandwidth log-periodic dual-dipole geodetic VGOS system called the 'eleven-feed', which covered the ultra-wide bandwidths required for that project (2–

13 GHz) (Yang et al. 2011). These systems enable the observations of radio sources over the whole usable band, simultaneously.

Achieving its full potential sensitivity requires the sub-bands to be coherently connected (via fringe-fitting) over the full band, which in turn preserves the chromatic astrometry information and results in astrometrically registered images of the emission from a source at the different observed sub-bands (in a similar fashion as above, in mm-waves). The RadioNet project RINGS (Radio Interferometry Next Generation Software) is a processing development to address the challenges resulting from the fringe-fitting analysis of such wideband data, among them a new functionality for the simultaneous calibration of both atmospheric contributions to the observables (with their distinct frequency dependencies) as well as the intrinsic chromatic effects from the sources themselves.

Other recent similar receiver designs are the ultra-wideband low (UWL) receiver for Parkes (Dunning et al. 2015; Hobbs et al. 2020) that covers 700 to 4030 MHz; two complementary wideband systems (UWMid, UWHigh) that would operate from 4 to 25 GHz are in the design phase.

7.1.3 Simulation studies with simultaneous multi-frequency observations for mm-VLBI astrometry with the ngVLA

In this section we consider the impact on the calibration performance from using frequency-switching compared to the simultaneous multi-frequency capability, for the ngVLA (or any other interferometer). This work was carried out under the ngVLA Community Studies program. We used the ARIS simulator (Asaki et al. 2007), which has very complete tropospheric and ionospheric models, to generate synthetic datasets with realistic atmospheric conditions over a subset of ngVLA stations. These comprised of SFPR observations with 16 antennas, with baselines from 27 to 500 km (spanning the edge of the core and the longest baselines of the proposed array), with a range of duty cycles for the frequency-switching between zero (i.e., simultaneous) and up to 60 sec. The array response to point sources was generated, with zero thermal errors and nominal atmospheric conditions, at the four frequency bands of the KVN. The lowest frequency (22 GHz) was used as the reference band for the SFPR analysis for all the other bands.

Our first metric was the fractional flux loss (FFL; 1-FFR) measured from the SFPR images compared to the input model, when the simulated data were calibrated using interleaved observations with a 30sec frequency duty cycle. This allows a direct measurement of the phase variance via the FFL. Additionally we considered the effect of phase-connection errors, which approximates the first metric. We estimated the loss of phase-connection by comparing the forward predicted phase (using the rate and phase solutions) to the actual phase, for a range of duty cycles. We define failure as where the error is greater than a half cycle. Longer intervals, obviously, more often fail to correctly predict the actual phase. Figure 6 shows, with lines, the fraction of incorrectly

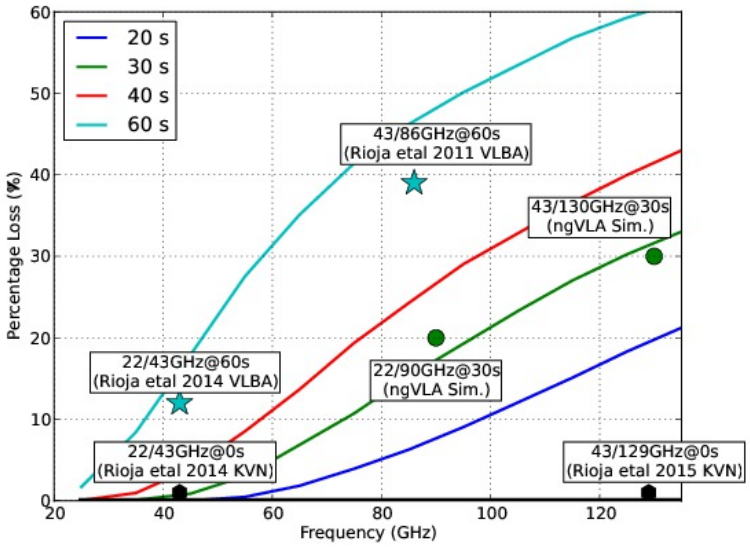

Fig. 6 Simulated phase-connection losses in multi-frequency calibration, as a function of frequency and of frequency-switching duty cycle, with lines for 60 sec (cyan), 40 s (red), 30 s (green) and 20 s (blue). Simultaneous observations have zero losses and are indicated with a black line superimposed on the x-axis. In all cases the simulations were thermal noise free. Overplotted as symbols are the fractional flux losses in the images made from the same simulated datasets, using SFPR with 30 s frequency-switching, in green circles, and empirical results from the literature using VLBA and KVN observations (cyan stars and black hexagons respectively Rioja and Dodson 2011; Rioja et al. 2014, 2015); labels list the reference and target frequencies and the duty cycle, along with the publication. Losses are over 10% at the highest frequencies (>100 GHz) even for the fastest conceivable duty cycle of 20 s, whereas simultaneous observations would have zero losses.

predicted solutions, up to a target frequency of 130 GHz. Overplotted as symbols are results from the SFPR imaging of the simulated ngVLA data and empirical results from the literature. The two metrics agree well with each other, and are in reasonable agreement with the empirical KVN and VLBA results, for which the weather conditions were excellent rather than nominal.

Figure 6 shows that, above 100 GHz, the losses are over 10%, even for the fastest conceivable duty cycle of 20 sec, whereas simultaneous observations would have zero losses. Note that even at lower frequencies, for weaker sources, one would still introduce significant errors, as the duty cycles would have to be longer to overcome thermal limits; however simultaneous observations would still result in zero interpolation errors. These studies underline the benefits of simultaneous multi-frequency observations, and support the additional effort required to design systems with this capability, at least for arrays observing at mm-wavelengths ($\geq$22 GHz).

7.2 Multiple-pixel radio telescopes

The scientific impact of the next-generation instruments can be improved not only by increasing sensitivity, but also by increasing the FoV, as both of these increase the survey speed. Here we discuss innovative technologies that provide multiple tied-array beams and multi-beam receivers, for connected arrays and single dishes elements of a VLBI array, respectively.

7.2.1 Multiple tied-array beams from antenna arrays

When using a connected array as a VLBI element, such as the VLA, ATCA or WSRT, it is common to combine the signals from the array's individual antennas and provide this as a single tied-array output. The connected array needs to be self-calibrated, that is 'phased-up', before the formation of the VLBI datastream.[3] A tied-array beam (TAB) has the same FoV as the connected array synthesised beam; that significantly restricts the FoV, compared to the primary beam of a single antenna. A solution to increase the TAB size consists of using only the antennas that are close together. A more effective alternative would be to provide multiple streams, each corrected for different pointings (or phase centers) within the single antenna FoV. Such functionality would be essential for in-beam MultiView, as discussed in Sects. 4 and 5.1, for ultra-precise astrometry with the next-generation instruments. It would also enable more efficient VLBI surveys with the SKA. Historically no connected array has offered the possibility of forming such multiple TABs, but this will change in the near future. APERTIF, on the Westerbork Synthesis Radio Telescope, has had plans for this functionality (although they are currently on hold); the next correlator upgrade for ATCA (BIGCAT) will provide this, and similarly for ASKAP. This would result in the full sensitivity of the connected array, with the same potential FoV as for the individual antennas.

Multiple phase-centres (i.e., tied-array beams towards multiple directions) will be a standard offering for tied-array SKA operations; this is essential given its small synthesised beamwidth. The tied-array FoV for SKA-Mid would be around or less than an arcsecond, and this would be combined with antennas having FoVs of many arcminutes in VLBI observations.

7.2.2 Multi-beam receivers

Receiver packages hosting multi-beam receivers, that is multiple independent receiver horns, have an excellent track record in accelerating survey speeds by enlarging the FoVs. For example the Parkes Multi-Beam, which increased the effective FoV of the Parkes dish (64m) by a factor of 13, was essential for the rapid HI all-sky survey HIPASS (Barnes et al. 2001) and the HITRUN pulsar surveys (e.g., Keith et al. 2010). Note however that these traditional

[3] http://science.nrao.edu/facilities/vla/docs/manuals/obsguide/modes/vlbi
http://www.atnf.csiro.au/vlbi/dokuwiki/doku.php/lbaops/lbascheduling

multi-beam receivers do not provide continuous sky coverage as the individual beams do not overlap.

The capabilities of the multi-beam receiver also allows for simultaneous VLBI datastreams to be collected from those beams pointing at multiple VLBI targets, to be cross correlated with the single datastream from a smaller antenna. Such a proof-of-concept was performed with the Parkes Multi-Beam to the ASKAP test-bed (12m), also located at Parkes, as part of the preparatory work for ASKAP (Rioja et al. 2011b). A more interesting demonstration would be to cross correlate the SKA-scale collecting area of FAST (500m), which is equipped with an operational Multi-Beam receiver providing 19 dual polarised beams spread over the same FoV as a 30m antenna, with other VLBI antennas. As yet no such demonstration has been performed.

7.2.3 Phased Array Feeds

The most applicable example of increasing the FoV is provided by phased array feeds, which provide a uniform access to any part of the sky within the enlarged FoV, see Fig. 7. Phased Array Feeds (PAF) at the focus of a parabolic radio telescope address one of the great limitations of single telescopes and arrays; that they only see one point in the sky, the equivalent of a single pixel camera. When used as part of a connected array this limitation is offset by the fact that one can form a high resolution image of the radio sky within that single pixel. Nevertheless, it was recognised that with the capabilities of modern backends one can do much better than this (see discussion in Fisher and Bradley 2000). PAFs on large single dish antennas allow these highly sensitive telescopes to observe a greater portion of the sky. The technologies behind the APERTIF and ASKAP PAFs apply multi-beam approaches to interferometres, each pixel being in essence a separate interferometric array with a slightly offset pointing centre. The benefits for precision astrometry is when these PAF-enabled instruments form an element in the VLBI array. The most effective implementation of this is to match the FoV of the highly sensitive, larger single dishes, to the larger FoV of the less sensitive, smaller single dishes (see discussion in Rioja et al. 2008), for calibration using MultiView (Sect. 5.1). The antenna arrays currently fitted with PAFs are all comprising smaller dishes, so the benefit for VLBI is less. In these cases the multiple tied-array beam forming (Sect. 7.2.1) is the most applicable capability. In the future we can expect to perform SKA-VLBI observations with the multiple TABs of SKA, plus a network of large telescopes with PAFs and medium size single pixel telescopes, as illustrated in Fig. 1. Currently large telescopes equipped with PAFs, such as Effelsberg (100m), Jodrell Bank (76m) or (planned) FAST (500m), Parkes (64m) and GreenBank (100m), could serve as pathfinders for MultiView in the SKA-era. Parkes has just been funded to implement a new version of the ASKAP PAF (Dunning et al. 2016), which combines the Vivaldi feeds of APERTIF and the checker-board technologies of ASKAP with cryogenic cooling. It is expected that this will reduce the effective system temperature T_{sys}/η_{eff} from about

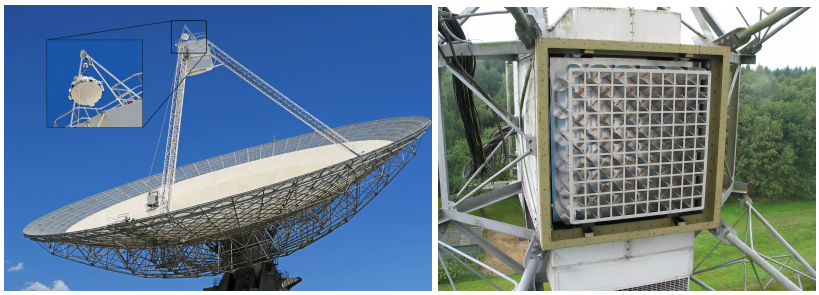

Fig. 7 Phase Array Feeds on Parkes-64m (left) and WSRT (right) telescopes, respectively. Shown are the Mk-II CSIRO PAF (originally designed for ASKAP and modified for Effelsberg-100m), where a PCB checker-board element approach is taken, and APERITIF for WSRT, which uses an array of Vivaldi elements. Image credit: CSIRO and ASTRON.

74K for the ASKAP system to 27K for the CryoPAF, delivering a large boost in performance.

7.2.4 Empirical atmospheric studies for estimating MultiView astrometric limits

A crucial question for MultiView astrometry is to characterise to what level the atmospheric residuals can be minimised by the spatial interpolation between the solutions of multiple calibrator sources. G. Keating has been testing strategies to correct for tropospheric gradients for Sub-Millimeter Array (SMA) observations at 230GHz using tip-tilt corrections (Keating, in prep.). Fig. 8 *left* shows an example of the Allan Standard Deviation (ASD) formed from the post-correction residual phases. Baselines of 300m are equivalent to about 6° on the sky, which is the maximum scale of interest for phase referenced VLBI. In the example shown the ASD falls as $\tau^{-2/3}$ at long timescales, which indicates that the residuals act as if they are from a thin 2D screen. On shorter timescales, when the thermal noise levels dominate, the ASD initially follows a $\tau^{-1/2}$ relationship, before transitioning to $\tau^{-2/3}$ after about 100 seconds. The ASD at 300 seconds is always better than $\sim 3 \times 10^{-15}$ for 100m baselines and is the equivalent to about 0.01mm of uncompensated residual excess path length (i.e., $\Delta\ell_z^{MV}$).

To quantify the ionospheric residuals we use measurements at m-wavelengths from the SKA-Low precursor, the Murchison Widefield Array (MWA), which are fully discussed in Dodson and Rioja (2018). To characterise the effects of the fine scale spatial structure we have used the by-products of the calibration method LEAP (Rioja et al. 2018). This method provides the station-based phase solutions of all calibrators lying within the very large FoV, as shown in Fig. 8 *right*. These solutions can be used to characterise the smoothness of the TEC screen, at the sub-degree scale for the calibrator directions. This is the regime most relevant to the SKA. We have taken a set of calibration solutions from observations carried out on 18 Dec 2017, which has been classified as of moderate weather. All of these datasets were from the extended MWA

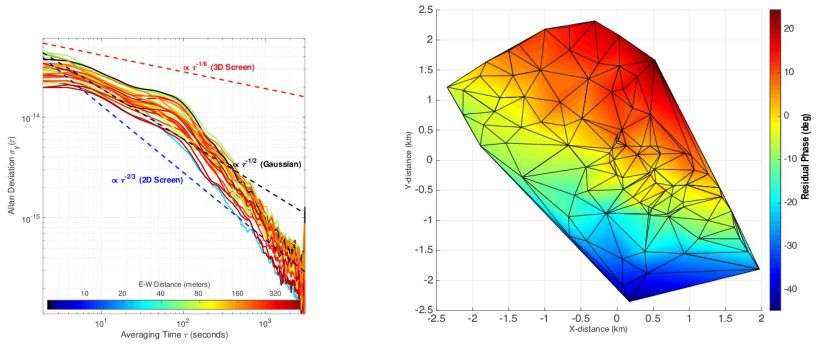

Fig. 8 *Left*: An example of the tropospheric structure function from tip-tilt corrected observations with the SMA at 230 GHz from Keating etal. (in prep.). The Allan Standard Deviation for each telescope pair is plotted, with colours indicating the baseline length along EW. The longer-term trend suggests the limiting systematic residual errors are from a 2D thin screen over the array, which extends to ∼6° (assuming the dominant water layer is at 3km). *Right*: An example LEAP measurement of the ionospheric directional dependent phase surface over MWA Phase-2 at 150 MHz. The typical phase residual after subtracting a planar fit is equivalent to 1 milliTECU (Dodson etal., in prep). The phase screen extends out to ∼1° for MWA Phase-2, with a dense sampling due to the 128 antennas.

Phase-2 array, with a maximum baseline of about 6km; this corresponds to a maximum angular scale is 1° for a nominal ionospheric height of 300 km. We assumed that the measured TEC surfaces could be approximated by planar surfaces (or other low-order polynomials) and measured the residuals of the fits. We limited ourselves to the strongest (>25 Jy) sources within each FoV, because it is vital to obtain results with the smallest possible intrinsic thermal noise. The LEAP measurements show an RMS of uncompensated residual excess TEC of ∼1 milli-TECU (i.e., ΔI^{MV}) after a planar fit has been subtracted for 90% of cases. Therefore in the majority of cases there are no significant deviation from a linear gradient at small (<1°) angles. These results predict that MultiView, with three calibrators up to ∼60′ away, would result in ∼5 μas astrometric precision at 1.6 GHz for most weather conditions with next-generation instruments. Additional calibrators (>3) allow higher order surfaces to be fitted, and increase the range of weather conditions in which high precision astrometry can be achieved. For this reason, among others, the current recommendation for μas-precision MultiView with SKA-VLBI is that eight VLBI beams will be required. We would recommend that these calibrator sources should evenly span the FoV of the smaller antennas in the array, with the larger antenna forming multiple pointed beams towards the sources. These studies suggest that the calibrator and target sources can be separated by up to a degree (for ionospheric corrections) or more (for tropospheric corrections) without introducing non-trackable changes in the phase screen. It is worth noting that we also used results from the MWA Real Time System (Mitchell et al. 2008), to show that the larger residuals from MultiView with angular separations up to 6° (Dodson and Rioja 2018) should match the sen-

sitivity of current instruments. This has been confirmed in Rioja et al. (2017) with 6° source separation at 1.6 GHz and with recent VLBI test observations using OzScope (Hyland 2020) with sources separated by up to 8° at 8 GHz. These atmospheric studies provide the basis for the MultiView astrometric error estimates listed in Column 3 of Table 2 and in Fig. 2 and Sec. 9. Note that there is no dilution effect for these MultiView residuals.

8 Astrophysical applications with current instruments

Here we review some of the recent published results from high precision radio astrometric surveys in the last few years, drawing out the important contributions from large and un-biased surveys, and link these to improvements in methods. For a more general review of the field see the references in Reid and Honma (2014).

8.1 Pulsar parallax at 1.4 GHz: PSRπ

Pulsar trigonometric distances provide important insights into pulsar emission physics, their equation of state, gravitational waves and SNR associations. Surveys allow for the construction of the 3D-structure of the free electrons in our galaxy, by connecting the pulsar dispersion measures to their trigonometric distances (Yao et al. 2017). Also, the interpretation of kick velocities to understand the properties of the binary progenitors requires accurate distances for the pulsars. The major 1.4 GHz VLBA pulsar astrometric program PSRπ has released the 'data-paper' (Deller et al. 2019) for the project, which increased the number of more distant (>2kpc) pulsars with accurate distances by a factor ten. PSRπ is a beautiful demonstration of a successful in-beam PR survey. Out of the 110 initial pulsars proposed an in-beam reference source could be detected for 60 targets. The minimum pulsar-reference source separation was only $0.8'$ and the median angular separation was $14'$. The median pulsar parallax error is 45μas, from typically nine epochs of observations (i.e., $\sim$135μas astrometric error per epoch). It is worth noting that the astrometric errors for these close-but-weak sources are dominated by the thermal errors. This is shown in Fig. 9, where the analysis from Deller et al. (2019) is contrasted to that in Kirsten et al. (2015) (which includes data from Chatterjee et al. (2004)). Deller et al. (2019) (Eqs. 1 and 2) reach the same conclusions as described in Sect. 5.1 above; that to achieve systematic errors at the level of 10 μas per epoch of in-beam PR observation the angular separation should be $\sim 1'$, and that the sources should be strong enough so that thermal errors do not dominate, that is the DR should be 1000:1. This underlines the strength of MultiView, for which the effective angular separation can be essentially zero, whilst using strong and widely separated reference sources to provide the matching precision.

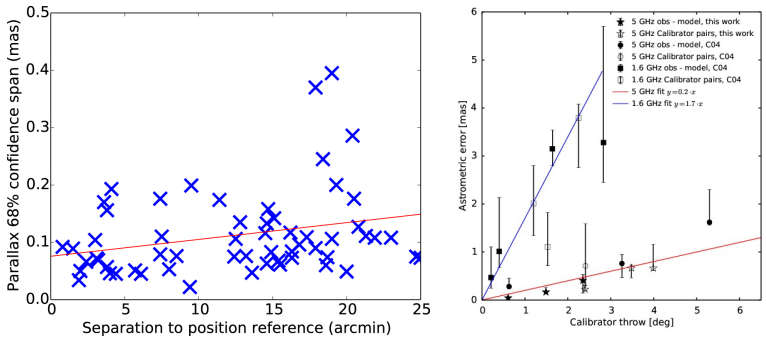

Fig. 9 Comparisons of PR-type astrometric errors achieved with existing instruments as a function of angular separation between target and reference sources, from *left)* Deller et al. (2019, Fig. 8) at L-band, for the parallax error and from *right)* Kirsten et al. (2015, Fig. 1) for the per epoch astrometric error that includes data from Chatterjee et al. (2004, Fig. 3), at 1.6 and 5 GHz. For the conventional PR (*right*), where calibrators will not be thermally limited in general, the dependence on angular separation is clear, which indicates that the errors are systematic. On the other hand for in-beam PR (*left*) the dependence on solely angular separation breaks down, due to the low SNR; that is as in-beam calibrators tend to be weaker the thermal and the systematic errors are approximately equal. Thus increased sensitivity with the next-generation of instruments will not result in higher astrometric precision, with these traditional methods. This is because the sensitivity will either allow the use of closer but weaker calibrators that match the current DR and result in thermal-error limited astrometry, or calibrators at approximately the same separation as currently, that would then result in systematic-error limited astrometry. The right-hand plot also demonstrates the difference in PR astrometric quality at 1.6 and 5 GHz from real experiments, as indicated by the fits to the 5GHz and 1.6GHz data; the slopes are steeper than the expectations from Asaki et al. (2007) (which is 1 mas/°at 1.6 GHz), but the ratio of the slopes agree, to within errors.

8.2 Galactic astrometry

8.2.1 Galactic structure: BeSSeL and VERA

It is extremely challenging to derive the structure of the Milky Way using observations from the inside, particularly with optical observations that are effectively blocked by dust extinction along the plane. Radio observations of HI and particularly maser astrometry therefore provide a unique insight. The combined on-going efforts from VLBI astrometric projects carried out mainly with the VLBA and VERA are significantly revising our knowledge of the Galaxy (Reid et al. 2019; VERA Collaboration et al. 2020, respectively). These observations result in high-precision astrometric measurements of the source coordinates, trigonometric parallax distances, proper motion and radial velocity towards a few hundred high mass star-forming regions (Reid et al. 2019; VERA Collaboration et al. 2020, references therein). The targets are mainly massive young stars with 22 GHz H_2O and 6.7 GHz methanol maser sources, with a few additional methanol masers at 12 GHz. These astrometric surveys are revealing the three-dimensional spiral arms structure of the Milky Way

with unprecedented accuracy. A highlight is a record breaking distance measurement, for the H_2O maser G007.47+00.05, with a parallax of $49 \pm 6\mu$as, equivalent to a distance of $20.4^{+2.8}_{-2.2}$ kpc (Sanna et al. 2017). In the latest results Reid et al. (2019); VERA Collaboration et al. (2020) have used the combined set of astrometric measurements to refine the underlying dynamical model described by the fundamental constants R_0 and θ_0, the distance to the Galactic Center and the circular rotation speed of the Local Standard of Rest (LSR), respectively. The parameter values from the latest modelling of Reid et al. (2019) are $R_0 = 8.15 \pm 0.15$ kpc and $\theta_0 = 236 \pm 7\,\mathrm{km\,s^{-1}}$. For VERA Collaboration et al. (2020) the results are $R_0 = 7.92 \pm 0.16_{\mathrm{stat}} \pm 0.3_{\mathrm{sys}}$ kpc and $\theta_0/R_0 = 30.17 \pm 0.27_{\mathrm{stat}} \pm 0.3_{\mathrm{sys}}\,\mathrm{km\,s^{-1}\,kpc^{-1}}$. These results include, for the first time, precise astrometric results from observations of 6.7 GHz methanol masers, e.g., Xu et al. (2016); Wu et al. (2019); Sakai (2018); Sakai et al. (2019b); Zhang et al. (2019) and Rygl et al. (2018). The important advance over the pure ATC corrections from the use of the image-based variation of MultiView for 6.7 GHz observations is indicated by the improvement between the first and the later results (see Fig. 2). Additionally, the LBA is now delivering its first methanol maser parallax measurements (Krishnan et al. 2015, 2017) that fill in the fourth quadrant. Observations towards the Galactic centre are extremely important to improve the dynamical models, and these could be provided by observations from the Southern hemisphere, such as with the SKA. In the meantime this can be attempted with MultiView astrometry with established arrays in the Northern hemisphere to correct for the larger errors due to the low elevation observations.

8.2.2 Spiral arms and density waves

The BeSSeL results are also revising our knowledge of the structure of the local arm, revealing it as a major spiral structure with star-forming activity similar to that in the Galaxy's major spiral arms (Xu et al. 2016). Honma et al. (2015) presented simulation studies that suggested the feasibility of using astrometric measurements of a few hundred sources at the current level of accuracy to discriminate between different dynamical models proposed to explain the nature and characteristics of the spiral arms. That is, between the quasi-stationary density wave theory (Lin and Shu 1964) and non-steady spiral arms, based on numerical simulations (Baba et al. 2015, 2013). The former predicts that the dust and stars will be separated within the arms, whilst the latter predicts that they will be co-located. Work by Hachisuka et al. (2015); Sakai et al. (2015); Griv et al. (2017); Sakai (2018); Sakai et al. (2019b) compared the empirical results with the predictions. Griv et al. (2017) argued that the data supports density wave theory, based on the earlier dataset in Reid et al. (2014). This is refined in the work of Sakai etal. (2015; 2019b) on the Perseus arm that suggests the addition of shocks to the density wave theory is required to explain their results. However they note that the full picture is almost certainly more complicated than this, as results for other regions appear less clear or even contradictory.

Sakai et al. (2019a) has recently published a VERA study on the outer rotation curve, in which they add a further four H_2O maser distance measurements to the literature. They use these to determine that the maximum height of the Galactic warp increases with Galactocentric distance and has an oscillatory behaviour. They suggest that these are possibly induced by the close passage of the Sagittarius dwarf galaxy.

8.2.3 Early stages of stellar evolution: POETS

Moscadelli et al. (2016) presented the first results of the Proto-stellar Outflows at the EarliesT Stages (POETS) survey. The POETS survey has the goal of imaging the outflows for hundreds of Young Stellar Objects (YSOs), at resolutions of a few mas and a few km s^{-1}. As such it has afforded, for the first time, a VLBI survey of the properties of the most widespread interstellar masers based on a large, homogeneous dataset. POETS uses the BeSSeL measurements of parallax and proper motion of H_2O masers, combined with additional proper motion studies of 6.7 GHz methanol masers, and continuum observations between 4 and 26 GHz carried out at lower-resolution with the JVLA. Sanna et al. (2018) reported on and interpreted the radio continuum data of the whole sample, and Moscadelli et al. (2019) completed the combined analysis of the radio continuum and H_2O maser observations for all the targets, focusing in particular on the H_2O maser kinematics. Recently, Moscadelli et al. (2020) has presented the statistics of the H_2O maser properties. The main result of the work so far is that the 3D velocity distribution of the H_2O masers near the YSO in all the sources of the sample can be interpreted in terms of a single physical scenario: a jet emerging from a disk-wind system. The statistical results indicate that the large majority (>80%) of the H_2O masers originate near (within 1000 AU) the YSOs, and that about half of the maser population (with intensities <100 mJy/beam) is still undetected.

8.2.4 Simultaneous multi-frequency astrometric survey of evolved stars with KVN

The Evolved Stars KVN KSP is providing new insights into the late stages in stellar evolution, illuminating the mass loss processes and the development of asymmetry in CircumStellar Envelopes (CSE), using a systematic astrometric study. The project comprises of simultaneous multi-frequency observations of 22 GHz H_2O and 43.1/42.8/86.2/129.3 GHz SiO masers towards a sample of 16 evolved stars sources, over multiple epochs with sufficient temporal sampling to trace the variations over multiple stellar pulsations. It is performed using SFPR measurements and the outcomes are bona-fide astrometrically registered high resolution VLBI images of the spatial and temporal distribution of the emission at all transitions, free of any assumptions. This has enabled astrometry for asymptotic giant branch (AGB) stars at frequencies up to a factor of three higher than any previous work. First results from these observations are now being published (e.g., VX Sagittarii (Yoon et al. 2018), R Crateris

(Kim et al. 2018) and V627 Cas (Yang et al. 2019)). Thus, the unbiased measure of overlap or offset between masers at different transitions, ring sizes and temporal evolution provides a wealth of information to: i) provide the basis to investigate the spatial structures and dynamics from the SiO to H_2O maser regions associated with a mass loss process and to trace the development of asymmetry in CSEs; ii) probe the astrochemistry of the matter thrown off into the ISM, as it is excited by the stellar pulsation of the host star; and iii) discriminate between competing proposed maser pumping mechanisms (i.e., radiative or collisional) and to deduce the physical conditions in the CSE.

8.2.5 Long-period variable star astrometry for the cosmic distance ladder

An important step on the cosmological distance ladder comes from period-luminosity relations in variable stellar sources. There are several classes of objects, and accurate distances to Galactic examples are vital for the calibration of the relationship. Mira variables and other long-period variables, which are low- to intermediate-mass (1–8$M_\odot$) AGB stars that pulsate with a period range of 100–1000 days, are the classic example for these studies. These sources are detectable to great distances, especially in the era of space infrared telescopes (Wood 2015), making them potentially a very powerful distance estimator. Optical astrometric observations of these sources have not been very reliable as AGB stellar diameters are of a similar magnitude to the parallax position shift, and their surfaces are mottled and variable. VLBI astrometry contributes to this field by providing precise trigonometric parallaxes to the 1.6 GHz OH, 22GHz H_2O and 43 GHz SiO masers associated with Galactic examples of these stars (Nakagawa et al. 2018). Recently, high-precision astrometric results, using ATC, have been obtained from observation of H_2O masers (Zhang et al. 2017; Nakagawa et al. 2016; Sudou et al. 2019). Additionally, a VERA survey using SiO masers is being developed. Alternatively, a OH maser survey using MultiView astrometry could be useful (see discussions in Orosz et al. 2017).

8.3 Extragalactic astrometry

8.3.1 Proper motion surveys of AGNs

Large surveys with precise measurements of the proper motion of distant objects allow the extraction of global signatures, such as detection of the Gravitational Wave background, the Hubble expansion and the evolution of Large-Scale Structure, when combined with the redshift measurement. Truebenbach and Darling (2017) has published a catalog of 713 VLBI proper motions of AGNs, derived from both archival and new measurements, which they have used to measure the Secular Aberration Drift. As the authors point out, this demonstrates that large precise catalogs are as useful in radio as they are in optical bands. The measurements of each individual quasar will be affected by

intrinsic core-jitter effects, however averaging over many of these uncorrelated errors using a large survey allows one to extract the global signatures. Their catalog is formed from the time-series of absolute astrometric VLBI Geodetic observations from the Goddard archive, and additional relative astrometric observations to improve on that dataset.

8.3.2 Towards global absolute phase astrometry

Abellán et al. (2018) presented a first successful demonstration of precise differential phase-delay astrometry of the angular separations between 13 radio-loud AGNs around the North Celestial Pole, that are up to 15° apart, using VLBA observations at 43 GHz. This is probably reaching the limit of the applicability of the analysis with UVPAP, given the increasing challenges for higher observing frequencies using PR. Previous demonstrations from this team were at lower frequencies (Martí-Vidal et al. 2016, and references therein). The precise astrometry measurements at 15 and 43 GHz were compared, to study the jet physical conditions, using the core-shift measurements, and to compare astrometric methods, among them SFPR. Their results agree with predictions from opacity and synchrotron self-absorption effects following the standard model for AGNs (Blandford and Königl 1979).

This determination is an important step towards wide field or global astrometry using the very precise phase observable. The precise determination of the coordinates of extragalactic sources across the sky is relevant to measuring the ICRF. Traditionally, wide field astrometry has been carried out using group-delay based analysis of geodetic VLBI observations, which traditionally has been about 30–40 fold less precise than the phase observable. Nevertheless note that geodetic VLBI is also undergoing a regeneration, as discussed in Sect. 4.5, and the approaches are converging.

8.3.3 Gamma-ray bright AGN survey: iMoGaBA

Interferometric Monitoring of Gamma-ray Bright AGNs (iMoGaBA) is a survey carried out with the KVN to investigate the origins of gamma-ray flares in AGNs (Lee et al. 2016). It is known that most compact flaring gamma-ray sources are AGNs, and determining the origin of these flares hinges on discovering their location in the jet. At the higher frequencies one expects the AGN core and the base of the jet to be exposed, as the otherwise bright synchrotron emission is reduced. Combining simultaneous high-frequency high-resolution imaging of 34 radio-loud AGNs with gamma-ray emission and radio-flux monitoring, at 22/43/86 and 130 GHz, has the potential to provide direct observations of where the emission comes from, during a flare. IMoGaBA is not strictly an astrometric survey, but uses FPT-squared (Sect. 5.3.1 and Algaba et al. 2015; Zhang et al. 2017) to detect the weaker sources; also in the extension to global baselines (AiMoGaBA) astrometry with SFPR will be added. Therefore we have included it in this review. Their observational interpretation is that the radio and gamma-ray locations are sometimes offset or orphaned

(for 1633+382 see Algaba et al. 2018) and sometimes associated with the radio lobe hot-spot for longer term variations and the core for the short term variations (for 3C 84 see Hodgson et al. 2018). AiMoGaBA will target the issue of jet base wandering after high-energy flares, first seen in Mrk 421 (Niinuma et al. 2015). This will determine whether the changes are due to alterations in the orientation of the jet or in the environment and magnetic field conditions.

8.4 Radio astrometry in the GAIAera

With the publication of GAIA Data Release 2 (DR2; Gaia Collaboration et al. 2018a), the comparison between the GAIA positions, parallaxes, and proper motions, and accurate VLBI astrometric measurements for sources that have both optical and radio detections has become a very active field of research. Multiple studies focus on different objects, among them, AGN positions (Petrov et al. 2019b), star-forming regions (Kounkel et al. 2018) and evolved stars (van Langevelde et al. 2018).

One of the interests of these comparisons is to verify these initial GAIA results. Among these, the parallax value for the Pleiades cluster is particularly important because of its role in the astronomical distance ladder. Previous comparisons of VLBI and Hipparcos parallaxes resolved the distance controversy by ruling out the Hipparcos value (Melis et al. 2014). The new GAIA results agree with all VLBI Pleiades parallax measurements of eight stars that show compact emission (Melis 2018). Similar studies of a sample of YSO candidates (GOBELINS: Ortiz-León et al. 2018) also show agreement, but hint where further improvements in the measurements of GAIA systematics could be made. Individual examples of disagreement can be found, for example on SV Peg (Sudou et al. 2019).

Xu et al. (2019) used a sample of 108 sources with both VLBI and GAIA DR2 astrometric results. The sample included many different types of stars, including YSOs, AGB stars, pulsars and other radio stars. They found excellent agreement between VLBI and DR2 parallaxes for all subsamples, except for the AGBs. These stars are generally large, variable and embedded in dusty environments, as mentioned in Section 8.2.5. Furthermore many are in binary systems, for which the orbital motions are not modelled in DR2. For these cases radio observations of the masers around AGB stars can yield parallax accuracies roughly an order of magnitude better than GAIA. The compendia of comparative studies dealing with the GAIA parallax zero point issue confirm that these are in agreement with expectations at this point in the mission (Lindegren et al. 2018), being negative and under 100μas with an average bias of -29μas.

For AGNs, Mignard et al. (2018c) reported that in general, the VLBI/DR2 position differences are small (close to their uncertainties of a few hundred μas) with some exceptions. Petrov and collaborators (Kovalev et al. 2017; Plavin et al. 2019; Petrov et al. 2019b) used the distribution of the GAIA/VLBI position angle offsets with respect to VLBI jet directions to determine the

nature of the outliers; they find that the position offsets show a preference to align along the jet. They argue that this could be caused by the presence of unresolved optical jets below the resolution of the GAIA point spread function, i.e., 100–300 mas, and propose that these VLBI/GAIA position offsets could be used for probing properties of the innermost regions (i.e., accretion disks and the relativistic jets) of the AGNs.

Several papers have been published that compare GAIA results to the proposed ICRF3 sample (Charlot et al. 2020). These suggest that ICRF3 is a better match to GAIA than ICRF2 (Frouard et al. 2018). The work to identify a suitable common set of radio stars that are to be found in both datasets, to bring the two reference frames into agreement has begun (Makarov et al. 2019; Lindegren 2020). Again this work is helping in identifying systematic errors in the GAIA results, to be corrected in the future releases.

9 Future ultra-precise astrometric possibilities with the next-generation instruments

We have presented the best outcomes at this point in time for astrometric surveys in Sect. 8, and linked these to the improvements in methods. We have listed the next-generation of methods in Sect. 5, and how those can improve the astrometric outcomes. The next step is to speculate what is possible with the combination of the next-generation of instruments (Sect. 4) with these improved methods, and what science could be targeted. These possibilities can be summarised in a similar plot to that with which we explored the current status (Fig. 2), but for the future, in Fig. 10. With the next-generation of instruments the frequency range can be enlarged to cover 0.1 to 130 GHz and with an increase in the sensitivity limits and smaller astrometric errors.

VLBI with SKA will be much more sensitive than our current thermal limitations but the baselines will still be global, so we have assumed a DR of 1000:1 and baselines of 6,000 km to provide a thermal astrometric error limit (grey dotted line) in Fig. 10. Also plotted are the estimated astrometric limits from in-beam PR systematic calibration errors with a $10'$ pair separation and ΔI=6 TECU and $\Delta\ell_z$=3 cm residuals (brown line, and as for Fig. 2), which matches the thermal potential that is achieved with the current instruments and a DR of 100:1. We repeat that to improve the astrometric accuracy significantly with a single in-beam reference source requires that both the thermal limits provide DR 1000:1 and that the reference source is as close as $1'$. The improvement of sensitivity from the SKA can provide the former or could improve the latter, but not both simultaneously. However we have shown in Sect. 7.2.4 that MultiView calibration errors (red line, as for Fig. 2) result in systematic ionospheric residuals of the order of a few milli-TECU and insignificant tropospheric residuals (equivalent to less than 1μas above 5 GHz). The increased sensitivity will improve the chances of finding multiple in-beam calibrators at frequencies $\leq$ 1.4 GHz for Phase-1 and at frequencies $\leq$ 6.7 GHz for Phase-2 (see Table 2, Col. 8). Of course at higher frequencies source-switched

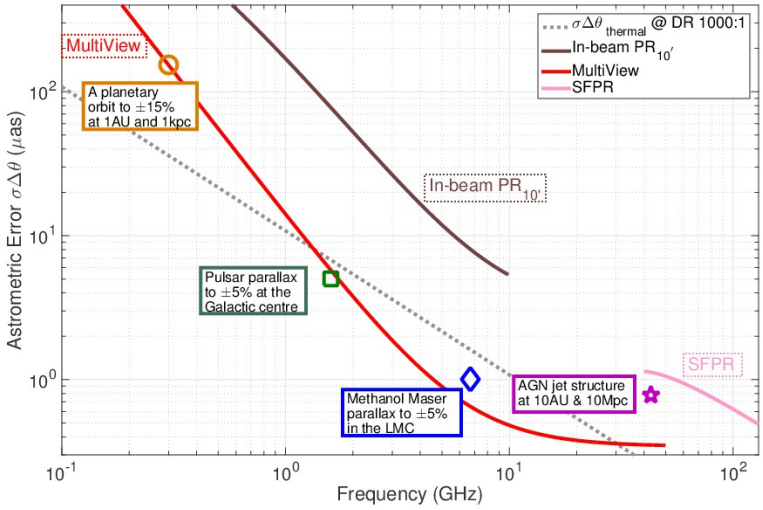

Fig. 10 Estimates of single epoch astrometric performance for the next-generation instruments, as a function of frequency between 100 MHz and 130 GHz. The grey dotted line is for astrometric errors arising from thermal noise with a DR of 1000:1 and 6,000 km baselines ($\sigma\Delta\theta_{\rm thermal}$). The solid lines are for systematic calibration errors ($\sigma\Delta\theta^{\rm cal}$) with atmospheric residuals of ΔI=6 TECU and $\Delta\ell_z$=3 cm, and angular separations of 10′, $\leq$1°, 1° for in-beam PR, MultiView and SFPR respectively. Systematic in-beam PR calibration errors (brown solid line; $\sigma\Delta\theta^{\rm PR_{10'}}$), are now far above the thermal limits indicated in grey (c.f. Fig. 2), and would therefore limit the astrometry. On the other hand the limits from MultiView (red solid line; $\sigma\Delta\theta^{\rm MV}$), above 1 GHz is below or around those from the thermal noise. The limit is around a μas, which is the probable limit of the fiducial reference points (Sec. 2.2). MultiView promises to provide astrometric accuracies at an order of magnitude lower in frequency, which match those of current best in-beam PR$_{10'}$ astrometry at 2 GHz. Therefore SKA with MultiView opens up a new window, down to 100 MHz, for precision astrometric applications and for ultra-precise astrometry at frequencies >2 GHz. Finally SFPR (pink solid line; $\sigma\Delta\theta^{\rm SFPR}$), referenced to 22 GHz and a second source at 1°, which runs from 40 to 130 GHz. This would be applicable to provide ultra-precise astrometry up to the highest frequencies of ngVLA with simultaneous multi-frequency observations. Superimposed with symbols are indicative experiments: with SKA-Low at 300 MHz we could track the orbit of a planet at 1AU around a star at 1kpc to 15% accuracy (per epoch), with SKA-Mid or ngVLA at 1.4GHz we could measure the parallax to 5% accuracy at the Galactic centre, at 6.7GHz we could measure the parallax of methanol masers in the LMC to 5% accuracy and with ngVLA at 43GHz we could measure the jet structures and core-shifts on a 10AU scale for a AGN at 10Mpc.

MultiView will be possible with SKA and ngVLA, while correcting for static systematic errors in the analysis. With such limitations we expect the MultiView astrometric errors to dominate the nominal thermal limit below 1 GHz (albeit far better than the astrometric limits currently achievable), and be below the nominal thermal limit above 1 GHz. On the other hand SFPR (pink line) potentially delivers $\sim$1μas astrometry in observations with ngVLA at high frequencies, and would probably only be limited by stability of the fiducial reference points (see Sect. 2.2).

Given these limits, science goals for VLBI with SKA-Low, with astrometry at the mas level, could be parallaxes of nearby ($\leq$1kpc) sources. For example, with SKA-Low, decametric emission from a Jupiter-like planet located at 1AU from its star would be an easily detectable (although complex to untangle) astrometric signal. Astrometric observations of pulsars at the Galactic Centre at 1.6 GHz with SKA-Mid or ngVLA would have matching thermal and systematic limits, and we should be able to reach astrometric errors of 10μas per epoch, providing a 5% error in the distance estimates. Astrometric observations of 6.7 GHz Methanol masers with SKA-Mid or ngVLA would be limited by the achievable thermal limits, and we should be able to reach errors of a few μas. Parallax and proper motion measurements of such sources in the Magellanic Clouds would determine whether the clouds are gravitationally bound to our Galaxy, or not. For ngVLA, continuum observations with sub-μas astrometric precision would be possible with MultiView and SFPR, that would probe down to 10AU for a source at 10Mpc. This is the scale where the AGNs launch the jet, so studies of the jet launching mechanism and the evolution will be very illuminating. Detailed considerations of many other potential SKA-VLBI projects have been recently published (Paragi et al. 2015, 2018; Garcia Miro 2019; Venturi et al. 2020).

The ngVLA planning for 'Astrometry and Long Baseline Science' (Reid et al. 2018) includes the goal of 1μas astrometry. Their objectives, among other possibilities, are: improved pulsar distances, to remove the Galactic rotational acceleration uncertainty from the measurements of the post-Keplerian parameters (Kramer et al. 2006); to measure the proper motion of the post-merge ejecta from neutron star-neutron star gravitational-wave sources, as demonstrated for GW-170817 by Mooley et al. (2018), which can be used to improve the measurement of H_0 using geometric constraints; tracking H_2O maser motions in the sub-parsec disks around AGNs; to probe the magnetic fields at these scales through their polarisation properties; and the proper motions of AGNs with H_2O masers in the Local Group of galaxies, following on from the work of Brunthaler et al. (2007). All of these are relative ultra-precise astrometry projects. The neutron star projects would be carried out at frequencies below 8 GHz, therefore would require MultiView calibration, for which multiple TABs will be essential. The other projects are at 22 GHz and source-switched MultiView should deliver the required astrometric precision. Not considered in Reid et al. (2018) are the possibilities for SFPR projects with frequency phase referenced λ-astrometry. An astrometric study of core-shifts and jet structure with ngVLA sensitivities, for example, will provide exquisite insight into the jet-physics and launching mechanisms from AGN black-holes, which will complement the results from the EHT. Additionally, the ngVLA would have the potential to perform astrometry on multiple maser emission lines around their stellar hosts. A large survey of the masers around the full gamut of AGB stars, with sufficient temporal sampling to track their responses to the pumping mechanism in different astro-chemical environments, would provide a huge increase in our understanding of the seeding of the ISM.

We are sure that the readers could provide a host of perhaps even more exciting ideas.

10 Summary

We are in an exciting epoch in radio astronomy, with a huge investment in future Great Observatories such as SKA and ngVLA. Additionally there are pathfinder instruments such as FAST, ASKAP, MeerKAT, KVN, LOFAR and MWA, among others. These will all be used in conjunction with other telescopes across the globe, for high resolution VLBI observations. Space-VLBI is an active field with proposals for Millimetron and Cosmic Microscope under discussion. The next-generation of instruments and the opportunities that these provide will allow for unprecedented sensitivity with increased frequency coverage and should lead to improved astrometry, provided systematic effects are compensated. VLBI provides the highest astrometry precision in astronomy currently; the next-generation instruments will maintain this leadership. Bona-fide precise astrometry adds a vital new dimension to astronomical measurements, providing positions, proper motion, distances and the direct registration of multi-epoch and multi-frequency temporal and frequency monitoring. As such it makes a fundamental contribution to many research fields in astrophysics.

This review has therefore focused on the fundamentals of high-precision astrometric VLBI, how it relates to other methods, how it has developed over time and how it could develop into the future. We have presented a common framework of the basis for all astrometric VLBI, which allows us to understand how the different approaches are related, where they will perform best and how they could further improve.

The propagation of the astronomical signal through the atmosphere introduces the dominant source of systematic errors and this then has set the limit to the frequency range, using established calibration methods. Advances have come from addressing this limitation, and have required new methods and technologies, which we describe. The frequency range for astrometry with established methods has been between 1.4 and 43 GHz, achieving the level of 10μas per epoch, in the best cases. We showed how observations at these frequencies with established methods are matching the thermal noise levels of current instruments. Additionally, established astrometric methods are currently limited to ground based arrays with accurate station positions.

To take advantage of the order of magnitude increase in sensitivity from the next-generation instruments for astrometry, systematic error calibration will have to be improved. Having made the link between the various astrometric strategies using the common framework allows us to identify the key issues. These can be addressed with next-generation calibration methods, and therefore indicate what are the technological capacities that must be in place on the next-generation of instruments. These new astrometric strategies are being demonstrated, operate beyond the range of frequencies possible with

established methods and are in active development. They are reducing the systematic limitations from the atmospheric contamination by orders of magnitude, as shown in the studies reported here. The most promising of the new methods are MultiView and Source Frequency Phase Referencing, which provide precise astrometry at the low and high frequencies, respectively. These in turn would be best implemented using simultaneous multiple beams and multiple frequency observations, respectively. Additionally, these methods are suitable for astrometry with Space-VLBI.

We reviewed the technological approaches that are providing simultaneous multiple beams and multiple frequency capabilities. For the former these are multi-beam receivers, Phased Array Feeds and Tied-Array Beams; for the latter these are multi-band and broadband receivers. The next-generation methods and technological solutions are essential considerations for the next-generation instruments, to achieve thermal noise limited astrometry. The potential, we argue, is to enable precise astrometry over 0.3 to 130 GHz and above at the level of 1μas, in the best cases. At this point the stability of the fiducial reference points would probably be the new dominant astrometric error.

We reviewed recent astrometrical publications focusing on surveys with current instruments. We emphasise the contributions to astrophysics that come from large and un-biased astrometric surveys, which is where the next-generation instruments will have the greatest impact. These surveys covered a large range of targets, such as pulsars, masers, stars and AGNs, to derive neutron-star physics, dynamic Galactic parameters, astrochemical conditions, gamma-ray origins and cosmology. We explored potential science cases for the next-generation instruments given the increased frequency range and precision.

The next-generation observatories, and their pathfinders, are working towards ultra-precise ($\sim$1μas) astrometry, and ensuring that the technological capabilities for optimum performance of next-generation methods are implemented. The prospects are therefore excellent for precise to ultra-precise astrometry across the whole radio band and the future for radio VLBI-astrometry is bright.

Acknowledgements This work was supported in part by funding from the European Union's Horizon 2020 research and innovation program under grant agreement No 730562 [RadioNet] and 730884 [VLBI with the SKA]. It was also supported by the ngVLA Community Studies program, coordinated by the ngVLA design and development project of the National Science Foundation and operated under cooperative agreement by Associated Universities, Inc. ADS was used heavily to search for relevant publications and provide references. We have discussed the ideas and issues in this document with many experts and young enthusiastic up coming researchers, to whom we are grateful for their time. In particular Ed Fomalont, Walter Alef, Mark Reid, Patrick Charlot, Mareki Honma, Simón Al-Tariqa, Richard W. Porcas, Luca Moscadelli and Huib van Langevelde have been reference points for us, as for many other people. The comments from the anonymous referees were much appreciated. F. Kristen provided the raw data for Fig. 9b, to allow the re-fitting. We thank A. Deller, F. Kristen, J. Flygare, G. Keating, ASTRON and CSIRO for the reproduction of their figures.

References

Abellán FJ, Martí-Vidal I, Marcaide JM, Guirado JC (2018) Core-shifts and proper-motion constraints in the S5 polar cap sample at the 15 and 43 GHz bands. A&A614:A74, DOI 10.1051/0004-6361/201731869

Alef W (1988) Test of Phase-Reference Mapping for Switched Observations. In: Reid MJ, Moran JM (eds) The Impact of VLBI on Astrophysics and Geophysics, IAU Symposium, vol 129, p 523

Alef W, Tuccari G, Dornbusch S, Wunderlich M, Pantaleev M, Flygare J, Tercero F, Schoonderbeek G, Hargreaves J, de Wild R, Bezrukovs V, D GJ, López-Pérez JA (2018) BRAND - the next generation receiver for VLBI. In: 14th European VLBI Network Symposium and Users Meeting, p 081, DOI 10.22323/1.344.0081

Algaba JC, Zhao GY, Lee SS, Byun DY, Kang SC, Kim DW, Kim JY, Kim JS, Kim SW, Kino M, Miyazaki A, Park JH, Trippe S, Wajima K (2015) Interferometric Monitoring of Gamma-Ray Bright Active Galactic Nuclei II: Frequency Phase Transfer. J Korean Astron Soc 48:237–255, DOI 10.5303/JKAS.2015.48.5.237, 1510.05817

Algaba JC, Lee SS, Kim DW, Rani B, Hodgson J, Kino M, Trippe S, Park JH, Zhao GY, Byun DY, Gurwell M, Kang SC, Kim JY, Kim JS, Kim SW, Lott B, Miyazaki A, Wajima K (2018) Exploring the Variability of the Flat Spectrum Radio Source 1633+382. I. Phenomenology of the Light Curves. ApJ852(1):30, DOI 10.3847/1538-4357/aa9e50, 1711.10120

An T, Jaiswal S, Mohan P, Zhao Z, Lao B (2019) A cosmic microscope to probe the universe from present to cosmic dawn:dual-element low-frequency space vlbi observatory. Chinese Journal of Space Science 39(2):242, DOI 10.11728/cjss2019.02.242

Asaki Y, Saito M, Kawabe R, Morita KI, Sasao T (1996) Phase compensation experiments with the paired antennas method. Radio Science 31:1615–1626, DOI 10.1029/96RS02629

Asaki Y, Sudou H, Kono Y, Doi A, Dodson R, Pradel N, Murata Y, Mochizuki N, Edwards PG, Sasao T, Fomalont EB (2007) Verification of the Effectiveness of VSOP-2 Phase Referencing with a Newly Developed Simulation Tool, ARIS. PASJ59:397–418, DOI 10.1093/pasj/59.2.397, 0707.0558

Asaki Y, Maud LT, Fomalont EB, Phillips NM, Hirota A, Sawada T, Barcos-Muñoz L, Richards AMS, Dent WRF, Takahashi S, Corder S, Carpenter JM, Villard E, Humphreys EM (2020) ALMA high-frequency long baseline campaign in 2017: Band-to-band phase referencing in submillimeter waves. Astrophys J Suppl Ser 247(1):23, DOI 10.3847/1538-4365/ab6b20

Baba J, Saitoh TR, Wada K (2013) Dynamics of Non-steady Spiral Arms in Disk Galaxies. ApJ763:46, DOI 10.1088/0004-637X/763/1/46, 1211.5401

Baba J, Morokuma-Matsui K, Egusa F (2015) Radial distributions of arm-gas offsets as an observational test of spiral theories. PASJ67(4):L4, DOI 10.1093/pasj/psv048, 1505.02881

Barnes DG, Staveley-Smith L, de Blok WJG, Oosterloo T, Stewart IM, Wright AE, Banks GD, Bhathal R, Boyce PJ, Calabretta MR, Disney MJ, Drinkwater MJ, Ekers RD, Freeman KC, Gibson BK, Green AJ, Haynes RF, te Lintel Hekkert P, Henning PA, Jerjen H, Juraszek S, Kesteven MJ, Kilborn VA, Knezek PM, Koribalski B, Kraan-Korteweg RC, Malin DF, Marquarding M, Minchin RF, Mould JR, Price RM, Putman ME, Ryder SD, Sadler EM, Schröder A, Stootman F, Webster RL, Wilson WE, Ye T (2001) The HI Parkes All Sky Survey: southern observations, calibration and robust imaging. MNRAS322(3):486–498, DOI 10.1046/j.1365-8711.2001.04102.x

Bartel N, Herring TA, Ratner MI, Shapiro II, Corey BE (1986) VLBI limits on the proper motion of the 'core' of the superluminal quasar 3C345. Nature319(6056):733–738, DOI 10.1038/319733a0

Blandford RD, Königl A (1979) Relativistic jets as compact radio sources. ApJ232:34–48, DOI 10.1086/157262

Bonaldi A, Bonato M, Galluzzi V, Harrison I, Massardi M, Kay S, De Zotti G, Brown ML (2019) The Tiered Radio Extragalactic Continuum Simulation (T-RECS). MNRAS482(1):2–19, DOI 10.1093/mnras/sty2603, 1805.05222

Born M, Wolf E (1999) Principles of Optics. Cambridge University Press, Cambridge, UK

Braun R, Bourke T, Green JA, Keane E, Wagg J (2015) Advancing Astrophysics with the Square Kilometre Array. In: Advancing Astrophysics with the Square Kilometre Array (AASKA14), p 174

Brisken WF (2001) High-precision pulsar astrometry using the VLA and VLBA interferometers. PhD thesis, Princeton University (USA)

Brisken WF, Benson JM, Beasley AJ, Fomalont EB, Goss WM, Thorsett SE (2000) Measurement of the Parallax of PSR B0950+08 Using the VLBA. ApJ541:959–962, DOI 10.1086/309492, astro-ph/0005324

Brisken WF, Benson JM, Goss WM, Thorsett SE (2002) Very Long Baseline Array Measurement of Nine Pulsar Parallaxes. ApJ571:906–917, DOI 10.1086/340098, astro-ph/0204105

Brunthaler A, Reid MJ, Falcke H (2005) Atmosphere-Corrected Phase-Referencing. In: Romney J, Reid M (eds) Future Directions in High Resolution Astronomy, Astronomical Society of the Pacific Conference Series, vol 340, p 455, astro-ph/0309575

Brunthaler A, Reid MJ, Falcke H, Henkel C, Menten KM (2007) The proper motion of the Local Group galaxy IC 10. A&A462(1):101–106, DOI 10.1051/0004-6361:20066430, astro-ph/0610774

Carilli CL, Holdaway MA (1999) Tropospheric phase calibration in millimeter interferometry. Radio Science 34:817–840, DOI 10.1029/1999RS900048, astro-ph/9904248

Charlot P, Jacobs CS, Gordon D, Lambert S, de Witt A, Böhm J, Fey AL, Heinkelmann R, Skurikhina E, Titov O, Arias EF, Bolotin S, Bourda G, Ma C, Malkin Z, Nothnagel A, Mayer D, MacMillan DS, Nilsson T, Gaume R (2020) Third Realization of the International Celestial Reference Frame by Very Long Baseline Interferometry. å00(00):00

Chatterjee S, Cordes JM, Vlemmings WHT, Arzoumanian Z, Goss WM, Lazio TJW (2004) Pulsar Parallaxes at 5 GHz with the Very Long Baseline Array. Astrophys J 604(1):339–345, DOI 10.1086/381748, astro-ph/0312044

Clark B (2015) next generation VLA memo 10: Considerations for a Water Vapor Radiometer System. Tech. rep., NRAO, URL http://library.nrao.edu/public/memos/ngvla/NGVLA_10.pdf

Condon JJ, Cotton WD, Greisen EW, Yin QF, Perley RA, Taylor GB, Broderick JJ (1998) The NRAO VLA Sky Survey. AJ115(5):1693–1716, DOI 10.1086/300337

Counselman I C C (1976) Radio astrometry. ARA&A14:197–214, DOI 10.1146/annurev.aa.14.090176.001213

Deller AT, Brisken WF, Phillips CJ, Morgan J, Alef W, Cappallo R, Middelberg E, Romney J, Rottmann H, Tingay SJ, Wayth R (2011) DiFX-2: A More Flexible, Efficient, Robust, and Powerful Software Correlator. PASP 123:275–287, DOI 10.1086/658907, arXiv:1101.0885

Deller AT, Goss WM, Brisken WF, Chatterjee S, Cordes JM, Janssen GH, Kovalev YY, Lazio TJW, Petrov L, Stappers BW, Lyne A (2019) Microarcsecond VLBI Pulsar Astrometry with PSRπ II. Parallax Distances for 57 Pulsars. Astrophys J 875(2):100, DOI 10.3847/1538-4357/ab11c7, 1808.09046

Dodson R, Rioja M (2018) Investigations on MultiView VLBI for SKA. In: 14th European VLBI Network Symposium and Users Meeting, p 086, DOI 10.22323/1.344.0086

Dodson R, Rioja M, Asaki Y, Imai H, Hong XY, Shen Z (2013) The Application of MultiView Methods for High-precision Astrometric Space VLBI at Low Frequencies. AJ 145:147, DOI 10.1088/0004-6256/145/6/147, arXiv:1303.3402

Dodson R, Rioja MJ, Jung TH, Sohn BW, Byun DY, Cho SH, Lee SS, Kim J, Kim KT, Oh CS, Han ST, Je DH, Chung MH, Wi SO, Kang J, Lee JW, Chung H, Kim HR, Kim HG, Lee CH, Roh DG, Oh SJ, Yeom JH, Song MG, Kang YW (2014) Astrometrically Registered Simultaneous Observations of the 22 GHz H_2O and 43 GHz SiO Masers toward R Leonis Minoris Using KVN and Source/Frequency Phase Referencing. AJ 148:97, DOI 10.1088/0004-6256/148/5/97, arXiv:1408.3513

Dodson R, Rioja MJ, Jung T, Goméz JL, Bujarrabal V, Moscadelli L, Miller-Jones JCA, Tetarenko AJ, Sivakoff GR (2017a) The science case for simultaneous mm-wavelength receivers in radio astronomy. New A Rev.79:85–102, DOI 10.1016/j.newar.2017.09.003, 1709.07167

Dodson R, Rioja MJ, Molina SN, Gómez JL (2017b) High-precision Astrometric Millimeter Very Long Baseline Interferometry Using a New Method for Multi-frequency Calibra-

tion. ApJ834(2):177, DOI 10.3847/1538-4357/834/2/177, 1612.02958
Doeleman S, Agol E, Backer D, Baganoff F, Bower GC, Broderick A, Fabian A, Fish V, Gammie C, Ho P, Honman M, Krichbaum T, Loeb A, Marrone D, Reid M, Rogers A, Shapiro I, Strittmatter P, Tilanus R, Weintroub J, Whitney A, Wright M, Ziurys L (2009) Imaging an Event Horizon: submm-VLBI of a Super Massive Black Hole. In: astro2010: The Astronomy and Astrophysics Decadal Survey, vol 2010, 0906.3899
Doi A, Fujisawa K, Habe A, Honma M, Kawaguchi N, Kobayashi H, Murata Y, Omodaka T, Sudou H, Takaba H (2006) Bigradient Phase Referencing. PASJ58:777–785, DOI 10.1093/pasj/58.4.777, astro-ph/0604596
Doi A, Kono Y, Kimura K, Nakahara S, Oyama T, Okada N, Satou Y, Yamashita K, Matsumoto N, Baba M, Yasuda D, Suzuki S, Hasegawa Y, Honma M, Tanaka H, Ishimura K, Murata Y, Shimomukai R, Tachi T, Saito K, Watanabe N, Bando N, Kameya O, Yonekura Y, Sekido M, Inoue Y, Sakamoto H, Kogiso N, Shoji Y, Ogawa H, Fujisawa K, Narita M, Shibai H, Fuke H, Uehara K, Koyama S (2019) A balloon-borne very long baseline interferometry experiment in the stratosphere: Systems design and developments. Advances in Space Research 63(1):779–793, DOI 10.1016/j.asr.2018.09.020
Dunning A, Bowen M, Bourne M, Hayman D, Smith SL (2015) An ultra-wideband dielectrically loaded quad-ridged feed horn for radio astronomy. In: 2015 IEEE-APS Topical Conference on Antennas and Propagation in Wireless Communications (APWC), pp 787–790, DOI 10.1109/APWC.2015.7300180
Dunning A, Bowen MA, Hayman DB, Kanapathippillai J, Kanoniuk H, Shaw RD, Severs S (2016) The development of a wideband 'rocket' phased array feed. In: 2016 46th European Microwave Conference (EuMC), pp 1568–1571
Event Horizon Telescope Collaboration (2019) First M87 Event Horizon Telescope Results. I. The Shadow of the Supermassive Black Hole. ApJL875(1):L1, DOI 10.3847/2041-8213/ab0ec7, 1906.11238
Fisher JR, Bradley RF (2000) Full-sampling array feeds for radio telescopes. In: Butcher HR (ed) PROCSPIE, Society of Photo-Optical Instrumentation Engineers (SPIE) Conference Series, vol 4015, pp 308–318, DOI 10.1117/12.390425
Flygare J, Pantaleev M (2019) Dielectrically Loaded Quad-Ridge Flared Horn for Beamwidth Control over Decade Bandwidth -Optimization, Manufacture, and Measurement. IEEE 0(0):0, DOI 10.1109/TAP.2019.2940529
Fomalont E, Kogan L (2005) ATMCA: Phase Referencing using more than one calibrator: AIPS Memo 111. Tech. rep., NRAO
Fomalont E, Johnston K, Fey A, Boboltz D, Oyama T, Honma M (2011) The Position/Structure Stability of Four ICRF2 Sources. AJ141:91, DOI 10.1088/0004-6256/141/3/91, 1012.2804
Fomalont EB, Kopeikin S (2002) Phase Referencing Using Several Calibrator Sources. In: Ros E, Porcas RW, Lobanov AP, Zensus JA (eds) Proceedings of the 6th EVN Symposium, p 53
Fomalont EB, Goss WM, Beasley AJ, Chatterjee S (1999) Sub-Milliarcsecond Precision of Pulsar Motions: Using In-Beam Calibrators with the VLBA. AJ117:3025–3030, DOI 10.1086/300877, astro-ph/9903042
Forbrich J, Dzib S, Reid M, Menten K (2020) A VLBA Survey of radio stars in the Orion Nebula Cluster: I. The nonthermal radio population. ApJ
Frouard J, Johnson MC, Fey A, Makarov VV, Dorland BN (2018) Toward the ICRF3: Astrometric Comparison of the USNO 2016A VLBI Solution with ICRF2 and Gaia DR1. AJ155(6):229, DOI 10.3847/1538-3881/aabafa, 1804.10240
Gaia Collaboration, Brown AGA, Vallenari A, Prusti T, de Bruijne JHJ, Babusiaux C, Bailer-Jones CAL, Biermann M, Evans DW, Eyer L, et al (2018a) Gaia Data Release 2. Summary of the contents and survey properties. A&A616:A1, DOI 10.1051/0004-6361/201833051, 1804.09365
Gaia Collaboration, Katz D, Antoja T, Romero-Gómez M, Drimmel R, Reylé C, Seabroke GM, Soubiran C, Babusiaux C, Di Matteo P, et al (2018b) Gaia Data Release 2. Mapping the Milky Way disc kinematics. A&A616:A11, DOI 10.1051/0004-6361/201832865, 1804.09380
Gaia Collaboration, Mignard F, Klioner SA, Lindegren L, Hernández J, Bastian U, Bombrun A, Hobbs D, Lammers U, Michalik D, et al (2018c) Gaia Data Release 2. The celestial

reference frame (Gaia-CRF2). A&A616:A14, DOI 10.1051/0004-6361/201832916
Garcia Miro C (2019) WP10: VLBI with the SKA. Tech. rep., JIVE
Greisen EW (2003) AIPS, the VLA, and the VLBA. Information Handling in Astronomy - Historical Vistas 285:109, DOI 10.1007/0-306-48080-8_7
Griv E, Jiang IG, Hou LG, Ngeow CC (2017) The nearby spiral density-wave structure of the Galaxy: Line-of-sight and longitudinal velocities of 61 masers. Astron Nachr 338:729–739, DOI 10.1002/asna.201713150
Guirado JC, Marcaide JM, Elosegui P, Ratner MI, Shapiro II, Eckart A, Quirrenbach A, Schalinski CJ, Witzel A (1995) VLBI differential astrometry of the radio sources 1928+738 and 2007+777 at 5 GHz. A&A293:613–625
Guirado JC, Marcaide JM, Pérez-Torres MA, Ros E (2000) VLBI difference astrometry at 43 GHz. A&A353:L37–L40, astro-ph/0002072
Guirado JC, Ros E, Jones DL, Lestrade JF, Marcaide JM, Pérez-Torres MA, Preston RA (2001) Space-VLBI phase-reference mapping and astrometry. A&A371:766–770, DOI 10.1051/0004-6361:20010370, astro-ph/0104365
Hachisuka K, Choi YK, Reid MJ, Brunthaler A, Menten KM, Sanna A, Dame TM (2015) Parallaxes of Star-forming Regions in the Outer Spiral Arm of the Milky Way. ApJ800:2, DOI 10.1088/0004-637X/800/1/2, 1412.7916
Hada K, Doi A, Kino M, Nagai H, Hagiwara Y, Kawaguchi N (2011) An origin of the radio jet in M87 at the location of the central black hole. Nature477(7363):185–187, DOI 10.1038/nature10387
Han ST, Lee JW, Kang J, Je DH, Chung MH, Wi SO, Sasao T, Wylde R (2008) Millimeter-wave Receiver Optics for Korean VLBI Network. Int J Infrared Millimeter Waves 29:69–78, DOI 10.1007/s10762-007-9296-7
Han ST, Lee JW, Kang J, Oh CS, Byun DY, Je DH, Chung MH, Wi SO, Song M, Kang YW, Lee SS, Kim SY, Sasao T, Goldsmith PF, Wylde R (2013) Korean VLBI Network Receiver Optics for Simultaneous Multifrequency Observation: Evaluation. PASP125:539, DOI 10.1086/671125
Han ST, Lee JW, Lee B, Chung MH, Lee SM, Je DH, Wi SO, Goldsmith PF (2017) A Millimeter-Wave Quasi-Optical Circuit for Compact Triple-Band Receiving System. J Infrared Millimeter Terahertz Waves 38:1487–1501, DOI 10.1007/s10762-017-0438-2
Hernández-Pajares M, Juan JM, Sanz J, Orus R, Garcia-Rigo A, Feltens J, Komjathy A, Schaer SC, Krankowski A (2009) The igs vtec maps: a reliable source of ionospheric information since 1998. J Geodesy 83(3):263–275, DOI 10.1007/s00190-008-0266-1
Hobbs G, Manchester RN, Dunning A, Jameson A, Roberts P, George D, Green JA, Tuthill J, Toomey L, Kaczmarek JF, Mader S, Marquarding M, Ahmed A, Amy SW, Bailes M, Beresford R, Bhat NDR, Bock DCJ, Bourne M, Bowen M, Brothers M, Cameron AD, Carretti E, Carter N, Castillo S, Chekkala R, Cheng W, Chung Y, Craig DA, Dai S, Dawson J, Dempsey J, Doherty P, Dong B, Edwards P, Ergesh T, Gao X, Han J, Hayman D, Indermuehle B, Jeganathan K, Johnston S, Kanoniuk H, Kesteven M, Kramer M, Leach M, Mcintyre V, Moss V, Osłowski S, Phillips C, Pope N, Preisig B, Price D, Reeves K, Reilly L, Reynolds J, Robishaw T, Roush P, Ruckley T, Sadler E, Sarkissian J, Severs S, Shannon R, Smart K, Smith M, Smith S, Sobey C, Staveley-Smith L, Tzioumis A, van Straten W, Wang N, Wen L, Whiting M (2020) An ultra-wide bandwidth (704 to 4 032 MHz) receiver for the Parkes radio telescope. PASA 37:e012, DOI 10.1017/pasa.2020.2, 1911.00656
Hodgson JA, Rani B, Lee SS, Algaba JC, Kino M, Trippe S, Park JH, Zhao GY, Byun DY, Kang S, Kim JY, Kim JS, Kim SW, Miyazaki A, Wajima K, Oh J, Kim Dw, Gurwell M (2018) KVN observations reveal multiple γ-ray emission regions in 3C 84? MNRAS475(1):368–378, DOI 10.1093/mnras/stx3041, 1802.02763
Honma M, Tamura Y, Reid MJ (2008) Tropospheric Delay Calibrations for VERA. PASJ60:951–960, DOI 10.1093/pasj/60.5.951
Honma M, Nagayama T, Sakai N (2015) Determining dynamical parameters of the Milky Way Galaxy based on high-accuracy radio astrometry. PASJ 67(4), DOI 10.1093/pasj/psv045, 70
Hyland L (2020) SPIRALS: Southern Hemisphere Parallax Interferometric Radio Astrometry Legacy Survey. PhD thesis, University of Tasmnaia (Aus)

Jackson N, Tagore A, Deller A, Moldón J, Varenius E, Morabito L, Wucknitz O, Carozzi T, Conway J, Drabent A, Kapinska A, Orrù E, Brentjens M, Blaauw R, Kuper G, Sluman J, Schaap J, Vermaas N, Iacobelli M, Cerrigone L, Shulevski A, ter Veen S, Fallows R, Pizzo R, Sipior M, Anderson J, Avruch IM, Bell ME, van Bemmel I, Bentum MJ, Best P, Bonafede A, Breitling F, Broderick JW, Brouw WN, Brüggen M, Ciardi B, Corstanje A, de Gasperin F, de Geus E, Eislöffel J, Engels D, Falcke H, Garrett MA, Grießmeier JM, Gunst AW, van Haarlem MP, Heald G, Hoeft M, Hörandel J, Horneffer A, Intema H, Juette E, Kuniyoshi M, van Leeuwen J, Loose GM, Maat P, McFadden R, McKay-Bukowski D, McKean JP, Mulcahy DD, Munk H, Pandey-Pommier M, Polatidis AG, Reich W, Röttgering HJA, Rowlinson A, Scaife AMM, Schwarz DJ, Steinmetz M, Swinbank J, Thoudam S, Toribio MC, Vermeulen R, Vocks C, van Weeren RJ, Wise MW, Yatawatta S, Zarka P (2016) LBCS: The LOFAR Long-Baseline Calibrator Survey. A&A595:A86, DOI 10.1051/0004-6361/201629016, 1608.02133

Jimenez-Monferrer S, Rioja MJ, Dodson R, Smirnov O, Guirado JC (2010) Multi-beam capabilities for high precision astrometry at low frequencies using VLBI. In: 10th European VLBI Network Symposium and EVN Users Meeting: VLBI and the New Generation of Radio Arrays, Manchester, Proceedings of Science, vol 125, p 84

Keith MJ, Jameson A, van Straten W, Bailes M, Johnston S, Kramer M, Possenti A, Bates SD, Bhat NDR, Burgay M, Burke-Spolaor S, D'Amico N, Levin L, McMahon PL, Milia S, Stappers BW (2010) The High Time Resolution Universe Pulsar Survey – I. System configuration and initial discoveries. Monthly Notices of the Royal Astronomical Society 409(2):619–627, DOI 10.1111/j.1365-2966.2010.17325.x

Kim DJ, Cho SH, Yun Y, Choi YK, Yoon DH, Kim J, Dodson R, Rioja MJ, Yang H, Yoon SJ (2018) Simultaneous VLBI Astrometry of H_2O and SiO Masers toward the Semiregular Variable R Crateris. ApJL866:L19, DOI 10.3847/2041-8213/aae58b, 1810.07739

Kirsten F, Vlemmings W, Campbell RM, Kramer M, Chatterjee S (2015) Revisiting the birth locations of pulsars B1929+10, B2020+28, and B2021+51. A&A 577:A111, DOI 10.1051/0004-6361/201425562, 1503.09061

Kounkel M, Covey K, Suárez G, Román-Zúñiga C, Hernandez J, Stassun K, Jaehnig KO, Feigelson ED, Peña Ramírez K, Roman-Lopes A, Da Rio N, Stringfellow GS, Kim JS, Borissova J, Fernández-Trincado JG, Burgasser A, García-Hernández DA, Zamora O, Pan K, Nitschelm C (2018) The APOGEE-2 Survey of the Orion Star-forming Complex. II. Six-dimensional Structure. AJ156:84, DOI 10.3847/1538-3881/aad1f1, 1805.04649

Kovalev YY, Petrov L, Plavin AV (2017) VLBI-Gaia offsets favor parsec-scale jet direction in active galactic nuclei. A&A598:L1, DOI 10.1051/0004-6361/201630031, 1611.02632

Kramer M, Stairs IH, Manchester RN, McLaughlin MA, Lyne AG, Ferdman RD, Burgay M, Lorimer DR, Possenti A, D'Amico N, et al (2006) Tests of general relativity from timing the double pulsar. Science 314(5796):97–102, DOI 10.1126/science.1132305

Krishnan V, Ellingsen SP, Reid MJ, Brunthaler A, Sanna A, McCallum J, Reynolds C, Bignall HE, Phillips CJ, Dodson R, Rioja M, Caswell JL, Chen X, Dawson JR, Fujisawa K, Goedhart S, Green JA, Hachisuka K, Honma M, Menten K, Shen ZQ, Voronkov MA, Walsh AJ, Xu Y, Zhang B, Zheng XW (2015) First Parallax Measurements Towards a 6.7 GHz Methanol Maser with the Australian Long Baseline Array - Distance to G 339.884-1.259. ApJ805(2):129, DOI 10.1088/0004-637X/805/2/129, 1503.05917

Krishnan V, Ellingsen SP, Reid MJ, Bignall HE, McCallum J, Phillips CJ, Reynolds C, Stevens J (2017) Parallaxes of 6.7-GHz methanol masers towards the G 305.2 high-mass star formation region. MNRAS465(1):1095–1105, DOI 10.1093/mnras/stw2850, 1611.00930

Lara L, Marcaide JM, Alberdi A, Guirado JC (1996) VLBI differential astrometry at large angular separation: 3C 395 - 3C 382. A&A314:672–678

Lee SS, Lobanov AP, Krichbaum TP, Witzel A, Zensus A, Bremer M, Greve A, Grewing M (2008) A Global 86 GHz VLBI Survey of Compact Radio Sources. AJ 136:159–180, DOI 10.1088/0004-6256/136/1/159, arXiv:0803.4035

Lee SS, Petrov L, Byun DY, Kim J, Jung T, Song MG, Oh CS, Roh DG, Je DH, Wi SO, Sohn BW, Oh SJ, Kim KT, Yeom JH, Chung MH, Kang J, Han ST, Lee JW, Kim BG, Chung H, Kim HG, Ryoung Kim H, Kang YW, Cho SH (2014) Early Science with the Korean VLBI Network: Evaluation of System Performance. AJ 147:77, DOI 10.1088/0004-6256/147/4/77

Lee SS, Wajima K, Algaba JC, Zhao GY, Hodgson JA, Kim DW, Park J, Kim JY, Miyazaki A, Byun DY, Kang S, Kim JS, Kim SW, Kino M, Trippe S (2016) Interferometric Monitoring of Gamma-Ray Bright AGNs. I. The Results of Single-epoch Multifrequency Observations. ApJS227(1):8, DOI 10.3847/0067-0049/227/1/8, 1610.09121

Lestrade JF, Rogers AEE, Whitney AR, Niell AE, Phillips RB, Preston RA (1990) Phase-Reference VLBI Observations of Weak Radio Sources. Milliarcsecond Position of Algol. AJ99:1663, DOI 10.1086/115447

Li D, Pan Z (2016) The Five-hundred-meter Aperture Spherical Radio Telescope Project. Radio Science 51:1060–1064, DOI 10.1002/2015RS005877, 1612.09372

Lin CC, Shu FH (1964) On the Spiral Structure of Disk Galaxies. ApJ140:646, DOI 10.1086/147955

Lindegren L (2020) The Gaia reference frame for bright sources examined using VLBI observations of radio stars. A&A633:A1, DOI 10.1051/0004-6361/201936161, 1906.09827

Lindegren L, Hernández J, Bombrun A, Klioner S, Bastian U, Ramos-Lerate M, de Torres A, Steidelmüller H, Stephenson C, Hobbs D, Lammers U, Biermann M, Geyer R, Hilger T, Michalik D, Stampa U, McMillan PJ, Castañeda J, Clotet M, Comoretto G, Davidson M, Fabricius C, Gracia G, Hambly NC, Hutton A, Mora A, Portell J, van Leeuwen F, Abbas U, Abreu A, Altmann M, Andrei A, Anglada E, Balaguer-Núñez L, Barache C, Becciani U, Bertone S, Bianchi L, Bouquillon S, Bourda G, Brüsemeister T, Bucciarelli B, Busonero D, Buzzi R, Cancelliere R, Carlucci T, Charlot P, Cheek N, Crosta M, Crowley C, de Bruijne J, de Felice F, Drimmel R, Esquej P, Fienga A, Fraile E, Gai M, Garralda N, González-Vidal JJ, Guerra R, Hauser M, Hofmann W, Holl B, Jordan S, Lattanzi MG, Lenhardt H, Liao S, Licata E, Lister T, Löffler W, Marchant J, Martin-Fleitas JM, Messineo R, Mignard F, Morbidelli R, Poggio E, Riva A, Rowell N, Salguero E, Sarasso M, Sciacca E, Siddiqui H, Smart RL, Spagna A, Steele I, Taris F, Torra J, van Elteren A, van Reeven W, Vecchiato A (2018) Gaia Data Release 2. The astrometric solution. A&A616:A2, DOI 10.1051/0004-6361/201832727, 1804.09366

Makarov VV, Berghea CT, Frouard J, Fey A, Schmitt HR (2019) The Precious Set of Radio-optical Reference Frame Objects in the Light of Gaia DR2 Data. ApJ873(2):132, DOI 10.3847/1538-4357/aafa1c, 1811.10117

Marcaide JM, Shapiro II (1984) VLBI study of 1038+528A and B : discovery of wavelength dependence of peak brightness location. ApJ276:56–59, DOI 10.1086/161592

Martí-Vidal I, Marcaide JM, Guirado JC, Pérez-Torres MA, Ros E (2008) Absolute kinematics of radio source components in the complete S5 polar cap sample. III. First wide-field high-precision astrometry at 15.4 GHz. A&A478(1):267–275, DOI 10.1051/0004-6361:20078067, 0711.1959

Martí-Vidal I, Abellán FJ, Marcaide JM, Guirado JC, Pérez-Torres MA, Ros E (2016) Absolute kinematics of radio-source components in the complete S5 polar cap sample. IV. Proper motions of the radio cores over a decade and spectral properties. A&A596:A27, DOI 10.1051/0004-6361/201628149, 1607.05089

Melis C (2018) VLBI Astrometry. URL https://osf.io/byrcf

Melis C, Reid MJ, Mioduszewski AJ, Stauffer JR, Bower GC (2014) A VLBI resolution of the Pleiades distance controversy. Science 345(6200):1029–1032, DOI 10.1126/science.1256101, 1408.6544

Middelberg E, Roy AL, Walker RC, Falcke H (2005) VLBI observations of weak sources using fast frequency switching. A&A433:897–909, DOI 10.1051/0004-6361:20042078, astro-ph/0412564

Miller-Jones JCA, et al. (2020) Inefficient stellar winds from a massive black hole progenitor in Cygnus X-1. Science 0:00–00

Mitchell DA, Greenhill LJ, Wayth RB, Sault RJ, Lonsdale CJ, Cappallo RJ, Morales MF, Ord SM (2008) Real-Time Calibration of the Murchison Widefield Array. IEEE Journal of Selected Topics in Signal Processing 2:707–717, DOI 10.1109/JSTSP.2008.2005327

Moldón J, Deller AT, Wucknitz O, Jackson N, Drabent A, Carozzi T, Conway J, Kapińska AD, McKean JP, Morabito L, Varenius E, Zarka P, Anderson J, Asgekar A, Avruch IM, Bell ME, Bentum MJ, Bernardi G, Best P, Bîrzan L, Bregman J, Breitling F, Broderick JW, Brüggen M, Butcher HR, Carbone D, Ciardi B, de Gasperin F, de Geus E, Duscha S, Eislöffel J, Engels D, Falcke H, Fallows RA, Fender R, Ferrari C, Frieswijk W, Garrett MA, Grießmeier J, Gunst AW, Hamaker JP, Hassall TE, Heald G, Hoeft

M, Juette E, Karastergiou A, Kondratiev VI, Kramer M, Kuniyoshi M, Kuper G, Maat P, Mann G, Markoff S, McFadden R, McKay-Bukowski D, Morganti R, Munk H, Norden MJ, Offringa AR, Orru E, Paas H, Pandey-Pommier M, Pizzo R, Polatidis AG, Reich W, Röttgering H, Rowlinson A, Scaife AMM, Schwarz D, Sluman J, Smirnov O, Stappers BW, Steinmetz M, Tagger M, Tang Y, Tasse C, Thoudam S, Toribio MC, Vermeulen R, Vocks C, van Weeren RJ, White S, Wise MW, Yatawatta S, Zensus A (2015) The LOFAR long baseline snapshot calibrator survey. A&A574:A73, DOI 10.1051/0004-6361/201425042, 1411.2743

Mooley KP, Deller AT, Gottlieb O, Nakar E, Hallinan G, Bourke S, Frail DA, Horesh A, Corsi A, Hotokezaka K (2018) Superluminal motion of a relativistic jet in the neutron-star merger GW170817. Nature561(7723):355–359, DOI 10.1038/s41586-018-0486-3, 1806.09693

Moscadelli L, Sánchez-Monge Á, Goddi C, Li JJ, Sanna A, Cesaroni R, Pestalozzi M, Molinari S, Reid MJ (2016) Outflow structure within 1000 AU of high-mass YSOs. I. First results from a combined study of maser and radio continuum emission. A&A585:A71, DOI 10.1051/0004-6361/201526238

Moscadelli L, Sanna A, Goddi C, Krishnan V, Massi F, Bacciotti F (2019) Protostellar Outflows at the EarliesT Stages (POETS). III. H_2O masers tracing disk-winds and jets near luminous YSOs. A&A631:A74, DOI 10.1051/0004-6361/201936436, 1909.08374

Moscadelli L, Sanna A, Goddi C, Krishnan V, Massi F, Bacciotti F (2020) Protostellar Outflows at the EarliesT Stages (POETS). IV. Statistical properties of the 22 GHz H_2O masers. A&A635:A118, DOI 10.1051/0004-6361/202037472, 2002.06871

Murphy E (ed) (2018) Science with a Next Generation Very Large Array, Astronomical Society of the Pacific Conference Series, vol 517

Murphy EJ, Bolatto A, Chatterjee S, Casey CM, Chomiuk L, Dale D, de Pater I, Dickinson M, Francesco JD, Hallinan G, Isella A, Kohno K, Kulkarni SR, Lang C, Lazio TJW, Leroy AK, Loinard L, Maccarone TJ, Matthews BC, Osten RA, Reid MJ, Riechers D, Sakai N, Walter F, Wilner D (2018) The ngVLA Science Case and Associated Science Requirements. In: Murphy E (ed) Science with a Next Generation Very Large Array, Astronomical Society of the Pacific Conference Series, vol 517, p 3

Nagayama T, Omodaka T, Handa T, Honma M, Kobayashi H, Kawaguchi N, Ueno Y (2011) Astrometry of Galactic Star-Forming Region G48.61+0.02 with VERA. Publ Astron Soc Japan 63(4):719–725, DOI 10.1093/pasj/63.4.719

Nagayama T, Hirota T, Honma M, Kurayama T, Adachi Y, Tamura Y, Kanya Y (2020) VEDA: VERA data analysis software for VLBI phase-referencing astrometry. PASJ DOI 10.1093/pasj/psaa044

Nair DG, Lobanov AP, Krichbaum TP, Ros E, Zensus JA, Kovalev YY, Lee SS, Mertens F, Hagiwara Y, Bremer M, Lindqvist M, de Vicente P (2019) Global millimeter VLBI array survey of ultracompact extragalactic radio sources at 86 GHz. A&A622:A92, DOI 10.1051/0004-6361/201833122, 1808.09243

Nakagawa A, Kurayama T, Matsui M, Omodaka T, Honma M, Shibata KM, Sato K, Jike T (2016) Parallax of a Mira variable R Ursae Majoris studied with astrometric VLBI. PASJ 68(5), DOI 10.1093/pasj/psw069, 78

Nakagawa A, Kurayama T, Orosz G, Burns RA, Oyama T, Nagayama T, Miyata T, Sekido M, Baba J, Wada K (2018) Astrometric VLBI Observations of the Galactic LPVs, Miras, and OH/IR stars. In: Tarchi A, Reid MJ, Castangia P (eds) Astrophysical Masers: Unlocking the Mysteries of the Universe, IAU Symposium, vol 336, pp 365–368, DOI 10.1017/S1743921317009449

Niell A, Barrett J, Burns A, Cappallo R, Corey B, Derome M, Eckert C, Elosegui P, McWhirter R, Poirier M, Rajagopalan G, Rogers A, Ruszczyk C, SooHoo J, Titus M, Whitney A, Behrend D, Bolotin S, Gipson J, Gordon D, Himwich E, Petrachenko B (2018) Demonstration of a broadband very long baseline interferometer system: A new instrument for high-precision space geodesy. Radio Science 53(10):1269–1291, DOI 10.1029/2018RS006617

Niinuma K, Kino M, Doi A, Hada K, Nagai H, Koyama S (2015) Discovery of a Wandering Radio Jet Base after a Large X-Ray Flare in the Blazar Markarian 421. ApJL807(1):L14, DOI 10.1088/2041-8205/807/1/L14, 1507.04082

Orosz G, Imai H, Dodson R, Rioja MJ, Frey S, Burns RA, Etoka S, Nakagawa A, Nakanishi H, Asaki Y, Goldman SR, Tafoya D (2017) Astrometry of OH/IR Stars Using 1612 MHz Hydroxyl Masers. I. Annual Parallaxes of WX Psc and OH138.0+7.2. AJ153(3):119, DOI 10.3847/1538-3881/153/3/119, 1701.05101

Ortiz-León GN, Loinard L, Dzib SA, Kounkel M, Galli PAB, Tobin JJ, Evans I Neal J, Hartmann L, Rodríguez LF, Briceño C, Torres RM, Mioduszewski AJ (2018) Gaia-DR2 Confirms VLBA Parallaxes in Ophiuchus, Serpens, and Aquila. ApJL869(2):L33, DOI 10.3847/2041-8213/aaf6ad, 1812.02360

Paragi Z, Godfrey L, Reynolds C, Rioja MJ, Deller A, Zhang B, Gurvits L, Bietenholz M, Szomoru A, Bignall HE, Boven P, Charlot P, Dodson R, Frey S, Garrett MA, Imai H, Lobanov A, Reid MJ, Ros E, van Langevelde HJ, Zensus AJ, Zheng XW, Alberdi A, Agudo I, An T, Argo M, Beswick R, Biggs A, Brunthaler A, Campbell B, Cimo G, Colomer F, Corbel S, Conway JE, Cseh D, Deane R, Falcke HDE, Gawronski M, Gaylard M, Giovannini G, Giroletti M, Goddi C, Goedhart S, Gómez JL, Gunn A, Kharb P, Kloeckner HR, Koerding E, Kovalev Y, Kunert-Bajraszewska M, Lindqvist M, Lister M, Mantovani F, Marti-Vidal I, Mezcua M, McKean J, Middelberg E, Miller-Jones JCA, Moldon J, Muxlow T, O'Brien T, Perez-Torres M, Pogrebenko SV, Quick J, Rushton A, Schilizzi R, Smirnov O, Sohn BW, Surcis G, Taylor GB, Tingay S, Tudose VM, van der Horst A, van Leeuwen J, Venturi T, Vermeulen R, Vlemmings WHT, de Witt A, Wucknitz O, Yang J, Gabänyi K, Jung T (2015) Very Long Baseline Interferometry with the SKA. In: Advancing Astrophysics with the Square Kilometre Array (AASKA14), p 143, 1412.5971

Paragi Z, Chrysostomou A, Garcia-Miro C (2018) SKA-VLBI Key Science Programmes. In: 14th European VLBI Network Symposium & Users Meeting (EVN 2018), p 85

Perutz MF (1962) X-ray Analysis of Haemoglobin: Nobel Lecture. URL https://www.nobelprize.org/prizes/chemistry/1962/perutz/lecture

Petrov L (2016) VLBA Calibrator Survey 9 (VCS-9). ArXiv e-prints 1610.04951

Petrov L, Kovalev YY, Fomalont EB, Gordon D (2008) The Sixth VLBA Calibrator Survey: VCS6. AJ136:580–585, DOI 10.1088/0004-6256/136/2/580, 0801.3895

Petrov L, de Witt A, Sadler EM, Phillips C, Horiuchi S (2019a) The Second LBA Calibrator Survey of southern compact extragalactic radio sources - LCS2. MNRAS485(1):88–101, DOI 10.1093/mnras/stz242, 1812.02916

Petrov L, Kovalev YY, Plavin AV (2019b) A quantitative analysis of systematic differences in the positions and proper motions of Gaia DR2 with respect to VLBI. MNRAS482(3):3023–3031, DOI 10.1093/mnras/sty2807, 1808.05114

Plavin AV, Kovalev YY, Petrov LY (2019) Dissecting the AGN Disk-Jet System with Joint VLBI-Gaia Analysis. ApJ871(2):143, DOI 10.3847/1538-4357/aaf650, 1808.05115

Porcas RW (2009) Radio astrometry with chromatic AGN core positions. A&A505:L1–L4, DOI 10.1051/0004-6361/200912846, 0909.0933

Porcas RW, Rioja MJ (2000) Earth-Space VLBI of the Quasar Pair 1038+52A,B. Advances in Space Research 26(4):673–676, DOI 10.1016/S0273-1177(99)01188-6

Porcas RW, Rioja MJ (2002) VLBI phase-reference investigations at 86 GHz. In: Ros E, Porcas RW, Lobanov AP, Zensus JA (eds) Proceedings of the 6th EVN Symposium, p 65

Pradel N, Charlot P, Lestrade JF (2006) Astrometric accuracy of phase-referenced observations with the VLBA and EVN. A&A452:1099–1106, DOI 10.1051/0004-6361:20053021, astro-ph/0603015

Radcliffe JF, Garrett MA, Beswick RJ, Muxlow TWB, Barthel PD, Deller AT, Middelberg E (2016) Multi-source self-calibration: Unveiling the microJy population of compact radio sources. A&A587:A85, DOI 10.1051/0004-6361/201527980, 1601.04452

Reid M, Loinard L, Maccarone T (2018) Astrometry and Long Baseline Science. In: Murphy E (ed) Science with a Next Generation Very Large Array, Astronomical Society of the Pacific Conference Series, vol 517, p 523, 1810.06577

Reid MJ, Honma M (2014) Microarcsecond Radio Astrometry. ARAA 52:339–372, DOI 10.1146/annurev-astro-081913-040006, arXiv:1312.2871

Reid MJ, Readhead ACS, Vermeulen RC, Treuhaft RN (1999) The Proper Motion of Sagittarius A*. I. First VLBA Results. ApJ524(2):816–823, DOI 10.1086/307855, astro-ph/9905075

Reid MJ, Menten KM, Brunthaler A, Zheng XW, Moscadelli L, Xu Y (2009) Trigonometric Parallaxes of Massive Star-Forming Regions. I. S 252 & G232.6+1.0. ApJ693(1):397–405, DOI 10.1088/0004-637X/693/1/397, 0811.0595

Reid MJ, Menten KM, Brunthaler A, Zheng XW, Dame TM, Xu Y, Wu Y, Zhang B, Sanna A, Sato M, Hachisuka K, Choi YK, Immer K, Moscadelli L, Rygl KLJ, Bartkiewicz A (2014) Trigonometric Parallaxes of High Mass Star Forming Regions: The Structure and Kinematics of the Milky Way. ApJ783:130, DOI 10.1088/0004-637X/783/2/130, 1401.5377

Reid MJ, Brunthaler A, Menten KM, Sanna A, Xu Y, Li JJ, Wu Y, Hu B, Zheng XW, Zhang B, Immer K, Rygl K, Moscadelli L, Sakai N, Bartkiewicz A, Choi YK (2017) Techniques for Accurate Parallax Measurements for 6.7 GHz Methanol Masers. AJ154:63, DOI 10.3847/1538-3881/aa7850, 1706.03128

Reid MJ, Menten KM, Brunthaler A, Zheng XW, Dame TM, Xu Y, Li J, Sakai N, Wu Y, Immer K, Zhang B, Sanna A, Moscadelli L, Rygl KLJ, Bartkiewicz A, Hu B, Quiroga-Nuñez LH, van Langevelde HJ (2019) Trigonometric Parallaxes of High-mass Star-forming Regions: Our View of the Milky Way. ApJ885(2):131, DOI 10.3847/1538-4357/ab4a11

Rioja M, Dodson R (2011) High-precision Astrometric Millimeter Very Long Baseline Interferometry Using a New Method for Atmospheric Calibration. AJ 141:114, DOI 10.1088/0004-6256/141/4/114, arXiv:1101.2051

Rioja M, Dodson R, Malarecki J, Asaki Y (2011a) Exploration of Source Frequency Phase Referencing Techniques for Astrometry and Observations of Weak Sources with High Frequency Space Very Long Baseline Interferometry. AJ 142:157, DOI 10.1088/0004-6256/142/5/157, arXiv:1110.0267

Rioja M, Dodson R, Reynolds J (2011b) Demonstration of MultiBeam to PAF VLBI correlation for ASKAP. Tech. rep., University of Western Australia, Australia

Rioja MJ (1993) Astrometría diferencial de precisión comparada del par de radio-fuentes 1038+528 A y B". PhD thesis, University of Granada (Spain)

Rioja MJ, Porcas RW (2000) A phase-reference study of the quasar pair 1038+528A,B. A&A355:552–563, astro-ph/0002097

Rioja MJ, Marcaide JM, Elosegui P, Shapiro II (1997a) Results from a decade-long VLBI astrometric monitoring of the pair of quasars 1038+528 A and B. A&A325:383–390

Rioja MJ, Stevens E, Gurvits L, Alef W, Schilizzi RT, Sasao T, Asaki Y (1997b) Phase-referencing in "cluster-cluster" VLBI mode. Vistas in Astronomy 41:213–217, DOI 10.1016/S0083-6656(97)00008-1

Rioja MJ, Porcas RW, Desmurs JF, Alef W, Gurvits LI, Schilizzi RT (2002) VLBI observations in Cluster-Cluster mode at 1.6 GHz. In: Ros E, Porcas RW, Lobanov AP, Zensus JA (eds) Proceedings of the 6th EVN Symposium, p 57, astro-ph/0207210

Rioja MJ, Dodson R, Kamohara R, Colomer F, Bujarrabal V, Kobayashi H (2008) Relative Astrometry of the J = 1→0, v = 1 and v = 2 SiO Masers toward R Leonis Minoris Using VERA. PASJ 60:1031–1038, DOI 10.1093/pasj/60.5.1031, arXiv:0811.3820

Rioja MJ, Dodson R, Jung T, Sohn BW, Byun DY, Agudo I, Cho SH, Lee SS, Kim J, Kim KT, Oh CS, Han ST, Je DH, Chung MH, Wi SO, Kang J, Lee JW, Chung H, Ryoung Kim H, Kim HG, Lee CH, Roh DG, Oh SJ, Yeom JH, Song MG, Kang YW (2014) Verification of the Astrometric Performance of the Korean VLBI Network, Using Comparative SFPR Studies with the VLBA at 14/7 mm. AJ 148:84, DOI 10.1088/0004-6256/148/5/84, arXiv:1407.4604

Rioja MJ, Dodson R, Jung T, Sohn BW (2015) The Power of Simultaneous Multi-Frequency Observations for mm-VLBI: Astrometry up to 130 GHz with the KVN. AJ 150:202

Rioja MJ, Dodson R, Orosz G, Imai H, Frey S (2017) MultiView High Precision VLBI Astrometry at Low Frequencies. AJ153:105, DOI 10.3847/1538-3881/153/3/105, 1612.02554

Rioja MJ, Dodson R, Franzen TMO (2018) LEAP: an innovative direction-dependent ionospheric calibration scheme for low-frequency arrays. MNRAS478:2337–2349, DOI 10.1093/mnras/sty1195, 1807.04685

Robertson DS (1975) Geodetic and Astrometric Measurements with Very Long Baseline Interferometry. PhD thesis, MIT

Ros E, Marcaide JM, Guirado JC, Ratner MI, Shapiro II, Krichbaum TP, Witzel A, Preston RA (1999) High precision difference astrometry applied to the triplet of S5 radio sources

B1803+784/Q1928+738/B2007+777. A&A348:381–393, astro-ph/9905265
Roy A, Rottmann H, Teuber U, Keller R (2006) Phase correction of VLBI with water vapour radiometry. In: Proceedings of the 8th European VLBI Network Symposium, p 58
Rygl K, Wu Y, Reid MJ, Brunthaler A, Menten K (2018) Astrometry of star-forming regions in the Sagittarius spiral arms. In: 14th European VLBI Network Symposium and Users Meeting, p 036, DOI 10.22323/1.344.0036
Sakai N (2018) Eight new astrometry results of 6.7 GHz CH_3OH and 22 GHz H_2O masers in the Perseus arm. In: Tarchi A, Reid MJ, Castangia P (eds) Astrophysical Masers: Unlocking the Mysteries of the Universe, IAU Symposium, vol 336, pp 168–171, DOI 10.1017/S1743921317010110
Sakai N, Nakanishi H, Matsuo M, Koide N, Tezuka D, Kurayama T, Shibata KM, Ueno Y, Honma M (2015) Outer rotation curve of the Galaxy with VERA. III. Astrometry of IRAS 07427-2400 and test of the density-wave theory. PASJ67(4):69, DOI 10.1093/pasj/psv049, 1505.03543
Sakai N, Nagayama T, Nakanishi H, Koide N, Kurayama T, Izumi N, Hirota T, Yoshida T, Shibata KM, Honma M (2019a) Vertical structure and kinematics of the Galactic outer disk. PASJ DOI 10.1093/pasj/psz125, 1910.08146
Sakai N, Reid MJ, Menten KM, Brunthaler A, Dame TM (2019b) Noncircular Motions in the Outer Perseus Spiral Arm. ApJ876(1):30, DOI 10.3847/1538-4357/ab12e0, 1903.11103
Sanna A, Reid MJ, Dame TM, Menten KM, Brunthaler A (2017) Mapping spiral structure on the far side of the Milky Way. Science 358:227–230, DOI 10.1126/science.aan5452, 1710.06489
Sanna A, Moscadelli L, Goddi C, Krishnan V, Massi F (2018) Protostellar Outflows at the EarliesT Stages (POETS). I. Radio thermal jets at high resolution nearby H_2O maser sources. A&A619:A107, DOI 10.1051/0004-6361/201833573, 1807.06680
Selina RJ, Murphy EJ, McKinnon M, Beasley A, Butler B, Carilli C, Clark B, Durand S, Erickson A, Grammer W, Hiriart R, Jackson J, Kent B, Mason B, Morgan M, Ojeda OY, Rosero V, Shillue W, Sturgis S, Urbain D (2018) The ngVLA Reference Design. In: Murphy E (ed) Science with a Next Generation Very Large Array, Astronomical Society of the Pacific Conference Series, vol 517, p 15
Shapiro II, Wittels JJ, Counselman CC III, Robertson DS, Whitney AR, Hinteregger HF, Knight CA, Rogers AEE, Clark TA, Hutton LK, Niell AE (1979) Submilliarcsecond astrometry via VLBI. I - Relative position of the radio sources 3C 345 and NRAO 512. AJ84:1459–1469, DOI 10.1086/112565
Smirnov A, Pilipenko S, Golubev E, Arhipov M, Pishnov V, Kosmovich T, Filina E, Baryshev A, De Graauw T, Likhachev S, Kardashev N (2018) Current status of the Millimetron Space Observatory. In: 42nd COSPAR Scientific Assembly, vol 42, pp E4.2–12–18
Sohn BW, Giovannini G, Giroletti M, Kino M, Hada K, Ro H, Kim J, Koyama S, Orienti M, Honma M, Nagai H, Oyama T, Lico R, Oh S, Zhao G, Cassaro P, Orfei A, Stagni T M Jung, Vincente P, M R, Dodson R (2018) EATING VLBI and KVN-Yebes observations of AGN jets. In: 14th European VLBI Network Symposium and Users Meeting, p 120, DOI 10.22323/1.344.0120
Sovers OJ, Fanselow JL, Jacobs CS (1998) Astrometry and geodesy with radio interferometry: experiments, models, results. Reviews of Modern Physics 70(4):1393–1454, DOI 10.1103/RevModPhys.70.1393, astro-ph/9712238
Sudou H, Omodaka T, Murakami K, Nagayama T, Nakagawa A, Urago R, Nagayama T, Hirano K, Honma M (2019) Annual parallax measurements of a semi-regular variable star SV Pegasus with VERA. PASJ71(1):16, DOI 10.1093/pasj/psy133, 1810.13064
Tercero F, García-Pérez O (2019) Broadband k-q-w feed system for the 40 meters yebes radio telescope. In: 2019 International Conference on Electromagnetics in Advanced Applications (ICEAA), pp 0719–0724, DOI 10.1109/ICEAA.2019.8879329
Thompson AR, Moran JM, Swenson J George W (2017) Interferometry and Synthesis in Radio Astronomy, 3rd edn. Springer, Cham, DOI 10.1007/978-3-319-44431-4
Titov O (2007) Effect of the selection of reference radio sources on geodetic estimates from vlbi observations. J Geodesy 81(6):455–468, DOI 10.1007/s00190-007-0145-1
Truebenbach AE, Darling J (2017) The VLBA Extragalactic Proper Motion Catalog and a Measurement of the Secular Aberration Drift. ApJS233(1):3, DOI 10.3847/1538-4365/

aa9026
Tsuboi M (2009) VSOP-2/ASTRO-G Project Overview for the Astronomy Community. In: Hagiwara Y, Fomalont E, Tsuboi M, Yasuhiro M (eds) Approaching Micro-Arcsecond Resolution with VSOP-2: Astrophysics and Technologies, Astronomical Society of the Pacific Conference Series, vol 402, p 30
Vallenari A (2018) The future of astrometry in space. Frontiers Astron Space Sci 5:11, DOI 10.3389/fspas.2018.00011
van Bemmel I, Small D, Kettenis M, Szomoru A, Moellenbrock G, Janssen M (2018) CASA on the fringe. In: 14th European VLBI Network Symposium and Users Meeting, p 79, DOI 10.22323/1.344.0079
van Langevelde H, Quiroga-Nuñez LH, Vlemmings WHT, Loinard L, Honma M, Nakagawa K A Immer, Burns Y R Pihlstrom, Sjouwerman L, Natarajan I, Rich RM, Deane R (2018) The Synergy between VLBI and Gaia astrometry. In: 14th European VLBI Network Symposium and Users Meeting, p 043, DOI 10.22323/1.344.0043
van Langevelde HJ, Vlemmings W, Diamond PJ, Baudry A, Beasley AJ (2000) VLBI astrometry of the stellar image of U Herculis, amplified by the 1667 MHz OH maser. A&A357:945–950, astro-ph/0003300
Venturi T, Paragi Z, Lindqvist M (2020) VLBI20-30: a scientific roadmap for the next decade. The future of the European VLBI Network. Tech. rep., JIVE
VERA Collaboration, Hirota T, Nagayama T, Honma M, Adachi Y, Burns RA, Chibueze JO, Choi YK, Hachisuka K, Hada K, Hagiwara Y, Hamada S, Hand a T, Hashimoto M, Hirano K, Hirata Y, Ichikawa T, Imai H, Inenaga D, Ishikawa T, Jike T, Kameya O, Kaseda D, Kim JS, Kim J, Kim MK, Kobayashi H, Kono Y, Kurayama T, Matsuno M, Morita A, Motogi K, Murase T, Nakagawa A, Nakanishi H, Niinuma K, Nishi J, Oh CS, Omodaka T, Oyadomari M, Oyama T, Sakai D, Sakai N, Sawada-Satoh S, Shibata KM, Shizugami M, Sudo J, Sugiyama K, Sunada K, Suzuki S, Takahashi K, Tamura Y, Tazaki F, Ueno Y, Uno Y, Urago R, Wada K, Wu YW, Yamashita K, Yamashita Y, Yamauchi A, Yuda A (2020) The First VERA Astrometry Catalog. PASJ DOI 10.1093/pasj/psaa018, 2002.03089
Walker RC, Chatterjee S (1999) VLBA Scientific Memorandum n. 23: Ionospheric Corrections Using GPS Based Models. Tech. rep., NRAO, URL https://science.nrao.edu/facilities/vlba/publications/memos/sci/sci23memo.ps
Wittels JJ (1975) Positions and Kinematics of Quasars and Related Radio Objects Inferred from VLBI Observations. PhD thesis, Massachusetts Institute of Technology (USA)
Wood PR (2015) The pulsation modes, masses and evolution of luminous red giants. MNRAS448(4):3829–3843, DOI 10.1093/mnras/stv289, 1502.03137
Wu YW, Reid MJ, Sakai N, Dame TM, Menten KM, Brunthaler A, Xu Y, Li JJ, Ho B, Zhang B, Rygl KLJ, Zheng XW (2019) Trigonometric Parallaxes of Star-forming Regions beyond the Tangent Point of the Sagittarius Spiral Arm. ApJ874(1):94, DOI 10.3847/1538-4357/ab001a, 1901.09313
Xu S, Zhang B, Reid MJ, Menten KM, Zheng X, Wang G (2018) The Parallax of the Red Hypergiant VX Sgr with Accurate Tropospheric Delay Calibration. ApJ859(1):14, DOI 10.3847/1538-4357/aabba6, 1804.00894
Xu S, Zhang B, Reid MJ, Zheng X, Wang G (2019) Comparison of Gaia DR2 Parallaxes of Stars with VLBI Astrometry. ApJ875(2):114, DOI 10.3847/1538-4357/ab0e83, 1903.04105
Xu Y, Reid M, Dame T, Menten K, Sakai N, Li J, Brunthaler A, Moscadelli L, Zhang B, Zheng X (2016) The local spiral structure of the Milky Way. Science Advances 2:e1600878–e1600878, DOI 10.1126/sciadv.1600878, 1610.00242
Yang H, Cho SH, Yun Y, Yoon DH, Kim DJ, Kim H, Yoon SC, Dodson R, Rioja MJ, Imai H (2019) Asymmetric distributions of H2O and SiO masers toward the symbiotic star V627 Cas. submitted
Yang J, Pantaleev M, Kildal P, Klein B, Karandikar Y, Helldner L, Wadefalk N, Beaudoin C (2011) Cryogenic 2–13 ghz eleven feed for reflector antennas in future wideband radio telescopes. IEEE Transactions on Antennas and Propagation 59(6):1918–1934, DOI 10.1109/TAP.2011.2122229
Yang J, Paragi Z, van der Horst AJ, Gurvits LI, Campbell RM, Giannios D, An T, Komossa S (2016) No apparent superluminal motion in the first-known jetted tidal disruption event

Swift J1644+5734. MNRAS462(1):L66–L70, DOI 10.1093/mnrasl/slw107, 1605.06461
Yao JM, Manchester RN, Wang N (2017) A New Electron-density Model for Estimation of Pulsar and FRB Distances. ApJ835(1):29, DOI 10.3847/1538-4357/835/1/29, 1610.09448
Yoon DH, Cho SH, Yun Y, Choi YK, Dodson R, Rioja M, Kim J, Imai H, Kim D, Yang H, Byun DY (2018) Astrometrically registered maps of H_2O and SiO masers toward VX Sagittarii. Nat Commun 9:2534, DOI 10.1038/s41467-018-04767-8, 1807.04455
Zhang B, Reid MJ, Menten KM, Zheng XW, Brunthaler A, Dame TM, Xu Y (2013) Parallaxes for W49N and G048.60+0.02: Distant Star Forming Regions in the Perseus Spiral Arm. ApJ775(1):79, DOI 10.1088/0004-637X/775/1/79, 1312.3856
Zhang B, Zheng X, Reid MJ, Honma M, Menten KM, Brunthaler A, Kim J (2017) VLBA Trigonometric Parallax Measurement of the Semi-regular Variable RT Vir. ApJ849(2):99, DOI 10.3847/1538-4357/aa8ee9
Zhang B, Reid MJ, Zhang L, Wu Y, Hu B, Sakai N, Menten KM, Zheng X, Brunthaler A, Dame TM, Xu Y (2019) Parallaxes for Star-forming Regions in the Inner Perseus Spiral Arm. AJ157(5):200, DOI 10.3847/1538-3881/ab141d, 1903.11594
Zhao GY, Algaba JC, Lee SS, Jung T, Dodson R, Rioja M, Byun DY, Hodgson J, Kang S, Kim DW, Kim JY, Kim JS, Kim SW, Kino M, Miyazaki A, Park JH, Trippe S, Wajima K (2018) The Power of Simultaneous Multi-frequency Observations for mm-VLBI: Beyond Frequency Phase Transfer. AJ155(1):26, DOI 10.3847/1538-3881/aa99e0, 1712.06243
Zhao GY, Jung T, Sohn BW, Kino M, Honma M, Dodson R, Rioja M, Han ST, Shibata K, Byun DY, Akiyama K, Algaba JC, An T, Cheng X, Cho I, Cui Y, Hada K, Hodgson JA, Jiang W, Lee JW, Lee JA, Niinuma K, Park JH, Ro H, Sawada-Satoh S, Shen ZQ, Tazaki F, Trippe S, Wajima K, Zhang Y (2019) Source-Frequency Phase-Referencing Observation of AGNS with KAVA Using Simultaneous Dual-Frequency Receiving. J Korean Astron Soc 52(1):23–30, DOI 10.5303/JKAS.2019.52.1.23, 1903.11796

A Symbols

Table 4 Symbols and abbreviations used in this review.

Quantities	
ν	Observing frequency.
$\phi_{A,B,C}$	Residual phase observable for sources A, B or C.
$\phi_{T,R}$	Residual phase observable for target or reference.
τ_ϕ	Residual phase Delay, $\frac{1}{2\pi}\frac{\phi}{\nu}$.
τ_g	Residual Group Delay, $\frac{1}{2\pi}\frac{\delta\phi}{\delta\nu}$.
t	time.
$\overrightarrow{b}$	VLBI baseline vector.
$\hat{s}$	unit vector in the direction of the source.
$\theta_{\rm beam}$	Synthesised beamwidth of the array.
$\delta\theta$	The final astrometric product.
Acronyms	
AIC	Advanced Ionospheric Calibration.
ATC	Advanced Tropospheric Calibration.
DR	Dynamic Range.
EOP	The Earth Orientation Parameter.
ICRF	International Celestial Reference Frame.
MFPR	Multi-Frequency Phase Referencing.
MV	MultiView.
RMS	Root Mean Square.
SEFD	System Equivalent Flux Density.
SFPR	Source/Frequency Phase Referencing.
SNR	Signal to Noise Ratio.
TAB	Tied Array Beam.
TEC	Total Electron Content measured in TEC units. 1 TECU = 10^{16} electrons.m^{-2}
Residual Error Contributors	
$\phi_{\rm pos,str,geo,ion,tro}$	Residual phase terms from source position and structure, array geometry, ionosphere and troposphere propagation respectively.
$\Delta\theta_{\rm ion,tro,AB}$	Angular separation relevant for ionospheric calibration, tropospheric calibration or between sources, respectively.
C_w	Unitless parameter for the tropospheric dynamic scale: 1,2 or 4 for good, normal or poor.
$Z_{g,i,F}$	mean Zenith angle between sources from the ground, at ionospheric pierce points for the the bottom and the peak of the F-layer, respectively.
$n_{T,R}$	number of phase ambiguities for target or reference observations, respectively.
$\Delta\nu_{\rm eff}$	Effective synthesised frequency bandwidth relevant in geodetic observations.
$\sum_{i=1}^{N}\alpha_i$	Weighted sum of calibrator corrections relevant for MV.
$\mathcal{R}$	General scale factor, for example: the frequency ratio in SFPR or $\sum_{i=1}^{N}\alpha_i$ in MV.
$\Delta\ell_z$	Residual tropospheric excess path length at Zenith.
ΔI	Residual ionospheric TEC.
$\Delta\ell_I$	ΔI expressed as excess path length at 1GHz.
Measurement precision	
$\sigma\phi^{\rm cal}$	Combination of all systematic phase errors relevant for a given calibration method (e.g. PR, MV or SFPR).
$\sigma\Phi$	Standard Deviation of the phase observable.
$\sigma\phi_{\rm thermal}$	Thermal phase noise contribution.
$\sigma\Delta\theta_{\rm thermal}$	Thermal astrometric error contribution.
$\sigma\Delta\theta^{cal}$	Systematic astrometric error contribution for a given calibration method (e.g. PR, MV or SFPR).
$\sigma\Delta\theta$	Total RMS of the astrometric measurement (systematic plus thermal).